

# Dynamic Cantilever Magnetometry of Individual Ferromagnetic Nanotubes

## Inauguraldissertation

zur Erlangung der Würde eines Doktors der Philosophie

vorgelegt der  
Philosophisch-Naturwissenschaftlichen Fakultät  
der Universität Basel

von

**Dennis Patrick Weber**

aus Rastatt, Deutschland

Basel, 2014



Diese Inauguraldissertation (Originaldokument auf dem Dokumentenserver der Universität Basel [edoc.unibas.ch](http://edoc.unibas.ch)) von Dennis Patrick Weber steht unter der Creative-Commons-Lizenz Namensnennung – Nicht-kommerziell – Keine Bearbeitung 3.0 Schweiz. Um eine Kopie dieser Lizenz einzusehen, besuchen Sie <http://creativecommons.org/licenses/by-nc-nd/3.0/ch/>.

Genehmigt von der Philosophisch-Naturwissenschaftlichen Fakultät auf Antrag von

Prof. Dr. Martino Poggio  
Fakultätsverantwortlicher

Prof. Dr. Ernst Meyer  
Korreferent

Basel, den 16.09.2014

Prof. Dr. Jörg Schibler  
Dekan



## Namensnennung - Nicht-kommerziell - Keine Bearbeitung 3.0 Schweiz (CC BY-NC-ND 3.0 CH)

Dies ist eine alltagssprachliche Zusammenfassung der Lizenz (die diese nicht ersetzt), und sie ist in folgenden Landessprachen verfügbar: **Deutsch**  
**Französisch**

Haftungsbeschränkung

### Sie dürfen:



**Teilen** — das Material in jedwedem Format oder Medium vervielfältigen und weiterverbreiten

Der Lizenzgeber kann diese Freiheiten nicht widerrufen solange Sie sich an die Lizenzbedingungen halten.

### Unter folgenden Bedingungen:



**Namensnennung** — Sie müssen **die Urheberschaft ausreichend deutlich benennen**, einen Link zur Lizenz beifügen und angeben, ob **Änderungen vorgenommen** wurden. Diese Angaben dürfen in jeder angemessenen Art und Weise gemacht werden, allerdings nicht so, dass der Eindruck entsteht, der Lizenzgeber unterstütze gerade Sie oder Ihre Nutzung des Werks besonders.



**Nicht kommerziell** — Sie dürfen das Material nicht für **kommerzielle Zwecke** nutzen.



**Keine Bearbeitungen** — Wenn Sie das Material **remixen, verändern oder darauf anderweitig direkt aufbauen** dürfen Sie die bearbeitete Fassung der Materials nicht verbreiten.

**Keine weiteren Einschränkungen** — Sie dürfen keine zusätzlichen Klauseln oder **technische Verfahren** einsetzen, die anderen rechtlich irgendetwas untersagen, was die Lizenz erlaubt.

### Hinweise:

Sie müssen sich nicht an diese Lizenz halten hinsichtlich solcher Teile des Materials, die gemeinfrei sind, oder soweit Ihre Nutzungshandlungen durch **Ausnahmen und Schranken des Urheberrechts** gedeckt sind.

Es werden keine Garantien gegeben und auch keine Gewähr geleistet. Die Lizenz verschafft Ihnen möglicherweise nicht alle Erlaubnisse, die Sie für die jeweilige Nutzung brauchen. Es können beispielsweise andere Rechte wie **Persönlichkeits- und Datenschutzrechte** zu beachten sein, die Ihre Nutzung des Materials entsprechend beschränken.



# Contents

<b>1. Introduction</b>	<b>3</b>
<b>2. Magnetism</b>	<b>7</b>
2.1. Introduction . . . . .	7
2.2. Magnetic Fields . . . . .	7
2.2.1. Magnetization . . . . .	7
2.2.2. Total Magnetic Field . . . . .	9
2.2.3. Demagnetization Factors . . . . .	10
2.3. Definition of Coordinates and Units . . . . .	11
2.3.1. Coordinate Systems . . . . .	11
2.3.2. Units . . . . .	13
2.4. Total Magnetostatic Energy . . . . .	13
2.4.1. Contributing Forms of Energy . . . . .	13
2.4.2. Magnetic Anisotropy . . . . .	15
2.4.3. Magnetic Domain Formation and Single-Domain Particle . . . . .	16
2.5. Example: A Prolate Ellipsoid . . . . .	17
2.5.1. Stoner-Wohlfarth Model . . . . .	17
2.5.2. Three Basic Configurations . . . . .	17
2.5.3. Total Magnetostatic Energy . . . . .	18
2.5.4. State Progression and Hysteresis . . . . .	19
2.5.5. Discussion . . . . .	20
2.6. Magnetization States and Reversal Of Non-Ideal Samples . . . . .	23
2.6.1. Limits of Stoner-Wohlfarth Model . . . . .	23
2.6.2. Nano-Scale Magnetic Samples . . . . .	23
<b>3. Cantilever Magnetometry</b>	<b>25</b>
3.1. Introduction . . . . .	25
3.2. Methods Overview . . . . .	25
3.2.1. Atomic Scale . . . . .	25
3.2.2. Bulk Magnetization . . . . .	26
3.2.3. Cantilever Torque Magnetometry . . . . .	27
3.3. Dynamic Cantilever Magnetometry (DCM) . . . . .	28
3.3.1. Introduction . . . . .	28
3.3.2. Cantilever . . . . .	29
3.3.3. Damped Harmonic Oscillator . . . . .	30
3.4. Derivation of Resonant Frequency Shift . . . . .	30
3.4.1. Introduction . . . . .	30
3.4.2. Torque on the Cantilever . . . . .	32

3.4.3.	Minimization of Total Energy . . . . .	33
3.4.4.	Frequency Shift . . . . .	36
3.4.5.	Discussion . . . . .	37
3.4.6.	High Field Limit . . . . .	39
3.4.7.	Magnetization Curve . . . . .	40
3.5.	Derivation of Demagnetization Factors . . . . .	40
3.5.1.	Introduction . . . . .	40
3.5.2.	Demagnetization Factors for a Hexagonal Nanotube . . . . .	41
<b>4.</b>	<b>Experimental Setup</b>	<b>45</b>
4.1.	Introduction . . . . .	45
4.2.	Cantilever . . . . .	45
4.3.	Magnetic Sample . . . . .	47
4.3.1.	Introduction . . . . .	47
4.3.2.	Ni Nanotubes . . . . .	48
4.3.3.	CoFeB Nanotubes . . . . .	51
4.4.	Sample Fabrication . . . . .	53
4.4.1.	Introduction . . . . .	53
4.4.2.	Standard Procedure . . . . .	54
4.5.	Variations on Sample Fabrication . . . . .	55
4.5.1.	Introduction . . . . .	55
4.5.2.	Dual Beam Microscopy and Nano-Manipulation . . . . .	56
4.5.3.	Universal Sample-To-Cantilever Attachment Apparatus . . . . .	57
4.6.	Methods . . . . .	59
4.6.1.	Cryostat . . . . .	59
4.6.2.	Laser Interferometer . . . . .	59
4.6.3.	Experimental Procedure . . . . .	60
<b>5.</b>	<b>Data and Discussion</b>	<b>63</b>
5.1.	Introduction . . . . .	63
5.2.	DCM Measurements . . . . .	64
5.2.1.	Ni High Applied Field Data . . . . .	64
5.2.2.	Ni Low Applied Field Data . . . . .	65
5.2.3.	CoFeB High Applied Field Data . . . . .	67
5.2.4.	CoFeB Low Applied Field Data . . . . .	68
5.2.5.	Magnetization Curves . . . . .	70
5.3.	Discussion . . . . .	71
5.3.1.	Validity of Model . . . . .	71
5.3.2.	Saturation Magnetization And Net Anisotropy . . . . .	73
5.3.3.	Magnetization Curves . . . . .	73
5.3.4.	Hysteresis . . . . .	74
5.3.5.	Discontinuities In Frequency Shift . . . . .	75
5.3.6.	Discussion Of Frequency Shift . . . . .	76
5.4.	State Progression . . . . .	79
5.5.	Findings Review . . . . .	83

<b>6. Conclusions</b>	<b>85</b>
6.1. Summary . . . . .	85
6.2. Outlook . . . . .	87
<b>References</b>	<b>89</b>
<b>Appendices</b>	<b>97</b>
<b>A. Source Code Wolfram Mathematica</b>	<b>97</b>
A.1. Sample-On-Cantilever . . . . .	98
A.2. Demagnetization Factors . . . . .	100
A.3. Fit and Magnetization Curve . . . . .	104
<b>B. Sample Specifications</b>	<b>107</b>
B.1. Sample Specifications Ni . . . . .	108
B.2. Sample Specifications CoFeB . . . . .	109
<b>C. Periodic Table of Chemical Elements</b>	<b>111</b>
<b>Acknowledgements</b>	<b>IX</b>
<b>Curriculum Vitae</b>	<b>XIII</b>
Education And Relevant Work . . . . .	XIII
List of Publications . . . . .	XIV







Richard P. Feynman in 1959. *Getty Images*

*“There is plenty of room at the bottom.”*

—Richard P. Feynman



# 1. Introduction

In a today famous and most visionary talk on December 29, 1959—more than half a century ago—Richard P. Feynman did no less than proclaim the field of nanotechnology [1]. In his attempt to discuss “the problem of manipulating and controlling things on a small scale,” Feynman imagined down-scaling micro-manipulation to what we know as shadow-mask evaporation, optical lithography, or focused ion beam microscopy. But he even further described machines, which would not only operate self-reproducing, but mimicking and miniaturizing their very own assembly to finally bridge the gap between man-made micro-machining and what is known in theory as the molecular assembler, a hypothetical tool for bottom-up synthesis of atomic-sized structures.

Consequently, Feynman collected the diverse scientific disciplines we nowadays know were vastly impacted by the combination of resources and knowledge associated with nanotechnology. In medicine, he envisioned to “swallow the surgeon,” i.e. to put a nanometer-sized surgical robot inside a blood vessel to find its destination, or to enable localized intra-cellular drug delivery by small machinery. In chemistry, not only synthesizing new materials should be possible, but also direct visual chemical analysis. Great advances in microbiology would be enabled by the sheer fact of being able to “just *look at the thing!*”

Today, magnetic nanoparticles are used as contrast agents for medical magnetic resonance imaging (MRI), or to be magnetically accumulated in target areas such as organs and tumors for localized drug delivery and hyperthermia [2–6]. For the latter, i.e. heat treating, energy absorption from external alternating magnetic fields has been found to be dependent on the particle shape anisotropy, with nanowires heating tissue more efficiently than nanoparticles [7].

MRI in the form of magnetic resonance force microscopy (MRFM) has proven to allow for chemical contrast and thus possibly analysis of chemical compounds [8–10]. Not quite down to the level of DNA, as Feynman had in mind, but already on the low nanometer-scale, Degen et al. [11] could demonstrate enormous potential for MRFM as a true three-dimensional imaging technique for microbiological applications by imaging single viruses.

Most importantly, Feynman envisioned the modern schemes of down-scaling writing and handling of information. In his talk he takes us on the quest of writing the Encyclopedia Britannica on the head of a pin, calculating that each print-size dot would be demagnified to a size of 1000 atoms. Even more so, by encoding the letters and by estimating a number of  $5 \times 5 \times 5$  atoms per encoded bit, human knowledge (as of 1959) collected in “all the books in the world” could be written within a cube of about  $20 \mu\text{m}$  width—“which is the barest piece of dust that can be made out by the human eye. So there is *plenty* of room at the bottom!”

By comparing to human cells, which could not only store information as dense as 50 atoms per bit in DNA, but also “doing something about it,” Feynman went one step further to explain his ideas on miniaturizing the computer: In 1959, computers would “fill rooms.”—“Why can’t we make them very small,” he asked, and mentioned wiring of “10 to 100 atoms in diameter, and the circuits should be a few thousand angstroms across.”

More than 50 years later, nanotechnology has seen the realization of a twelve-atom bit<sup>a</sup>. The next generation of commercially available storage media reaches Feynman’s benchmark of about 100 atoms per bit<sup>b</sup> and transistor sizes in integrated circuits are in the order of just above 100 nm width<sup>c</sup>. Although being made of well-characterized materials, reducing the size of these components goes along with emerging size-dependent properties. Ultimately following the laws of quantum mechanics, different forces are of importance compared to the macroscopic world. In physics—yet merely following after Feynman’s far-sightedness—we set out for exploring these “strange phenomena that occur in complex situations.”

In this thesis, we focus on one particular aspect of nanotechnology, namely the understanding of magnetic states in nanometer-scale objects. Describing microscopic magnetization states and reversal is particularly important for the development of magnetic storage media. In order to further optimize information-bit density, innovative geometries involving magnetic nanowires have been suggested by Parkin et al. [12]. The realization of both writing and reading in such magnetic nanowires depends on the reliable induction and control of domain wall movement. In this thesis we intend to shed light on basic dynamic effects in similar structures.

Ferromagnetic nanotubes are the focus of this work due to their unique magnetic properties and unusual geometry. The reduced dimensionality of these structures manifests itself in magnetic configurations not present in macroscopic magnets (section 2.6.2). The magnetic samples that we are interested in are in the shape of a hollow prism with hexagonal cross-section and a very high aspect ratio. These structures avoid magnetization point singularities as present in solid magnetic cylinders, but support core-free magnetization states as a prerequisite for fast and controllable magnetization reversal. For this thesis, two different sets of magnetic samples are probed. One set of samples is processed to be Ni nanotubes, the other to be CoFeB nanotubes (section 4.3).

Dynamic cantilever magnetometry (DCM) allows us to investigate the weak magnetic response of individual magnetic nanotubes without averaging over an inhomogeneous ensemble. With this sensitive method we are able to study the magnetization states, magnetization reversal mechanisms, and demagnetization factors of single nanotubes dependent on the applied field and the alignment of the sample. The study of demagnetizing factors has been a classical topic in magnetism since the development of modern electrodynamics by Maxwell [13].

The advantages of our technique are the high precision of the associated frequency measurement and the potential of investigating arbitrary geometries, even at the nanometer scale. At the same time, interfering electrostatic and magnetostatic fields are entirely avoided by a purely

---

<sup>a</sup>A. Heinrich et al.: “Atomic-scale magnetic memory,” *IBM Research – Almaden*, 2012-01-05.

<sup>b</sup>S. Anthony: “Seagate hits 1 terabit per square inch, 60TB hard drives on their way,” *ExtremeTech*, 2012-03-20.

<sup>c</sup>Wikipedia: “Integrated circuit,” *Wikipedia, The Free Encyclopedia*, 2014-08-29.

optical readout. DCM is sensitive to the volume magnetization of the sample, instead of probing the total magnetic field including the stray field for instance.

An individual nanotube is affixed to the end of an ultrasoft cantilever, which is a mechanical oscillator exhibiting beam-like shape, clamped at one end, free at the other, and capable of deflection in one direction only in the fundamental oscillation mode. To fabricate the sample-on-cantilever system, individual nanotubes are chosen from their substrate under an optical microscope, and glued to the cantilever using a hydraulic micro-manipulator setup, allowing the handling of nanometer-scale samples (section 4.4). The torque acting between the magnetic nanotube and the applied field shifts the resonant frequency of the cantilever. Changes in the magnetization state can be tracked in timescales in the order of a few cantilever oscillation cycles.

This thesis is divided into four parts. In chapter 2 we establish the basic concepts of magnetism and introduce the coordinate systems used throughout the thesis. To explain phenomena such as magnetic anisotropy, or magnetic domain formation we consider the total magnetostatic energy of a given sample. Minimization of the energy yields the optimal angle of the magnetization within a magnetic particle, as shown for an important model system, the prolate ellipsoid. We review deviant magnetization states for samples with different geometry.

Chapter 3 introduces our experimental method, DCM, after reviewing other means of magnetometry. To later explain our data, we derive the cantilever resonant frequency shift as a response to an applied magnetic field and discuss found solutions. We also derive demagnetization factors to describe the shape anisotropy of our samples.

In chapter 4 we mention the components necessary to perform DCM measurements, from the physical properties of the cantilever to the experimental methods. Following in Feynman's footsteps, we illustrate bottom-up nanotube sample growth and fabrication methods including micro-manipulation and focused ion beam microscopy.

Finally in chapter 5 we show and discuss the findings of our measurements. We measure the shift of the cantilever resonant frequency as a function of both the applied field and the alignment of the sample in three basic configurations to characterize the sample anisotropy.

---

$k_0, l_e, \mu_0$	physical constants and quantities	italic lower case letters
$\theta, \Phi'$	angles	greek letters
$\mathbf{M}_s, \mathbf{H}$	vector physical quantities	italic boldface upper case letters
$M_s, V, H$	norm of physical quantities	italic upper case letters
$\hat{x}, \hat{z}'$	unit vector	lower case letters with hat
D	tensor physical quantity	sans-serif upper case letters
$\mathcal{H}$	quantum operator	calligraphy letters
$\mathcal{S}_i$	vector quantum operator	boldface calligraphy letters
$\boxed{1}$	name of sample-on-cantilever configuration	boxed number

---

Table 1.1. | Notation



## 2. Magnetism

### 2.1. Introduction

This brief introduction to the basic concepts of magnetism will closely follow the straightforward completeness of Skomski and Coey [14], the elaborate explanations of Morrish [15] and the unprecedented elegance of Aharoni [16].

First, the origin of magnetism, basic symbols and the fields involved in the description of magnetic samples are introduced. After establishing the coordinate systems as foundations on which the calculations in this theses are performed, the different interactions present in magnetic material are listed. They provide the basis for the reader to follow into the topics of magnetic anisotropy and domain formation. We consider the example of an ellipsoidal magnetic particle, which is an important model system to understand magnetization behavior in terms of the Stoner-Wohlfarth model. Finally, possible magnetization state and reversal schemes for non-ideal systems are laid out to form the theoretical prerequisites necessary to understand later experimental results.

### 2.2. Magnetic Fields

#### 2.2.1. Magnetization

The force amongst samples of magnetic material is strongest between specific regions of samples called magnetic poles. In 1789, Coulomb [17] discovered that these forces originate in two types of magnetic poles. There is a repellent force between two like, and an attractive force between two unlike magnetic poles. Isolated magnetic poles have never been observed in nature, but in unlike pairs instead, called magnetic dipoles. The magnetic dipole moment is defined as

$$\mathbf{m} \equiv m\mathbf{d},$$

where  $\mathbf{d}$  is a vector pointing from the negative (south) to the positive (north) pole, and  $m$  the strength of an isolated pole [15].

A magnetic field  $\mathbf{H}$  applied to *any* material leads to the acquisition of a magnetic dipole moment inside that material. The magnetic dipole moment per unit volume is defined as the

magnetization  $\mathbf{M}$ . The response of the magnetization to the total field  $\mathbf{H}'$  (2.2) inside most (i.e. diamagnetic, see below) materials is linear:

$$\mathbf{M} = \chi \mathbf{H}' \quad (2.1)$$

Exceptions to this rule are discussed in the following. The proportionality constant  $\chi$  is known as the susceptibility. In case the magnetic vectors are not parallel the susceptibility is a second rank tensor [16].

The microscopic origin of magnetic dipoles is found in the orbital and spin angular momentum of electrons and to minor extent from the nuclear magnetic moment. Thus, in any material, electrons and nuclei are influenced by a magnetic field. This property is called diamagnetism, distinguishable by  $\chi < 0$ . Any other form of magnetism exhibits  $\chi > 0$  and a permanent magnetic moment. In case of small or no coupling (small  $\chi$ ) between the magnetic moments, the material is called paramagnetic. For large coupling (large  $\chi$ ), when the interaction between the constituent magnetic moments is strong, the magnetic moments become highly ordered: If the moments are aligned parallel, the material is called ferromagnetic. If they are aligned anti-parallel, with no net moment, the material is anti-ferromagnetic, but with a net moment, it is ferrimagnetic ([14, 15] and figure 2.1).

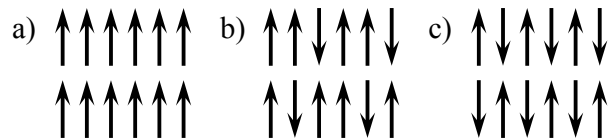


Figure 2.1. | Illustration of a) ferromagnetic, b) ferrimagnetic, and c) anti-ferromagnetic order. The arrows represent microscopic magnetic dipole moments. Illustration reproduced from [14].

In the latter three cases of highly ordered magnetic materials, here summarized as ferromagnets, changes in the magnetization are mostly due to rotations of the net magnetization vector. Namely, ferromagnets are made of magnetic *domains*, small regions, each spontaneously magnetized as depicted in figure 2.1. The net magnetization of the entire sample then is the vector sum of the magnetization of each domain. An applied field changes the domain arrangement and thus the net magnetization, which then can even assume zero. For ferromagnets, the susceptibility is not a constant, but a function of the applied field, additionally dependent on the temperature, the size, shape and history of the considered sample [14, 15]. For these magnets the definition of the susceptibility is generalized to

$$\chi \equiv \left. \frac{\partial M}{\partial H} \right|_{H,T}$$

(also called effective susceptibility) evaluated at a specific applied field  $H$  and temperature  $T$ . The magnetization cannot follow the applied field instantaneously in the presence of metastable energy minima and barriers associated with the microstructure of the ferromagnet, which gives rise to magnetic hysteresis [14].

The function  $M(H)$  is known as the *limiting* hysteresis curve, see figure 2.2. The curve is obtained by applying a large enough field to the ferromagnet until the saturation magnetization  $M_s$  is reached and is reproducible in consecutive field cycles. For a fully demagnetized magnet,



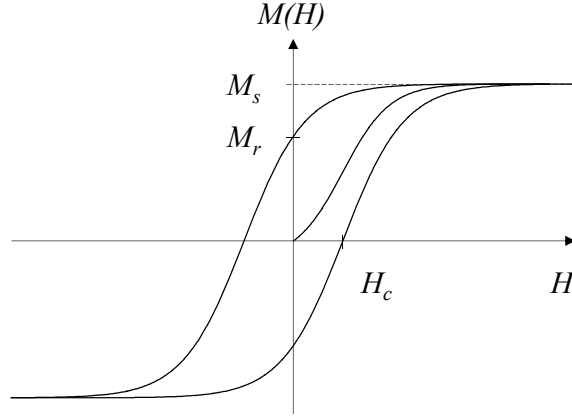


Figure 2.2. | Schematic diagram of the limiting hysteresis curve of a typical ferromagnetic material, also showing the virgin curve, the saturation magnetization  $M_s$ , the remanence  $M_r$ , and the coercivity  $H_c$ . Diagram reproduced from [16].

the curve is starting at the origin, known as virgin curve. If the field is increased and decreased before the limiting curve is achieved, a *minor* hysteresis curve is traced. It is apparent that the magnetization  $M$  is not proportional to the applied field  $H$ , in particular it may be non-zero at  $H = 0$ , the so-called remanence  $M_r$ . The field for which the magnetization is zero is called coercivity  $H_c$ . The higher the remanence  $M_r$  of the magnet, the higher the coercivity to “force” the magnetization into reversal [16]. For more details on hysteresis refer to section 2.5.4 where an example of an ellipsoidal magnetic particle is described.

The saturation magnetization  $M_s$  is an intrinsic property of the material. It is a function of the temperature, where above the Curie temperature,  $T_C$ ,  $M_s$  becomes zero at zero applied field: All ferromagnets become paramagnetic above  $T_C$  [16].

### 2.2.2. Total Magnetic Field

The magnetization  $\mathbf{M}$  *inside* a magnetic material is the result of an applied field  $\mathbf{H}$  *outside* the material (as implied in equation (2.1)). More precisely, the externally applied magnetic field  $\mathbf{H}$  is distinguished from the total, internal magnetic field  $\mathbf{H}'$  by the demagnetizing field  $\mathbf{H}_{dm}$  [14]:

$$\mathbf{H}' = \mathbf{H} + \mathbf{H}_{dm} \quad (2.2)$$

$\mathbf{H}_{dm}$  can be found by solving the magnetostatic Maxwell equations [13], which is discussed in more detail in section 2.2.3.

The divergenceless magnetic flux density  $\mathbf{B}$ , usually used in Maxwell’s equations, is defined by

$$\mathbf{B} \equiv \mu_0(\mathbf{H}' + \mathbf{M}) \quad (2.3)$$

with the vacuum permeability  $\mu_0 \equiv 4\pi \cdot 10^{-7} \text{ V s / (A m)}$ , taking into account both internal and external field contributions. To clarify these contributions, with the help of figure 2.3, consider a point P inside a bar magnet. The magnet has been uniformly magnetized by an external applied

field  $\mathbf{H}$ , which is now switched off (i.e.  $\mathbf{H}' = \mathbf{H}_{dm}$ ), see figure 2.3a. Uncompensated surface moments<sup>a</sup> (poles) of the magnetization (depicted in figure 2.3b) produce an inhomogeneous field  $\mathbf{H}_{dm}$ , which is called demagnetizing field inside, and stray field outside the magnet [15]. Relation (2.3) is evaluated at point P as illustrated in figure 2.3c, resulting in the flux density  $\mathbf{B}$  (figure 2.3d), obeying Maxwell's equation  $\nabla \cdot \mathbf{B} = 0$  [14].

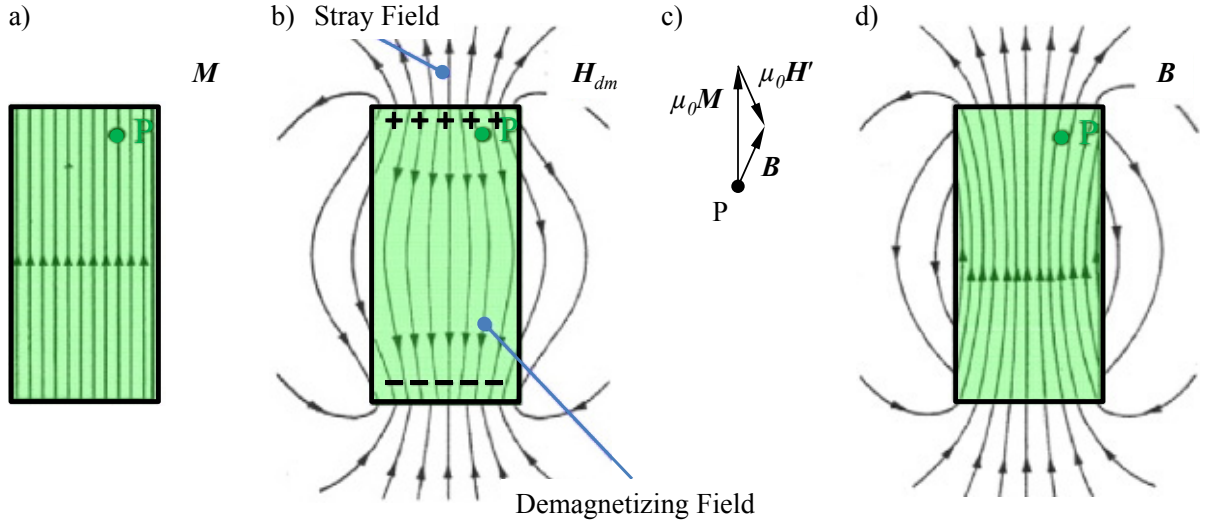


Figure 2.3. | Illustration of a bar magnet (in green), depicting a) the magnetization  $\mathbf{M}$ , b) the demagnetizing and stray field  $\mathbf{H}_{dm}$ , and d) the magnetic flux density  $\mathbf{B}$ , evaluated at point P inside the magnet (c). Illustration similar to [14], adapted from [18].

With equation (2.1), the relation (2.3) simplifies to

$$\mathbf{B} = \mu \mathbf{H}',$$

where  $\mu \equiv \mu_0(1 + \chi) \equiv \mu_0 \mu_r$  is called the magnetic permeability [16].

### 2.2.3. Demagnetization Factors

In order to determine the demagnetizing field  $\mathbf{H}_{dm}$  of equation (2.2) one can solve the magnetostatic Maxwell equations [13], notably

$$\nabla \times \mathbf{H}' = 0 \tag{2.4a}$$

$$\text{and } \nabla \cdot \mathbf{B} = 0. \tag{2.4b}$$

To proceed one can define the scalar magnetic potential  $U_{mag}$  (for any magnetic field) by

$$\mathbf{H}' \equiv -\nabla U_{mag} \tag{2.5}$$

and substitute expression (2.3) in (2.4b) to get

$$\nabla^2 U_{mag} = \nabla \cdot \mathbf{M}$$

<sup>a</sup>Additional contributions to this field come from uncompensated volume moments, arising from an inhomogeneous magnetization, which for clarity are not shown in the illustration.

inside the magnetic material. The relation obeys Maxwell's boundary conditions of components  $H_{\parallel}$  and  $B_{\perp}$  being continuous parallel and perpendicular to the surface between two magnetic materials. With these boundary conditions, in principle one can solve for  $U_{mag}(\mathbf{M}(\mathbf{r}), \mathbf{r})$  for any magnetization and for the whole space. Particularly in the case of uniform magnetization, where  $\nabla \mathbf{M} = 0$ , once  $U_{mag}$  is known we can go back and find  $\mathbf{H}_{dm}$  with equation (2.5), for the volume of the magnetic sample.  $\mathbf{H}_{dm}$  is a linear function of the components of  $\mathbf{M}$ , so we may write

$$\mathbf{H}_{dm} \equiv -\mathbf{D} \circ \mathbf{M}, \quad (2.6)$$

and hereby define the demagnetization factor tensor  $\mathbf{D}$ , with  $\text{Tr } \mathbf{D} \equiv 1$  [16].

In uniformly magnetized ellipsoids of revolution calculation of  $\mathbf{H}_{dm}$  yields a *homogeneous* dipolar demagnetizing field. Symmetry leads to the principal-axis representation of the demagnetization factor tensor:

$$\mathbf{H}_{dm} = - \begin{pmatrix} D_x & 0 & 0 \\ 0 & D_y & 0 \\ 0 & 0 & D_z \end{pmatrix} \circ \mathbf{M} \quad (2.7)$$

The matrix elements are the demagnetization factors  $D_x$ ,  $D_y$ , and  $D_z$ , with  $D_x + D_y + D_z = 1$ . They correspond to the geometrically defined demagnetization factors  $D_a$  and  $D_b$  of the polar and equatorial semi-axes  $a$  and  $b$  of the ellipsoid, depending on the orientation of the ellipsoid, see figure 2.4 (upper right) and table 2.1 (in section 2.5.2). For arbitrary orientations of the ellipsoid one can always apply a rotation matrix to the demagnetization factor tensor. In the special case, where the magnetization  $\mathbf{M}$  and applied field  $\mathbf{H}$  are both parallel to one of the ellipsoid semi-axes, the total field (2.2) is given by  $\mathbf{H}' = \mathbf{H} - D_i \mathbf{M}$  ( $i \in \{x, y, z\}$ ) [14].

For uniformly magnetized, but arbitrarily shaped magnetic materials, even including cavities for instance, one can still calculate the demagnetization factors by considering an average demagnetizing field. Using a field average over the whole volume of the sample leads to the so called *magnetometric* demagnetization factors [16].

Formulae for the calculation of demagnetization factors (and fully derived examples) can be found in any of [14–16], reliably referring to Osborn [19]. Within the scope of this thesis the reader may refer to section 3.5, where the cases important for the interpretation of our data are considered.

## 2.3. Definition of Coordinates and Units

### 2.3.1. Coordinate Systems

The recent definitions of physical quantities have been self-consistent in terms of the used coordinate systems. In this section a more generalized set of coordinate systems is introduced to ensure consistency within the thesis.

In figure 2.4 two sets of Cartesian coordinates  $(x, y, z)$  and  $(x', y', z')$  are defined, together with their spherical coordinate equivalents  $(r, \Theta, \Phi)$  and  $(r', \Theta', \Phi')$ . The primed and unprimed coordinate systems are related by the angle  $\theta$ , namely the primed coordinates are rotated with respect to the unprimed coordinates by  $\theta$  around the  $x$  axis. Usually, unless otherwise specified, the applied magnetic field vector  $\mathbf{H}$  is fixed along the  $z$  axis. The magnetization  $\mathbf{M}$  is defined as a three-dimensional vector

$$\mathbf{M} \equiv M(\sin \Theta' \sin \Phi' \cdot \hat{x}' + \sin \Theta' \cos \Phi' \cdot \hat{y}' + \cos \Theta' \cdot \hat{z}') \quad (2.8)$$

The primed coordinates serve to describe magnetic samples and the magnetization therein. The primed axes may or may not be aligned to an axis of symmetry of the—in general arbitrary—magnetic sample. However, ellipsoids of revolution are frequently used as a model system for they provide analytically solvable problems (in figure 2.4, upper right). These ellipsoids can be defined self-consistently by the length of their polar and equatorial semi-axes,  $a$  and  $b$ . There are three basic configurations [1], [2], and [3] for an ellipsoid of revolution to be placed in a sample-independent coordinate system  $(x', y', z')$ , with its principal axes each aligned to one of the coordinate directions (see ellipsoids in figure 2.6, and table 2.1).

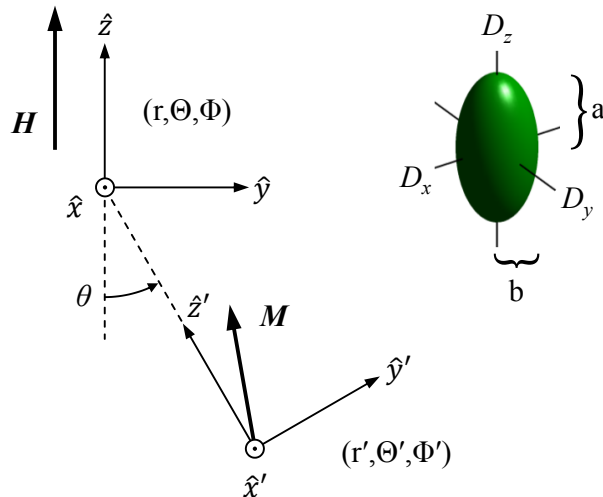


Figure 2.4. | Illustration of sets of primed and unprimed coordinate systems. Two sets of cartesian coordinates  $(x, y, z)$  and  $(x', y', z')$  are defined, together with their spherical coordinate equivalents  $(r, \Phi, \Theta)$  and  $(r', \Phi', \Theta')$ . Unprimed coordinates are rotated by the angle  $\theta$  around the  $x$  axis. The applied field  $\mathbf{H}$  is fixed along the  $\hat{z}$  direction. The three-dimensional magnetization vector is shown in projection onto the  $y'-z'$ -plane. The primed coordinates serve to describe magnetic samples, drawn schematically, e.g. prolate ellipsoids of revolution, with polar and equatorial semi-axes  $a$  and  $b$ , and principle-axis demagnetization factors  $D_x$ ,  $D_y$ , and  $D_z$ .

In literature [14–16, 20–22] the magnetization vector often is projected onto the  $y'-z'$ -plane, the necessary coordinates reduce to two dimensions with the polar angle  $\Theta'$  and the magnitude  $M$  only. Then the angle between magnetization and applied field is  $(\theta - \Theta')$ . Note, that the symbol  $\theta$  in general is not related to otherwise familiar spherical coordinate notation.

### 2.3.2. Units

In SI units, the magnetic flux density  $\mathbf{B}$  is measured in teslas T. In Gaussian-cgs units,  $\mathbf{B}$  is measured in gauss G. The conversion is  $1 \text{ T} = 10^4 \text{ G}$ . The applied magnetic field (also called magnetizing field)  $\mathbf{H}$  and the magnetization  $\mathbf{M}$  are measured in amperes per metre A/m in SI units, and in oersteds Oe in cgs units. The conversion here is  $1 \text{ A/m} = 4\pi \cdot 10^{-3} \text{ Oe}$ . In some older references, including Kittel [23], gauss is also used for the saturation magnetization  $\mathbf{M}_s$ , despite the official introduction of oersted in 1930 [24]. Because of relation (2.3), the product of either  $\mathbf{M}$  or  $\mathbf{H}$  with the vacuum permeability  $\mu_0 = 4\pi \cdot 10^{-7} \text{ Vs/(A m)}$  has the SI unit tesla. To summarize [25]:

$$[\mathbf{B}] = 1 \text{ G} = 10^{-4} \text{ T}$$

$$[\mathbf{M}] = [\mathbf{H}] = 1 \text{ Oe} = \frac{10^3}{4\pi} \frac{\text{A}}{\text{m}}$$

## 2.4. Total Magnetostatic Energy

### 2.4.1. Contributing Forms of Energy

The magnetic domain structure, the onset of magnetization reversal, and the rotation of the magnetization within a given sample is determined by minimizing the total magnetostatic energy of the sample (see [15, 16] following Brown [26]).

The total magnetostatic energy of a magnetic particle in its most general form is given by

$$E_{tot} = E_Z + E_{ms} + E_{ex} + E_K + E_\sigma + E_0, \quad (2.9)$$

where the used symbols have the following meaning [15]:

$E_Z$ : The *Zeeman energy*  $E_Z$  is the potential energy of a magnetic particle represented by its net magnetization  $\mathbf{M}$  in an applied field  $\mathbf{H}$ :

$$E_Z = -\mu_0 \int \mathbf{M} \cdot \mathbf{H} \, dV$$

It describes the interaction of the magnetic dipoles within a particle of volume  $V$  with the applied field [14]. For a uniformly magnetized particle with saturation magnetization  $\mathbf{M}_s$  using equation (2.8) and a uniformly applied field, it is sufficient to rewrite the expression for the Zeeman energy to

$$E_Z = -\mu_0 V M_s H (\sin \theta \sin \Theta' \cos \Phi' + \cos \theta \cos \Theta') \quad (2.10)$$

In case of purely rotational displacement, interaction between magnetic dipoles is measurable as a torque  $\boldsymbol{\tau}$  acting on each magnetic dipole moment towards the applied field. The infinitesimal

vector  $\partial\boldsymbol{\alpha}$  between arbitrary  $\boldsymbol{M}$  and  $\boldsymbol{H}$  has the magnitude  $\partial\alpha$  and the direction of the rotation axis is  $\hat{\alpha} = \frac{\boldsymbol{M} \times \boldsymbol{H}}{\|\boldsymbol{M} \times \boldsymbol{H}\|}$ . From the Zeeman energy  $E_Z = -\mu_0 V M_s H \cos \alpha$ , the torque then is

$$\boldsymbol{\tau} = -\frac{\partial E_Z}{\partial \boldsymbol{\alpha}} = -\frac{\partial E_Z}{\partial \alpha} \cdot \hat{\alpha} = \mu_0 V \boldsymbol{M} \times \boldsymbol{H} \quad (2.11)$$

[27] and for uniform fields becomes

$$\boldsymbol{\tau} = \mu_0 V M_s H ((\cos \theta \sin \Theta' \cos \Phi' - \sin \theta \cos \Theta') \cdot \hat{x} - \sin \Theta' \sin \Phi' \cdot \hat{y})$$

Note, that there is no component of the torque parallel to the applied field.

$E_{ms}$ : The *magnetostatic self-energy*  $E_{ms}$  of a permanent magnet is

$$E_{ms} = -\frac{\mu_0}{2} \int \boldsymbol{M} \cdot \boldsymbol{H}_{dm} \, dV. \quad (2.12)$$

This energy represents the mutual magnetostatic interaction of the elementary magnetic dipoles inside the volume  $V$  of the magnetic material and is derived by pairwise summation (factor  $\frac{1}{2}$ ) of the Coulomb potentials of each magnetic dipole in the material [14]. The magnetostatic self-energy can be attributed to two physical causes, which also cause the demagnetizing field  $\boldsymbol{H}_{dm}$  (see figure 2.3): First, uncompensated surface moments, and second, uncompensated volume moments, arising from an inhomogeneous magnetization  $\boldsymbol{M}$  inside the volume of the magnetic material [15].

To calculate the magnetostatic self-energy for a uniformly magnetized ellipsoid, we use the magnetization as defined in equation (2.8). By substituting equation (2.7) in (2.12),  $E_{ms}$  simplifies to

$$E_{ms} = \frac{\mu_0}{2} V M_s^2 ((D_x \sin^2 \Phi' + D_y \cos^2 \Phi') \sin^2 \Theta' + D_z \cos^2 \Theta') \quad (2.13)$$

The demagnetization factors characterize the dependence of the energy on the shape of the magnetic sample, which is why expression (2.13) is also referred to as *shape anisotropy energy*, see section 2.4.2.

$E_{ex}$ : The *exchange energy*  $E_{ex}$  is a quantum phenomenon of electrostatic origin, important for both sub-domain magnetic dipole-dipole alignment and temperature dependence of a ferromagnet. Its magnitude is determined by the Heisenberg interaction Hamiltonian

$$\mathcal{H} = -\frac{1}{\hbar^2} \sum_{i,j} J_{ij} \boldsymbol{S}_i \cdot \boldsymbol{S}_j$$

using Planck's constant  $2\pi\hbar = 6.6261 \cdot 10^{-34}$  Js, the interaction strength constants  $J_{ij}$ , and the three-component spin operators  $\boldsymbol{S}_{i,j}$ . A positive or negative sign of  $J_{ij}$  determines whether nearest neighbor magnetic dipoles align parallel or anti-parallel (then called ferro- or anti-ferromagnetism). The model may be solved within a mean-field approximation, which gives results equivalent to the behavior of a single spin in a magnetic field. From this model an expression for the Curie temperature  $T_C$  can be derived [14].

$E_K$ : The *magneto-crystalline anisotropy energy*  $E_K$  is related to intrinsic crystalline lattice properties. Commonly, in a phenomenological approach, the energy is expressed in a power series of the angle between magnetization and principal axis of the crystal. The magnitude of the energy scales with the anisotropy constants  $K_m$ , which are the coefficients of the expansion to  $m$ th order. There is no local symmetry for non-crystalline particles, thus the magneto-crystalline anisotropy energy remains undefined [14, 15].

$E_\sigma$ : The *magneto-elastic energy*  $E_\sigma$  is a contribution to the total energy originating from the interaction of magnetization and strain. Like the magneto-crystalline anisotropy energy it depends on the crystalline directions of the magnetic material, and is therefore zero in non-crystalline structures [15].

$E_0$ : Finally, there may be an additive energy  $E_0$ , for example accounting for sample inhomogeneities, like geometric structure imperfections, or crystal lattice defects [14].

### 2.4.2. Magnetic Anisotropy

Magnetic hysteresis (figure 2.2) is caused by metastable energy minima associated with preferred magnetization directions (see section 2.5.4). The presence of energy barriers between these minima can be attributed to microstructural properties of the magnetic material and any applied field. The directional dependence of the net magnetization within a magnetic domain is called magnetic anisotropy. For more details on the associated energies see section 2.4.1.

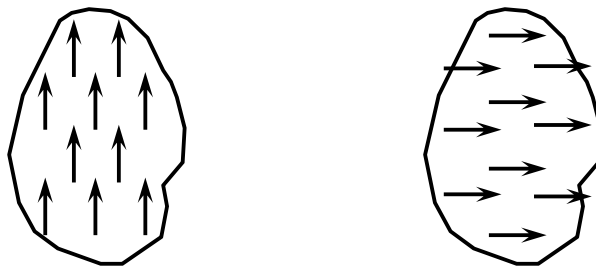


Figure 2.5. | Illustration of the “easy” (left) and “hard” (right) magnetization direction due to shape anisotropy in a nanometer-scale magnetic particle. The arrows represent microscopic magnetic dipole moments. Illustration adapted from [14].

There are several sources for magnetic anisotropy, mainly due to the crystalline structure of the magnetic material. The source for *crystalline anisotropy* is the crystalline electrostatic field, which interacts with electrons in partially filled atomic shells. Crystalline anisotropy then arises from spin-orbit coupling of these aspherical electron orbits to the magnetization, such that the electron orbits are linked to the crystalline structure. The associated magneto-crystalline anisotropy energy  $E_K$  may exceed other typical anisotropy energies by an order of magnitude, but is small compared to the exchange energy  $E_{ex}$ . In effect the *magnitude* of the magnetization is determined almost only by the exchange energy, but the *direction* of the magnetization is given by the anisotropy energy [14, 16]. Directions of the magnetization, in which the anisotropy energy has a local minimum, are called “easy”, whereas directions in which the anisotropy energy has a local maximum, are called “hard”.

In non-crystalline nanometer-scale aspherical magnetic particles, *shape anisotropy* is most dominant. This type of anisotropy is associated with the magnetostatic self-energy  $E_{ms}$  (2.12), where depending on the shape of the magnetic particle uncompensated magnetic moments lead to a directional dependence of the net magnetization. Therefore the magnetostatic self-energy is scaled by the shape-dependent demagnetization factors  $D_i$  of the magnetic particle together with the magnetization direction, which is why expression (2.13) is also referred to as shape anisotropy energy. For symmetric particles, e.g. a prolate ellipsoid of revolution as in figure 2.4, where two demagnetization factors are equivalent, corresponding to two equivalent equatorial semi-axes, the shape anisotropy is called *uniaxial*, and the magnetostatic self-energy can be written in terms of only one demagnetization factor.

In figure 2.5 the “easy” (on the left) and “hard” (on the right) magnetization directions (or axes) due to shape anisotropy are illustrated. The magnitude of the net magnetization is equal in each of the magnetic dipole moment configurations. But the magnetostatic self-energy is lower in case of the magnetization being aligned along the easy axis, due to the reduced demagnetizing field, see equation (2.12), together with figure 2.3 [14]. By comparison of two different demagnetization factors for two different axes of the magnetic particle it is possible to distinguish between an easy and a hard axis:  $D_{easy} < D_{hard}$

### 2.4.3. Magnetic Domain Formation and Single-Domain Particle

The magnetized state of macroscopic magnets is determined by their net magnetization and demagnetizing field, and thus by the magnetostatic self-energy  $E_{ms}$ , see equation (2.12). In ferromagnets a lower energy state can be achieved by the formation of magnetic domains, each individually magnetized in different directions, averaging to a macroscopic net magnetization of the sample, which can assume any value between zero and saturation magnetization. An applied magnetic field rotates the magnetization of each domain towards its direction, and for sufficiently large applied fields the sample is uniformly magnetized and will behave as a single-domain particle with saturation magnetization  $\mathbf{M}_s$  [14–16].

The local order of the magnetic dipoles within a domain is governed by the exchange energy  $E_{ex}$ . The forces resulting from the exchange energy are much stronger, but also more short ranged compared to the force exerted by the demagnetizing field. On a range much larger than nearest neighbors magnetic dipoles, inhomogeneous perturbations in the alignment of the magnetic dipoles can be present.

Gain in magnetostatic self-energy by domain formation always competes against the exchange and crystalline anisotropy energy stored in the resulting domain walls. In nanometer-scale magnetic particles the cost in exchange energy due to the formation of domain walls is higher than the gain in magnetostatic self-energy, even in the presence of uncompensated surface poles. There is a critical single-domain radius of a spherical ferromagnetic particle below which domain formation is suppressed: For cobalt this radius is around 34 nm, and only 16 nm for nickel [14]. Both for magnetic particles below that size, and for thin magnetic films with thicknesses below the numbers given, as an estimation, no domain walls are expected.



To explain the formation of domains, one needs to minimize the total magnetostatic energy. This is usually done in a continuum approximation, where the magnetization is a continuous function of space  $\mathbf{M}(\mathbf{r})$ . Only in few cases the minimization procedure leads to analytic solutions [14].

For this thesis, one example is introduced (section 2.5) and the minimization procedure carried out (section 3.4), retrieving the optimal angle of the magnetization within a single-domain particle in an applied field.

## 2.5. Example: A Prolate Ellipsoid

### 2.5.1. Stoner-Wohlfarth Model

In single-domain particles the exchange energy is the dominant interaction. Ideally all magnetic dipoles are aligned so there is no spatial dependence of the magnetization, and the exchange energy becomes constant throughout the volume of the magnetic material. The magnetization then is always the saturation magnetization and can rotate coherently, i.e. uniformly as a whole, within the magnetic particle. Coherent rotation of the magnetization is understood as opposed to incoherent rotation, where magnetization reversal nucleates by localized or delocalized instabilities of the initial magnetization. Note, that nucleation and incoherent rotation are generally independent of the single-domain character of a magnetic particle [14, 16]. The assumption of coherent rotation of the saturation magnetization within non-interacting particles is known as the Stoner-Wohlfarth model [20].

Minimization of the total magnetostatic energy  $E_{tot}$  yields the optimal angle of the saturation magnetization  $\mathbf{M}_s$  between the applied field  $\mathbf{H}$  and the easy axis of the magnetic particle. That easy axis may be defined by crystalline anisotropy, but in case of non-crystalline material only shape anisotropy is of importance. Since the mathematical treatment in the minimization procedure of both anisotropies is similar, we will consider only shape anisotropy here. The exchange energy is a constant within the assumptions of the Stoner-Wohlfarth model, so it will not enter in the calculation.

### 2.5.2. Three Basic Configurations

One can find solutions to the energy minimization problem for magnetic particles in the shape of ellipsoids of revolution in any alignment with respect to the sample-independent coordinates  $(x', y', z')$  (see figure 2.6). However, we focus on special cases, to illuminate the general behavior. Prolate ellipsoids can be described by their polar and equatorial semi-axes  $a$  and  $b$ , and by the corresponding geometrical demagnetization factors  $D_a$  and  $D_b$ . There are three basic configurations of aligning the principle axes of such an ellipsoid to the sample-independent coordinates  $(x', y', z')$  with corresponding demagnetization factors  $D_x$ ,  $D_y \equiv D_{\perp}$ , and  $D_z \equiv D_{\parallel}$ .

The symbols  $D_{\perp}$  and  $D_{\parallel}$  are used for demagnetization factors in  $\hat{y}'$ - and  $\hat{z}'$ -direction, respectively. These demagnetization factors are convenient for describing our experimental results, and can be made of any of the geometrical demagnetization factors characteristic for the considered sample. By realizing the three configurations in experiment, we can measure uniaxial anisotropy in the  $y'$ - $z'$ -plane, expecting different behavior in each configuration. Following scheme unfolds for the three basic configurations of a prolate ellipsoid of revolution:

Coordinate Directions	Ellipsoid Semiaxes			Demagnetization Factors		
	$\hat{x}'$	$\hat{y}'$	$\hat{z}'$	$D_x$	$D_y \equiv D_{\perp}$	$D_z \equiv D_{\parallel}$
Configuration <span style="border: 1px solid black; padding: 0 2px;">1</span>	$b$	$b$	$a$	$D_b$	$D_b$	$D_a$
Configuration <span style="border: 1px solid black; padding: 0 2px;">2</span>	$b$	$a$	$b$	$D_b$	$D_a$	$D_b$
Configuration <span style="border: 1px solid black; padding: 0 2px;">3</span>	$a$	$b$	$b$	$D_a$	$D_b$	$D_b$

Table 2.1. | List of symbols used to describe three basic configurations for an ellipsoid of revolution to be placed in a sample-independent coordinate system  $(x', y', z')$  with the principal axes each aligned to one of the coordinate directions. The symbols  $D_{\perp}$  and  $D_{\parallel}$  are used for demagnetization factors perpendicular (in  $\hat{y}'$ -direction) and parallel to the  $\hat{z}'$ -direction.

### 2.5.3. Total Magnetostatic Energy

In figure 2.6 is depicted, how the principal axes of a prolate ellipsoid are aligned to the coordinate system  $(x', y', z')$  in three basic configurations in accordance with table 2.1. The coordinates are as shown in figure 2.4. The total magnetostatic energy of an ellipsoid of revolution then is

$$\begin{aligned}
E_{tot} &= E_Z + E_{ms} \\
&= -\mu_0 V M_s H (\sin \theta \sin \Theta' \cos \Phi' + \cos \theta \cos \Theta') \\
&\quad + \frac{\mu_0}{2} V M_s^2 ((D_x \sin^2 \Phi' + D_y \cos^2 \Phi') \sin^2 \Theta' + D_z \cos^2 \Theta')
\end{aligned} \tag{2.14}$$

from the relations for the Zeeman energy  $E_Z$  (2.10) and the magnetostatic self-energy  $E_{ms}$  (2.13). Other energy terms of (2.9) are ignored, specifically, since the exchange energy is a constant and the sample material is assumed to be homogeneous, non-crystalline, and unstrained.

To illustrate the optimal angle for the magnetization at lowest energy, we choose the applied field  $\mathbf{H}$  to be fixed and positive in  $\hat{z}'$ -direction ( $\theta = 0^\circ$ ). Other alignments of the applied field to one of the axes  $x'$  or  $y'$  can be considered by looking at the three basic configurations under cyclic permutation of the coordinates. To depict the energy landscape, the magnetization  $\mathbf{M}$  of (2.8) is chosen to rotate with either  $\Phi' = 0$  or  $\Theta' = \frac{\pi}{2}$  fixed (i.e. within the  $y'$ - $z'$ -plane, or the  $x'$ - $y'$ -plane, respectively). For the cases considered here, the total energy can then be simplified to the reduced energy

$$e_{tot} \equiv \frac{2E_{tot}}{\mu_0 V M_s^2} = \begin{cases} -\frac{2H}{M_s} \cos \Theta' + D_{\perp} \sin^2 \Theta' + D_{\parallel} \cos^2 \Theta' & \text{if } \Phi' = 0 \quad \Leftrightarrow \quad y'-z'\text{-plane} \\ D_x \sin^2 \Phi' + D_y \cos^2 \Phi' & \text{if } \Theta' = \frac{\pi}{2} \quad \Leftrightarrow \quad x'-y'\text{-plane} \end{cases}$$

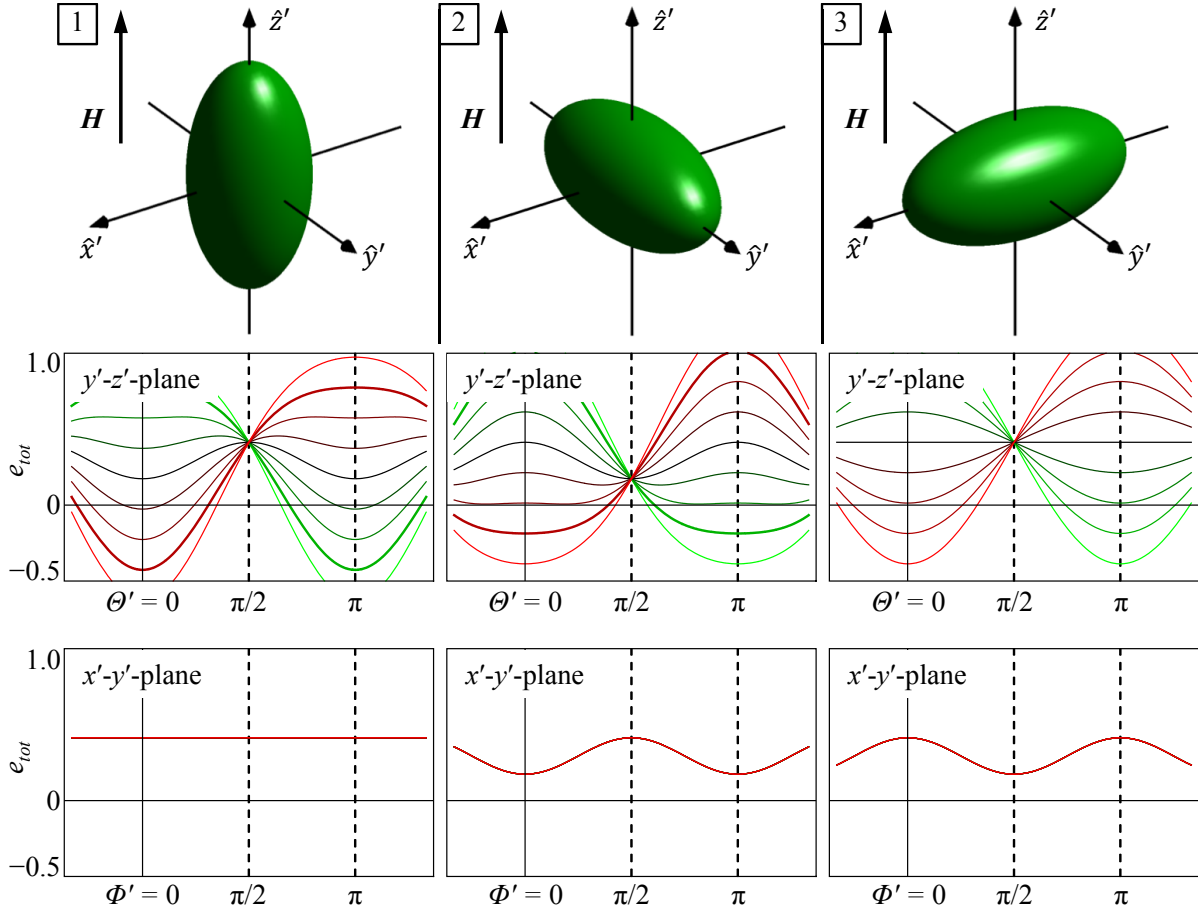


Figure 2.6. | Illustration and graphs of the total magnetostatic energy of prolate ellipsoids. In the upper row is depicted, how the principal axes of a prolate ellipsoid are aligned to the coordinate system  $(x', y', z')$  in three basic configurations in accordance with table 2.1. The lower two rows for each configuration show the reduced energy  $e_{tot} \equiv \frac{2E_{tot}}{\mu_0 V M_s^2}$  vs. the angles  $\Theta'$  and  $\Phi'$ , respectively, as a function of the applied field. Different values of the applied field are in color, from negative (green), through zero (black), to a higher positive field (red), symmetrically around zero field. The thick line is the coercivity.

The calculation of the energy minima is carried out in section 3.4. Here, a qualitative analysis is performed.

### 2.5.4. State Progression and Hysteresis

In figure 2.6, the middle row for each configuration shows the reduced energy  $e_{tot}$  vs. the angle  $\Theta'$  (the polar angle of the magnetization) as a function of the applied field, for  $\Phi' = 0$  (the  $y'-z'$ -plane). The lower row shows the reduced energy  $e_{tot}$  vs. the angle  $\Phi'$  (the azimuthal angle of the magnetization) for  $\Theta' = \frac{\pi}{2}$  (the  $x'-y'$ -plane). For all graphs, the applied field is increased stepwise from negative (green), through zero (black), to a higher positive field (red), symmetrically around zero field. The thick line is the coercivity.

The physical system always assumes a state in which the total magnetostatic energy has a local minimum. That state is determined by the direction of the magnetization, which again is dependent on the applied field direction and the shape of the magnetic sample. If we suppose, that in each graph in figure 2.6 the magnetic sample was initialized to be in the green minimum by applying a high enough negative field, we can follow the magnetization state progression with increasing applied field by following the angle of the local energy minimum. The coercivity  $H_c$  is that applied field, which marks the onset of magnetization reversal, that is where energy minima become metastable. In the presence of shape anisotropy only, the coercivity is

$$H_c = \begin{cases} |M_s(D_\perp - D_\parallel)| & \text{if } \Phi' = 0 \\ |M_s(D_x - D_y)| & \text{if } \Theta' = \frac{\pi}{2} \end{cases} \quad (2.15)$$

[14]. Ultimately the magnetization always is rotated towards the applied field, like in the initial state, but in positive direction. The procedure is repeatable symmetrically and generally leads to the hysteresis curve for the magnetization, similar to figure 2.2.

Observing hysteretic behavior is the observation that a measurement of a physical quantity is giving different results under the influence of the sample history. In an energy picture, the existence of hysteresis corresponds to a regime in which there are two or more solutions to the energy minimization problem<sup>b</sup> (local minima). The physical system always assumes a state of minimal energy and energy barriers prevent jumps from one solution to another. The energy landscape here is a function of the applied field and the magnetization assumes an optimal angle accordingly. But the local minima are metastable due to the applied field dependence. If one local minimum becomes unstable and vanishes, the magnetization changes direction immediately, such that the system is at minimal energy again. Which of the local minima is assumed first, depends on the initial value of the applied field. Therefore the valid solution is determined by the applied field history of the sample [16].

Once the metastable energy minimum becomes unstable, the rotation of the magnetization is irreversible. In the cases where there is only one energy minimum present at a time, there is no hysteresis, and thus the rotation of the magnetization can be stopped anytime during the sweep and be reversed for instance [15].

### 2.5.5. Discussion

We may pay special attention to the differences between the three basic configurations in figure 2.6. The following description is meant to clarify and map the energy landscape for the three configurations within the  $y'$ - $z'$ -, and the  $x'$ - $y'$ -plane of the coordinate system. The magnetization is *chosen* to be constraint to these planes, such that we can follow the magnetization state progression with increasing applied field by following the angle of the local energy minimum.

*Configuration* 1: Looking at the  $y'$ - $z'$ -plane, with increasing applied field the magnetization stays in the initial direction  $\Theta' = \pi$ , supported by the anisotropy term in the magnetostatic

---

<sup>b</sup>Neglecting the infinite number of solutions due to the  $\pi$ -periodic symmetry of the physical system.

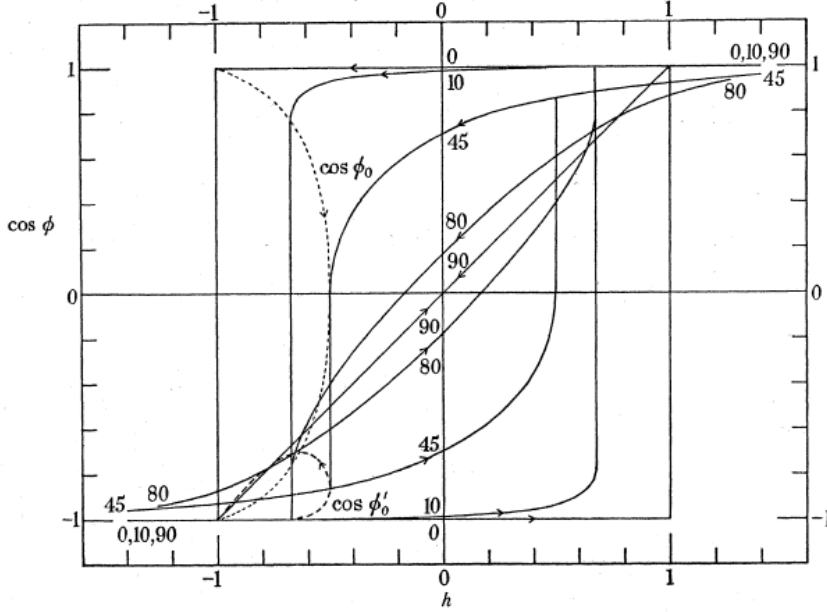


FIGURE 6. Magnetization curves for prolate spheroids. The resolved magnetization in the positive field direction is given by  $I_0 \cos \phi$ , where  $I_0$  is the saturation magnetization. The field,  $H$ , is given by  $H = (N_b - N_a) I_0 h$ , where  $N_a$  and  $N_b$  are the demagnetization coefficients along the polar and equatorial axes. The angle,  $\theta$ , between the polar axis and the direction of the field, is shown, in degrees, by the numbers on the curves. The dotted curves give  $\cos \phi_0$  and  $\cos \phi'_0$ , where  $\phi_0$  and  $\phi'_0$  are the angles made with the positive field direction by the magnetization vector at the beginning and end of the discontinuous change at the critical value,  $h_0$ , of the field.

Figure 2.7. | Graph of the limiting hysteresis curve of a prolate ellipsoid in configurations [1] and [2], and transient configurations. Original figure 6 from Stoner and Wohlfarth [20] (1948). Symbol transcription: saturation magnetization  $4\pi I_0 \mapsto M_s$ , the angle between applied field and magnetization  $\phi \mapsto \theta - \Theta'$ , reduced field  $h \equiv \frac{H}{(D_b - D_a)M_s}$ , demagnetization factors  $N_i \mapsto 4\pi D_i$ , the angle between the ellipsoid polar axis and the applied field is implicitly defined by the configuration, and the critical reduced field is the reduced coercivity.

energy. At negative coercivity the local energy minimum becomes metastable and is further destabilized for increasing applied field, but the minimum is still present at a constant angle. Only when the positive coercivity is reached, the first minimum vanishes, and the magnetization immediately jumps to the second emerged minimum in direction  $\Theta' = 0$ , thus following the applied field. So in between the coercivities there are two solutions to the minimization problem, for higher magnitudes of the applied field, there is only one. This behavior results in a rectangular hysteresis curve as shown in the original figure 6 of Stoner and Wohlfarth [20] (1948), reproduced in figure 2.7, labeled  $0^\circ$ .

Considering the  $x'-y'$ -plane we can see, that there is neither a preferred direction of the magnetization, nor any applied field dependence. This follows from the circular cross-section of the prolate ellipsoid perpendicular to its axis of revolution, and from the absence of an applied field component in the  $x'-y'$ -plane.

*Configuration [2]:* In the  $y'-z'$ -plane the magnetization starts out at  $\Theta' = \pi$  at negative applied field. The easy axis here however is the  $\hat{y}'$  direction. From negative coercivity, the minimum starts to shift towards the easy axis at  $\Theta' = \frac{\pi}{2}$ . For zero applied field, only the

shape anisotropy determines the magnetization direction. For positive fields the minimum continues to follow towards the applied field direction, and with positive coercivity a stable state directed to  $\Theta' = 0$  is reached. At all times there is only one solution to the minimization problem present (excluding equivalent solutions due to symmetry). The described behavior is reflected in the non-hysteretic, diagonal magnetization curve shown in figure 2.7, labeled  $90^\circ$ .

In the  $x'$ - $y'$ -plane, again, there is no applied field dependence, since the applied field does not exhibit contribution to that plane. In contrast to configuration [\[1\]](#), a preferred angle of the magnetization in  $\hat{y}'$  direction is apparent. These minima are a consequence of the shape anisotropy energy.

*Configuration [\[3\]](#):* In the  $y'$ - $z'$ -plane the magnetization stays with the applied field. Once reaching zero applied field, there are neither constraints due to the applied field, nor due to the shape (which is circular within the  $y'$ - $z'$ -plane). The magnetization in principle is free to assume any direction. If we consider a continuous applied field sweep, the magnetization direction jumps from  $\Theta' = \pi$  to  $\Theta' = 0$  at zero field, such that here the coercivity is  $H_c = 0$ , which follows from equation (2.15) for  $(D_\perp - D_\parallel) = 0$ . Therefore always only one solution is present. The magnetization behavior results in a rectangular magnetization curve similar to the one encountered in configuration [\[1\]](#), but with zero width.

The magnetization behavior of configuration [\[3\]](#) in the  $x'$ - $y'$ -plane (lower row of figure 2.6) resembles the description of configuration [\[2\]](#), except for a shift in  $\Phi'$ : Here, the easy axis of the prolate ellipsoid is aligned to the  $\hat{x}'$ -direction.

Despite the described differences between configurations [\[2\]](#) and [\[3\]](#), the constraint of the magnetization to the  $y'$ - $z'$ -plane in configuration [\[3\]](#) is hypothetical and chosen here only to illustrate the energy landscape. The actual rotation of the magnetization within a prolate ellipsoid is determined by its shape and the direction of the applied field only, such that the behavior of the magnetization within the ellipsoid for configurations [\[2\]](#) and [\[3\]](#) is actually equivalent.

Hysteresis curves in figure 2.7 labeled  $0^\circ$  to  $90^\circ$  refer to angles  $\theta$  between applied field and polar ellipsoid axis. In a general solution to the energy minimization problem, all these configurations are covered, and corresponding optimal angles of the magnetization within the magnetic particle can be found. The configurations  $0^\circ$  and  $90^\circ$  are covered by our configurations [\[1\]](#) and [\[2\]](#), respectively, see figure 2.6. The configurations  $0^\circ < \theta < 90^\circ$  constitute a transition of the shape of the hysteresis curve from rectangular to diagonal, i.e. a transition between our configurations [\[1\]](#) and [\[2\]](#). For these configurations the coercivity is reduced (dotted line in figure 2.7), because the energy minima of figure 2.6 are shifted both in magnetization angular position and magnitude as a function of the angle  $(\theta - \Theta')$ . Additionally, for  $0^\circ < \theta < 90^\circ$ , the magnetization only aligns to the applied field asymptotically: Phenomenologically speaking, if the magnetization were aligned to the applied field, the torque rotating the magnetization due to the Zeeman interaction would be zero. The opposing torque arising from the shape anisotropy, in contrast, is finite, so alignment would only be possible for an infinite applied field [15].

## 2.6. Magnetization States and Reversal Of Non-Ideal Samples

### 2.6.1. Limits of Stoner-Wohlfarth Model

A nanometer-scale magnetic sample in the shape of a prolate ellipsoid is exactly described in its magnetization behavior by the Stoner-Wohlfarth model. Although coherent rotation is not common in real magnetic samples, the model system reproduces many of the features of experimentally acquired hysteresis data, even for larger samples.

Especially in larger magnetic particles, on a macroscopic level, inhomogeneous perturbations in the alignment of the magnetic dipoles are present, such that the magnetization  $\mathbf{M}(\mathbf{r})$  is no longer constant. Hence the magnetization reversal starts by nonuniform nucleation and becomes generally incoherent. This effect in principle is measurable in a rise of the coercivity, but that rise is strongly counteracted by the inhomogeneous structure of most real magnetic particles, such that experimental coercivities usually are smaller than theoretically calculated by a factor two to ten [14].

Incoherent nucleation in prolate ellipsoids, as well as in circular cylinders, may take the form of the *curling mode*, in which the magnetization has a circumferential component that is a function of the radial distance to the polar axis. During reversal this curling mode passes through a state of flux closure, also known as *vortex state*, for minimal magnetostatic energy [15].

### 2.6.2. Nano-Scale Magnetic Samples

In nanometer-scale magnetic samples, the low-dimensionality of these structures results in magnetic configurations not present in macroscopic magnets. Due to the topology of the samples described in section 4.3, we are interested in the magnetization reversal of cylindrical and tubular structures (nanotubes). These structures avoid magnetization point singularities as present in solid magnetic cylinders [28], but support core-free magnetization states, a prerequisite for fast magnetization reversal [29]. Apart from uniform axial magnetization, with the magnetic moments pointing along the nanotube axis, at the ends of such nanotubes curling-mode-like states have been simulated [30] (“twisted bamboo”). Magnetic dipoles in the middle sections are free to rotate independently [31] (“zig-zag shaped”), and form vortex [29] and transverse domain walls [32]. Circumferential magnetization vortices (around the perimeter of the nanotube) are reported in [33] together with in-plane non-circumferential magnetization vortices (only on one side or within one facet of the nanotube) [34].

Magnetization reversal may take the form of propagating vortex or transverse domain walls [29, 32, 35–37], or a mixed multi-domain combination of the former [29, 38, 39]: Magnetic moments rotate progressively via propagation of a domain wall, within which magnetic moments are aligned circumferential or perpendicular with respect to the nanotube symmetry axis. Micromagnetic simulations may help to better understand the interplay of mixed states. In [40, 41] an “onion state” is suggested, consisting of two oppositely oriented circumferential

domains, and confining states in which all magnetic moments align along the applied field or the easy anisotropy axis.

Recent results hint on how nucleation of magnetization reversal takes place: Nucleation sites over the full length of the nanotube give rise to simultaneous reversal in several domains. Micromagnetic simulations reveal possible nucleation sites including inhomogeneities in the nanotube structure, like surface roughness, or inherent edges of faceted nanotubes [42].



# 3. Cantilever Magnetometry

## 3.1. Introduction

Several experimental methods allow for the measurement of the magnetization and magnetic anisotropy of small magnetic particles. Before we focus on torque based means of magnetometry, a few other important techniques are briefly introduced in section 3.2 to broaden the spectrum of available tools, rather than to give a complete list.

For the experiments presented in this thesis, we use dynamic cantilever magnetometry. In section 3.3 the basic constituents of the technique are explained. The essential component, a mechanical oscillator, is treated mathematically in detail to predict the data we later obtain during the measurements. The response of the mechanical oscillator to an applied magnetic field is a shift in the mechanical resonant frequency. We discuss the according behavior in section 3.4.

To later quantify the expected frequency shift, one needs to know the micromagnetic demagnetization factors, scaling the magnetostatic self-energy of the magnetic sample. The formulae are prepared in section 3.5.

## 3.2. Methods Overview

### 3.2.1. Atomic Scale

The origin of magnetism lies in the atomic-scale structure of the magnetic material. To probe both the crystalline and the magnetic structure, diffraction methods are widely spread. They rely on a beam of radiation scattered by the electrons or nuclei of the sample material, so the beam wavelengths should be comparable to the inter-atomic spacing. Interference of the scattered waves leads to diffraction beams, following Bragg's law [43], dependent on the lattice parameters. The desired interaction determines the diffraction method. Neutron diffraction is sensitive to the magnetic moments of electrons. Magnetic samples typically are prepared as a powder [14].

By measuring the energy of inelastically scattered beams one can investigate the energy levels of magnetic samples. Absorption spectroscopy and photoelectron spectroscopy can probe the structure of surface layer electrons. High spatial resolution can be achieved, when intense

polarized light sources, possibly of x-ray energies, and polarization sensitive readout of the emitted photons are available. X-ray magnetic circular dichroism photoelectron emission microscopy (XMCD-PEEM) is mentioned here [34, 44]. Magnetic circular dichroism refers to the difference in absorption for left- and right-circular polarized light passing through a magnetic sample [14].

### 3.2.2. Bulk Magnetization

Measurements of magnetic fields are categorized by either measuring the force on the magnetic sample, or the change of magnetic flux in a circuit. Measurements of the magnetization and stray fields close to the sample surface may be used to visualize their spatial distribution [14].

Force measurement methods rely on the force on a magnetic moment resulting from a gradient magnetic field, recorded by a balance. The sensitivity of this method can be enhanced by converting the continuous signal of the balance to an alternating one, realized with an alternating gradient magnetic field at the mechanical resonant frequency of the balance rod [14]. A specialized technique for measuring the total anisotropy, including magneto-crystalline and shape anisotropy, involves the recording of a torque curve. A field is applied in different directions with respect to the anisotropy axes of the magnetic sample, and a torsion balance is used to measure the resulting mechanical torque. Some difficulty involves the generation of the applied field in an air gap to be large enough to saturate the magnetic sample and guarantee a single-domain character [16]. Also nuclear magnetic resonance (NMR) can be used to probe magnetic fields knowing the nuclear resonance frequency of the sample isotopes. The signal is recorded from the response of a mechanical oscillator, called cantilever, with the magnetic sample affixed to its one end [9].

Methods based on the change of magnetic flux usually involve some sort of inductive pick-up coil, or the utilization of the Hall effect [45]. Flux changes occur during movement of the sample, as in vibrating-sample magnetometry (VSM), or within a superconducting quantum interference device (SQUID). Where for the former a typical application is the fast recording of limiting hysteresis loops, for the latter, due to its high sensitivity, also small changes during magnetization reversal can be probed. SQUID magnetometry is suitable for small samples such as thin magnetic films or magnetic particles comparable to the size of the critical single-domain radius (section 2.4.3) [14]. Recent experiments include magnetic characterization of ordered arrays of nanometer-sized tubular magnetic samples (nanotubes) [37, 39, 46, 47], the study of magnetization reversal [38, 48], and magnetic anisotropy [49]. Nanometer-sized scanning SQUIDs (nanoSQUIDs) have been used to map the stray field of individual nanotubes while simultaneously probing their volume magnetization [50].

Visualizing the spatial distribution of magnetization and studies of magnetization reversal usually depend on the near-surface stray field of the magnetic sample. Not always the surface domains and domain walls are actually representative for the bulk material. Magnetic force microscopy (MFM) is a scanning probe technique utilizing a mechanical oscillator (cantilever) sensitive to the gradients of the stray field. Similar to atomic force microscopy (AFM), the deflection and the changes in the resonant frequency of the cantilever are registered, with a

variety of ferromagnetic, inductive, or magneto-resistive pick-up tips. MFM has been used to study metastable magnetization states [41] and flux closure states [51] in magnetic nanorings, to observe magnetization switching in magnetic nanotubes [52], and to probe the anisotropy in nanometer-sized magnetic particles (nanomagnets) [53]. Another emerging high resolution scanning probe technique involves the utilization of nitrogen vacancy centers (NVs) in diamond to map magnetic dipole fields in the sub-nanometer range [54]. Furthermore, scanning or transmission electron microscopy (SEM/TEM) can be used to raster a sample surface and image both microstructure, topology, chemical composition, and magnetic contrast. The relevant interaction here depends on the Lorentz force [14, 55]. Electron holography, as an extension to TEM, additionally allows the recording of the electron wave phase shift, carrying information on in-plane component of the magnetic field [56].

The mapping of magnetic domains is also possible using optical techniques: A beam of radiation is influenced by the ferromagnetic order in the sample material. For light, the magneto-optical Kerr effect (MOKE) is mentioned [57, 58]. It is based on the Faraday effect, where the polarization of light is rotated under passage through magnetic media, by an amount proportional to the path length in the medium. Since the MOKE refers to reflection, it can be combined to polarization sensitive optical microscopy, giving simultaneous images of microstructure and domain structure [14].

Many of the aforementioned methods of magnetometry may provide the means to probe nanomagnets [37–39, 46–49]. Measurements have been carried out on large ensembles of magnetic particles, actually recording an average of the individual contributions. Due to interaction effects between individual particles, and the distribution in sample size, shape and orientation, these measurements are difficult to interpret [15, 22, 40]. In 2012, Rüffer et al. [40] probed the magnetic states of a single nanotube, using the anisotropic magneto-resistance effect: Depending on the orientation of an applied field with respect to the easy and hard axis of the magnetic sample, the resistivity of the electrically contacted sample is subject to changes. In the case of atomic-layer-deposited (ALD) Ni nanotubes, the resistivity as a measure for the magnetization states was reported to only depend on the magnetic shape anisotropy. In our approach, we focus on the measurement of individual nanotubes using torque magnetometry.

### 3.2.3. Cantilever Torque Magnetometry

Cantilever torque magnetometry is a sensitive tool to detect the weak magnetic response of a variety of nanometer-scale systems. Recent experiments include the measurement of magnetic fluctuations in nanometer-sized ferromagnetic particles [21], persistent currents in normal metal rings [59], and of the magnetization of superconducting nanostructures [60]. Cantilever magnetometry has also been used to detect the magnetization reversal in single Fe-filled carbon nanotubes [61] and a single Ni nanorod [62], and to observe mesoscopic vortex physics in superconductors [63].

We will follow Jang et al. [64] to categorize different approaches of cantilever torque magnetometry: Cantilever torque magnetometry is based on the effect of a magnetized particle on a mechanical oscillator (cantilever) in an applied field. The torque produced by the mag-

netic moments of the sample mounted on the end of the cantilever modifies the response of the cantilever. Commonly three different approaches (modes) make use of cantilever torque magnetometry: In mode 1, the constant deflection of the cantilever is measured in a static or low frequency applied field, called static cantilever magnetometry (SCM). For mode 2 one measures the cantilever resonant frequency in a static field, i.e. dynamic cantilever magnetometry (DCM), and mode 3 involves the measurement of the resonant cantilever displacement by applying a secondary magnetic field at the cantilever resonant frequency. The latter mode is called phase-locked cantilever magnetometry (PLCM). Where for mode 1 a constant deflection is recorded typically in form of a direct current signal, the displacement sensitivity is enhanced for modes 2 and 3 by the quality factor  $Q$  of the cantilever by measuring a frequency. In both mode 2 and 3 the sensitivity benefits from high applied fields, additionally PLCM utilizes a cantilever deflection-dependent field, which further boosts sensitivity by a factor of the inverse peak deflection angle. In DCM additional benefit comes from the ability to track changes in the magnetization in timescales in the order of a few cantilever oscillation cycles [64]. For our measurements of the magnetic anisotropy and magnetization reversal of individual nanotubes we use DCM (mode 2).

### 3.3. Dynamic Cantilever Magnetometry (DCM)

#### 3.3.1. Introduction

To investigate the weak magnetic response of individual magnetic nanotubes without averaging over an inhomogeneous ensemble, we use highly sensitive DCM (mode 2). This technique allows us to study the magnetization states, demagnetization factors and magnetization reversal mechanisms of single nanotubes as a function of the applied field and the alignment of the sample. A nanotube is affixed to the end of an ultrasoft cantilever, which is a mechanical oscillator capable of deflection in one direction only and torsion for higher oscillation modes. The torque acting between the magnetic particle and the applied field shifts the resonant frequency of the cantilever. We measure the resonant frequency as a function of the applied field by fiber optical laser interferometry<sup>a</sup> [21, 22, 65].

Compared to other means of cantilever torque magnetometry, with DCM we can achieve a high precision by counting a frequency, rather than recording a direct current signal. At the same time interfering electrostatic and magnetostatic fields are entirely avoided by a purely optical readout. DCM is sensitive to the volume magnetization of the sample, instead of probing the total magnetic field including the stray field for instance. Changes in the magnetization state can be tracked in timescales in the order of a few cantilever oscillation cycles.

---

<sup>a</sup>Methods see section 4.6.

### 3.3.2. Cantilever

The mechanical oscillators used in DCM exhibit beam-like shape, clamped at one end, free at the other, in the so called cantilever configuration. These cantilevers typically share common geometrical and mechanical properties, such as cross-sections very small compared to their length, resulting in a low spring constant  $k$  and a high quality factor  $Q$ . The implication of  $Q$  as a measure of the rate of energy loss is the description of a cantilever as a damped oscillator. The lower the dissipation  $\Gamma$ , the higher the dimensionless value of  $Q$ . For high  $Q$ s, the motion of the cantilever in each oscillation mode can be described by a damped harmonic oscillator, where the elastic potential energy of the cantilever material is the dominant origin of the restoring force of the oscillator. [66, 67].

A damped harmonic oscillator in the realization of a mathematical pendulum implies the assumption of a massless cord and a point mass at its end containing the total mass of the harmonic oscillator. If we like to describe the oscillation of a cantilever correctly by the equation of motion of a damped harmonic oscillator, we need to introduce the concept of an effective length and mass.

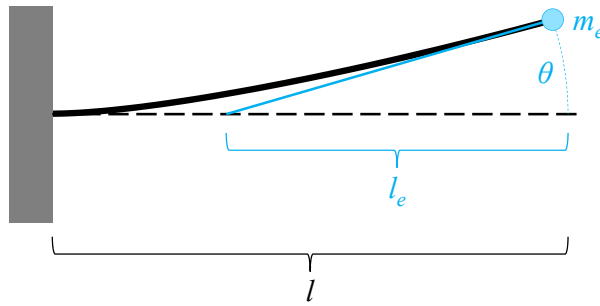


Figure 3.1. | Illustration of a mechanical oscillator in cantilever configuration. Definition of the effective length  $l_e$  compared to cantilever length  $l$ . Illustration not to scale.

The effective length  $l_e$  compensates for the non-linear mode shape of a deflected cantilever and is defined in figure 3.1 as the length of a straight line with matching displacement and angle at the cantilever's tip position. The cantilever is operated under small deflections  $\theta < 0.0005 \ll 1$  in its fundamental oscillation mode. The aspect ratio of the cantilever cross-section of below 0.03 ensures one-dimensional deflection in the cantilever fundamental oscillation mode and torsion only in higher modes. The fundamental mode shape and effective length of such a cantilever is calculated numerically for figure 4.2.

The effective mass  $m_e$  is the motional mass of the cantilever. Each mass element in the volume of the cantilever individually responds to deflection depending on its position. The effective mass is a volume average of all mass elements, replacing the total mass of the cantilever, such that the elastic potential energy is constant. The effective mass for a cantilever with uniform cross-section is  $1/4$  of the total mass [8, 67].

### 3.3.3. Damped Harmonic Oscillator

The elastic potential energy stored in the cantilevers used in DCM for small deflection angles  $\theta \ll 1$  is

$$E_{osc} = \frac{k_0}{2} (l_e \theta)^2 \quad (3.1)$$

The index “0” indicates physical quantities of the fundamental oscillation mode. From here the restoring torque enters the equation of motion of a damped harmonic oscillator:

$$m_e l_e^2 \cdot \ddot{\theta} + \Gamma_0 l_e^2 \cdot \dot{\theta} - k_0 l_e^2 \cdot \theta = 0$$

We find the spring constant, the effective mass and the dissipation by

$$k_0 = \frac{k_B T}{\langle y^2 \rangle}, \quad m_e \equiv \frac{k_0}{\omega_0^2}, \quad \text{and} \quad \Gamma_0 \equiv \frac{m_e \omega_0}{Q_0} \quad (3.2)$$

from experimentally accessible quantities<sup>a</sup>, including the temperature  $T$ , the mean square cantilever tip deflection  $\langle y^2 \rangle = l_e^2 \langle \theta^2 \rangle$ , the fundamental resonant angular frequency of a simple (i.e. undamped) harmonic oscillator  $\omega_0$ , and the quality factor  $Q$ .  $k_B = 1.3806 \cdot 10^{-23}$  J/K is the Boltzmann constant. From the solution of the equation of motion we find the cantilever oscillation angular frequency  $\omega = \sqrt{\frac{k_0}{m_e} - \left(\frac{\Gamma_0}{2m_e}\right)^2}$ . Thus, relative to  $\omega_0$  the oscillation frequency is shifted by:

$$\Delta\omega \equiv \omega - \omega_0 = \omega_0 \cdot \left( \sqrt{1 - \left(\frac{1}{2Q_0}\right)^2} - 1 \right) \quad (3.3)$$

Our cantilevers show quality factors of  $Q_0 > 30\,000$ , such that  $\left(\frac{1}{2Q_0}\right)^2 < 3 \cdot 10^{-10} \ll 1$ .

## 3.4. Derivation of Resonant Frequency Shift

### 3.4.1. Introduction

We derive an expression for the shift of the resonant frequency of a cantilever with a nanomagnet affixed to its end, as a function of the applied magnetic field. The expression is given in terms of the saturation magnetization and the demagnetization factors of the magnetic sample.

Applied field  $\mathbf{H}$  and magnetization  $\mathbf{M}$  result in a torque  $\boldsymbol{\tau}(\theta)$  acting on the cantilever, adding to the mechanical restoring force, effectively stiffening or softening the cantilever, thus shifting its resonant frequency. By minimizing the total energy of the system we get the preferred angles  $\Theta'(\theta)$  and  $\Phi'(\theta)$  of the sample magnetization for each deflection angle  $\theta$  of the cantilever [16, 20–22, 68–71].

As a magnetic sample we consider an ellipsoidal nanomagnet according to the Stoner-Wohlfarth model ([20] and section 2.5), exhibiting only shape anisotropy (section 2.4.2). For the derivation

the coordinates of figure 3.2 are used, in accordance with the previously introduced coordinates of figure 2.4.

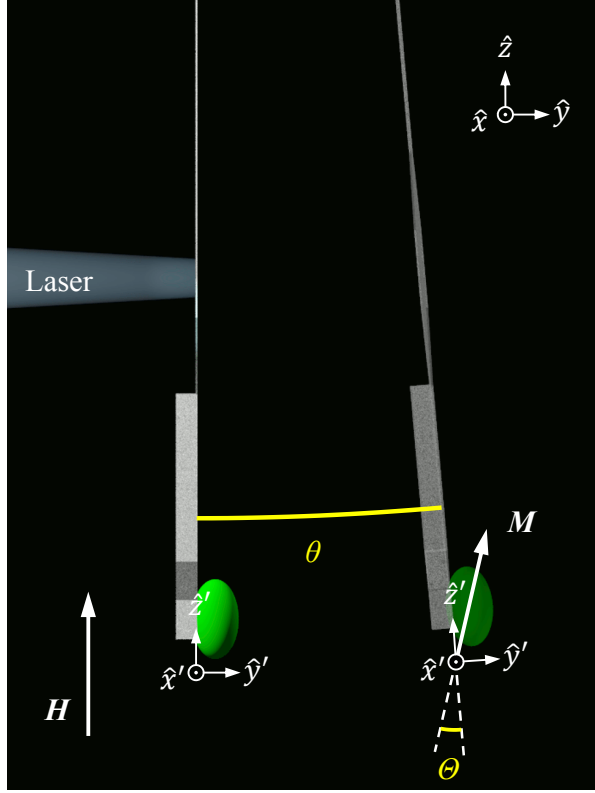


Figure 3.2. | Schematic diagram of the coordinate systems and angles used in dynamic cantilever magnetometry. In particular,  $\theta$  is the angle between the cantilever tip (fixed along the  $\hat{z}'$  axis) and the applied field  $\mathbf{H}$  (fixed along the  $\hat{z}$  axis), i.e. the deflection angle of the cantilever tip.  $\Theta'$  is the angle between the cantilever tip and the magnetization vector  $\mathbf{M}$  in projection onto the  $y'$ - $z'$ -plane. Diagram is to scale, deflection exaggerated for clarity.

Since now the magnetic sample is affixed to the cantilever, the primed coordinates also become the coordinates following the cantilever tip motion. In particular,  $\theta$  is the angle between the cantilever tip (fixed along the  $z'$  axis) and the applied field (fixed along the  $z$  axis), i.e. the deflection angle of the cantilever tip.

From equations (3.1), (2.10) and (2.13), the total energy  $E_{tot}$  of a single-domain ellipsoidal nanomagnet affixed to the end of a cantilever can be written as the sum of the elastic potential energy  $E_{osc}$ , the Zeeman energy  $E_Z$ , and the magnetostatic self-energy  $E_{ms}$ :

$$\begin{aligned}
 E_{tot} = & \frac{k_0}{2} (l_c \theta)^2 \\
 & - \mu_0 V M_s H (\sin \theta \sin \Theta'(\theta) \cos \Phi'(\theta) + \cos \theta \cos \Theta'(\theta)) \\
 & + \frac{\mu_0}{2} V M_s^2 ((D_x \sin^2 \Phi'(\theta) + D_y \cos^2 \Phi'(\theta)) \sin^2 \Theta'(\theta) + D_z \cos^2 \Theta'(\theta)) \quad (3.4)
 \end{aligned}$$

### 3.4.2. Torque on the Cantilever

In DCM, the torque  $\tau$  resulting from the magnetic particle in the applied field enters the equation of motion of the damped harmonic oscillator in its fundamental oscillation mode as a modified restoring torque:

$$m_e l_e^2 \cdot \ddot{\theta} + \Gamma_0 l_e^2 \cdot \dot{\theta} - \tau(\theta) = 0 \quad (3.5)$$

The partial derivative of the total energy of the system with respect to the angle of motion  $\theta$  of the cantilever leads to the torque  $\tau$  acting on the cantilever [27], namely

$$\tau = - \frac{\partial E_{tot}}{\partial \theta} \quad (3.6)$$

By expressing the torque  $\tau$  as a function of the deflection angle  $\theta \ll 1$  we can write

$$\tau(\theta) \approx \tau(0) + \left. \frac{\partial \tau}{\partial \theta} \right|_{\theta=0} \cdot \theta$$

and with equation (3.6) we arrive at

$$\tau(\theta) = - \left. \frac{\partial E_{tot}}{\partial \theta} \right|_{\theta=0} - \left. \frac{\partial}{\partial \theta} \left( \frac{\partial E_{tot}}{\partial \theta} \right) \right|_{\theta=0} \cdot \theta \quad (3.7)$$

We can now rewrite the damped harmonic oscillator equation of motion (3.5) with the help of equation (3.7):

$$m_e l_e^2 \cdot \ddot{\theta} + \Gamma_0 l_e^2 \cdot \dot{\theta} + \left( \frac{1}{l_e^2} \left. \frac{\partial^2 E_{tot}}{\partial \theta^2} \right|_{\theta=0} \right) l_e^2 \cdot \theta = - \left. \frac{\partial E_{tot}}{\partial \theta} \right|_{\theta=0}$$

The term in parentheses is identified as an effective spring constant  $k_e \equiv k_0 + \Delta k(\theta)$  of the sample-on-cantilever system, with  $\Delta k(\theta)$  effectively stiffening or softening the cantilever compared to a damped harmonic oscillator  $k_0$ . The right hand side of the equation represents a constant deflection of the oscillator, as utilized in SCM (mode 1).

Using the effective spring constant, we now can solve the equation of motion. We find the cantilever oscillation angular frequency to be  $\omega = \sqrt{\frac{k_0}{m_e} + \frac{\Delta k(\theta)}{m_e} - \left(\frac{\Gamma_0}{2m_e}\right)^2}$ . Similar to (3.3) and for high quality factors  $\left(\frac{\Gamma_0}{2m_e}\right)^2 \rightarrow 0$ , we can rewrite the cantilever oscillation angular frequency shift  $\Delta\omega = \omega - \omega_0$  as

$$\Delta\omega = \omega_0 \cdot \left( \sqrt{1 + \frac{\Delta k(\theta)}{k_0}} - 1 \right) \approx \frac{\omega_0}{2k_0} \cdot \Delta k(\theta) \quad (3.8)$$

using the approximation  $\sqrt{1 + \epsilon} \approx \frac{\epsilon}{2} + 1$  for  $\epsilon \ll 1$ . From the known energies (3.4) we can deduct

$$\begin{aligned} \frac{1}{l_e^2} \left. \frac{\partial^2 E_{tot}}{\partial \theta^2} \right|_{\theta=0} &= \frac{1}{l_e^2} \left. \frac{\partial^2 E_{osc}}{\partial \theta^2} \right|_{\theta=0} + \frac{1}{l_e^2} \left. \frac{\partial^2 (E_Z + E_{ms})}{\partial \theta^2} \right|_{\theta=0} \\ k_e &= k_0 + \Delta k(\theta) \end{aligned}$$



so we can rewrite (3.8) to

$$\Delta\omega = \frac{\omega_0}{2k_0 l_e^2} \cdot \frac{\partial^2(E_Z + E_{ms})}{\partial\theta^2} \Big|_{\theta=0} \quad (3.9)$$

thus stating, that the curvature of the energy determines the frequency shift. The sum  $E_Z + E_{ms}$  is the total magnetostatic energy of the sample-on-cantilever system. Other energy terms of (2.9) are ignored, specifically, since the exchange energy is a constant and the sample material is assumed to be homogeneous, non-crystalline, and unstrained. The energy is given in terms of the angles  $\Theta'(\theta)$  and  $\Phi'(\theta)$  which can be expanded as a function of  $\theta$  to first order around  $\theta = 0$  for  $\theta \ll 1$ :

$$\Theta'(\theta) \approx \Theta'_0 + \frac{\partial\Theta'}{\partial\theta} \Big|_{\theta=0} \cdot \theta \quad (3.10a)$$

$$\Phi'(\theta) \approx \Phi'_0 + \frac{\partial\Phi'}{\partial\theta} \Big|_{\theta=0} \cdot \theta \quad (3.10b)$$

The second derivative of the energy with respect to  $\theta$  for (3.9) then is an extensive expression, for which the reader may refer to appendix A.1. The expression will be given later in the context of some special case, see equation (3.18).

### 3.4.3. Minimization of Total Energy

To find the actual frequency shift, we need to know the angles  $\Theta'(\theta)$  and  $\Phi'(\theta)$  of the magnetization within the magnetic particle. In ferromagnetic nanotubes, microscopic magnetic processes occur at a much higher frequency than the cantilever resonant frequency [32, 72, 73], such that the magnetization is always assumed in equilibrium at an optimal angle between the applied field and the easy axis of the particle. That angle is determined by minimization of the total energy (3.4) of the system, i.e. one needs to find the stationary points for which  $\frac{\partial E_{tot}}{\partial\Theta'} = \frac{\partial E_{tot}}{\partial\Phi'} = 0$ .

In figure 3.3 the three basic configurations of an ellipsoidal nanomagnet are shown and the corresponding total reduced energy  $e_{tot} \equiv \frac{2E_{tot}}{\mu_0 V M_s^2}$  is plotted as a function of both the polar coordinate  $\Theta'(\theta)$  and the azimuthal coordinate  $\Phi'(\theta)$  of the magnetization (2.8), similar to figure 2.6, but including the cantilever elastic potential energy  $e_{osc}$ . The cantilever deflection  $\theta$  is chosen small and positive but unequal zero, the applied field  $\mathbf{H}$  is set above positive coercivity. Low energy is in blue, high energy in red, local energy minima are indicated by dotted rectangles, angular changes due to applied field sweeps indicated by arrows.

In configuration 1 the minimal energy is found around  $\Theta' = 0$  for arbitrary  $\Phi'$ . The asymmetry of the energy landscape in  $\Phi'$  is caused by the deflection angle of the cantilever. During oscillation the minimum will always stay between the applied field direction and the easy axis of the sample. Sweeping the applied field will result in the appearance of a secondary energy minimum around  $\Theta' = \pi$ , causing the first minimum to become metastable. Only when the first minimum disappears, the magnetization will instantly assume  $\Theta' = \pi$ , thus jumping by  $180^\circ$ .

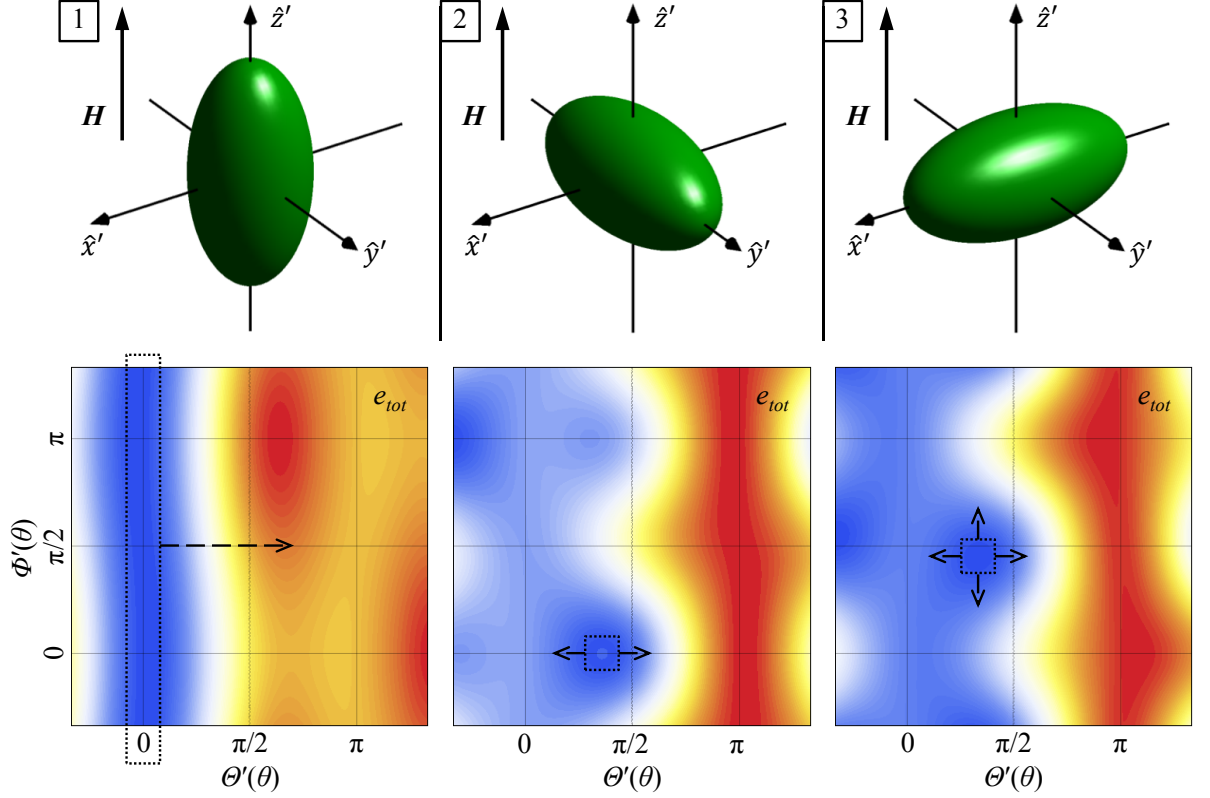


Figure 3.3. | Illustration and graphs of the total magnetostatic energy of ellipsoidal nanomagnets. Three basic configurations are shown and the corresponding total reduced energy  $e_{tot}$  is plotted as a function of the polar angle  $\Theta'(\theta)$  and the azimuthal angle  $\Phi'(\theta)$ . The cantilever deflection  $\theta$  is chosen small but unequal zero, the applied field  $\mathbf{H}$  is set above coercivity. Low energy is in blue, high energy in red, local energy minima indicated by dotted rectangles, angular changes due to applied field sweeps indicated by arrows.

In configuration [2] the minimal energy is found for  $\Phi' = 0$  (and  $\Phi' = \pi$ , due to symmetry). Sweeping the applied field will result in the energy minimum moving along constant  $\Phi'$  between values of  $\Theta' = 0$  and  $\pi$ . The oscillation angle  $\theta$  influences the depth of the minimum but not its position.

In configuration [3] the minimal energy is found around  $\Phi' = \frac{\pi}{2}$ . Sweeping the applied field will result in the energy minimum moving both around values of  $\Phi' = \frac{\pi}{2}$ , and between values of  $\Theta' = 0$  and  $\pi$ . The deflection angle  $\theta$  influences the depth of the minimum and its position in  $\Phi'$  during cantilever oscillation, note the asymmetric position of the energy minimum around  $\Phi' = \frac{\pi}{2}$ . Therefore a general analytical solution to the minimization problem is demanding. In case of a small deflection angle  $\theta \ll 1$  the magnetization behavior of configuration [3] resembles the description of configuration [2], except for a shift in  $\Phi'$ .

For a more elaborate explanation of the underlying physics in terms of magnetism, refer to section 2.5.5, here we sum up, that a general solution of the energy minimization problem is possible, but tedious due to the mentioned dependencies on the cantilever oscillation angle  $\theta$ , and includes finding the root of a quartic equation [74].

Special cases including certain assumptions of exact angles can be solved here to illuminate the general behavior. For configuration [1], we can find the minimum for arbitrary  $\Phi'$  and for configuration [2], the minimum is in  $\Phi' = 0$ , since we can assume the magnetization to stay in a plane spanned by the applied field direction and the easy anisotropy axis. For configuration [3] no constant angles can be assumed. In principle one can find a general solution using the same procedure as shown here, we will focus on the analytical solution for configurations [1] and [2].

We will investigate the minima of the total energy and thus derive the optimal angle for the magnetization with following set of equations for configurations [1] and [2] under the assumption of  $\Phi' = 0$ :

$$E_{tot} = \frac{k_0}{2}(l_e\theta)^2 - \mu_0VM_sH \cos(\theta - \Theta') + \frac{\mu_0}{2}VM_s^2(D_\perp \sin^2 \Theta' + D_\parallel \cos^2 \Theta') \quad (3.11a)$$

$$\left. \frac{\partial E_{tot}}{\partial \Theta'} \right|_{\Phi'=0} = 0 \quad \text{and} \quad \left. \frac{\partial^2 E_{tot}}{\partial \Theta'^2} \right|_{\Phi'=0} > 0 \quad (3.11b)$$

Listed is the total energy of the sample-on-cantilever system, and the necessary and sufficient condition for an energy minimum. Here, the conventions  $D_y \equiv D_\perp$  and  $D_z \equiv D_\parallel$  are used.

We start by solving the two conditions (3.11b):

$$H \sin(\theta - \Theta') = M_s(D_\perp - D_\parallel) \sin \Theta' \cos \Theta' \quad (3.12a)$$

$$-H \cos(\theta - \Theta') < M_s(D_\perp - D_\parallel) \cos 2\Theta' \quad (3.12b)$$

To solve equation (3.12a) for arbitrary  $\Theta'$ , we only consider small deflections  $\theta \ll 1$ , such that (3.12a) becomes<sup>b</sup>:

$$\theta = \frac{M_s}{H}(D_\perp - D_\parallel) \sin \Theta' + \tan \Theta' \quad (3.13)$$

Solution is possible, if we use the expansion (3.10a) and rewrite it to:

$$\Theta'(\theta) = \Theta'_0 + \left( \left. \frac{\partial \theta}{\partial \Theta'} \right|_{\Theta'=\Theta'_0} \right)^{-1} \cdot \theta \quad (3.14)$$

The derivative  $\frac{\partial \theta}{\partial \Theta'}$  may be taken from (3.13):

$$\frac{\partial \theta}{\partial \Theta'} = \frac{M_s}{H}(D_\perp - D_\parallel) \cos \Theta' + \frac{1}{\cos^2 \Theta'} \quad (3.15)$$

We have to solve equation (3.12a) at  $\theta = 0$  to get  $\Theta'_0$ . Three solutions result in an energy minimum only for the conditions derived from the second derivative (3.12b):

$$\Theta'_0 = 0 \quad \Leftrightarrow \quad H > -M_s(D_\perp - D_\parallel) \quad (3.16a)$$

$$\Theta'_0 = \pi \quad \Leftrightarrow \quad H < M_s(D_\perp - D_\parallel) \quad (3.16b)$$

$$\Theta'_0 = \pm \arccos \left( -\frac{H}{M_s(D_\perp - D_\parallel)} \right) \quad \Leftrightarrow \quad |H| < |M_s(D_\perp - D_\parallel)| \quad \text{for} \quad (D_\perp - D_\parallel) < 0 \quad (3.16c)$$

---

<sup>b</sup>In particular, we can use  $\sin(\theta - \Theta') \approx \theta \cos \Theta' - \sin \Theta'$ .

One more condition  $|H| > |M_s(D_\perp - D_\parallel)|$  for  $(D_\perp - D_\parallel) > 0$  is invalid as an argument for the arccos in equation (3.16c). We can now substitute the solutions (3.16) in the expansion (3.14):

$$\Theta'(\theta) = \begin{cases} \frac{H}{H + M_s(D_\perp - D_\parallel)} \cdot \theta & \text{for (3.16a)} \\ \pi + \frac{H}{H - M_s(D_\perp - D_\parallel)} \cdot \theta & \text{for (3.16b)} \\ \pm \arccos\left(-\frac{H}{M_s(D_\perp - D_\parallel)}\right) + \frac{H^2}{M_s^2(D_\perp - D_\parallel)^2 - H^2} \cdot \theta & \text{for (3.16c)} \end{cases} \quad (3.17)$$

This is the optimal polar angle of the magnetization within a magnetic particle of prolate ellipsoidal shape in configurations [\[1\]](#) and [\[2\]](#), for any given applied field and as a function of the cantilever deflection angle, see figure 3.4.

### 3.4.4. Frequency Shift

To calculate the actual resonant frequency shift  $\Delta f \equiv \frac{\Delta\omega}{2\pi}$  of the DCM sample-on-cantilever system for configurations [\[1\]](#) and [\[2\]](#), according to equation (3.9), we rewrite  $\Delta\omega$  for  $\Phi' = 0$  with the energy (3.4):

$$\Delta\omega = \frac{\omega_0}{2k_0l_e^2} \cdot \left[ -\mu_0VM_sH \left( \cos\Theta'_0 \left( 1 - \frac{\partial\Theta'}{\partial\theta} \Big|_{\theta=0} \right)^2 - \sin\Theta'_0 \frac{\partial^2\Theta'}{\partial\theta^2} \Big|_{\theta=0} \right) + \mu_0VM_s^2(D_\perp - D_\parallel) \left( \cos 2\Theta'_0 \left( \frac{\partial\Theta'}{\partial\theta} \Big|_{\theta=0} \right)^2 + \sin\Theta'_0 \cos\Theta'_0 \frac{\partial^2\Theta'}{\partial\theta^2} \Big|_{\theta=0} \right) \right] \quad (3.18)$$

Using equations (3.15) and (3.16) to substitute known quantities in (3.18) leads to

$$\Delta f(H) = \begin{cases} \frac{f_0}{2} \frac{\mu_0VM_sH}{k_0l_e^2} \frac{M_s(D_\perp - D_\parallel)}{H + M_s(D_\perp - D_\parallel)} & \text{for } H > -M_s(D_\perp - D_\parallel) \\ \frac{f_0}{2} \frac{\mu_0VM_sH}{k_0l_e^2} \frac{M_s(D_\perp - D_\parallel)}{H - M_s(D_\perp - D_\parallel)} & \text{for } H < M_s(D_\perp - D_\parallel) \\ \frac{f_0}{2} \frac{\mu_0VM_sH}{k_0l_e^2} \frac{H}{M_s(D_\perp - D_\parallel)} \frac{2H^2 - M_s^2(D_\perp - D_\parallel)^2}{M_s^2(D_\perp - D_\parallel)^2 - H^2} & \text{for } |H| < |M_s(D_\perp - D_\parallel)| \\ & \text{and } (D_\perp - D_\parallel) < 0 \end{cases} \quad (3.19)$$

for configurations [\[1\]](#) ( $D_\perp > D_\parallel$ ) and [\[2\]](#) ( $D_\perp < D_\parallel$ ).

These formulae serve to describe the response of a magnetic sample-on-cantilever system to an applied magnetic field within the assumptions of the Stoner-Wohlfarth model. The torque acting on the cantilever, as a result of magnetization and applied field, stiffens or softens the cantilever, such that the resonant frequency shifts. The first factor in each formula of (3.19) scales the resonant frequency with respect to a simple harmonic oscillator. The second factor represents a normalized torque, see (2.11). The third (and fourth) factor is a result of the shape anisotropy of the magnetic sample and includes the factor  $(D_\perp - D_\parallel)$ , which we call ‘‘net anisotropy’’ with respect to the plane of the cantilever oscillation.

### 3.4.5. Discussion

#### On The Solutions

For clarity, we plot the solutions (3.17) and (3.19) in figure 3.4. The upper row shows the optimal angle  $\Theta'(\theta=0)$  of the magnetization from equation (3.17) for zero cantilever deflection vs. the reduced applied field  $h \equiv \frac{H}{M_s(D_{\perp}-D_{\parallel})}$  for configurations **1** and **2**, expressed by  $\cos \Theta'$  and  $\sin \Theta'$  as projection in the  $\hat{z}'$ - and the  $\hat{y}'$ -direction, respectively. The lower row shows the torque-reduced relative frequency shift  $\Delta f/f_0$  from equation (3.19) vs.  $h$  for both configurations. Additional grid lines are horizontal and vertical asymptotes.

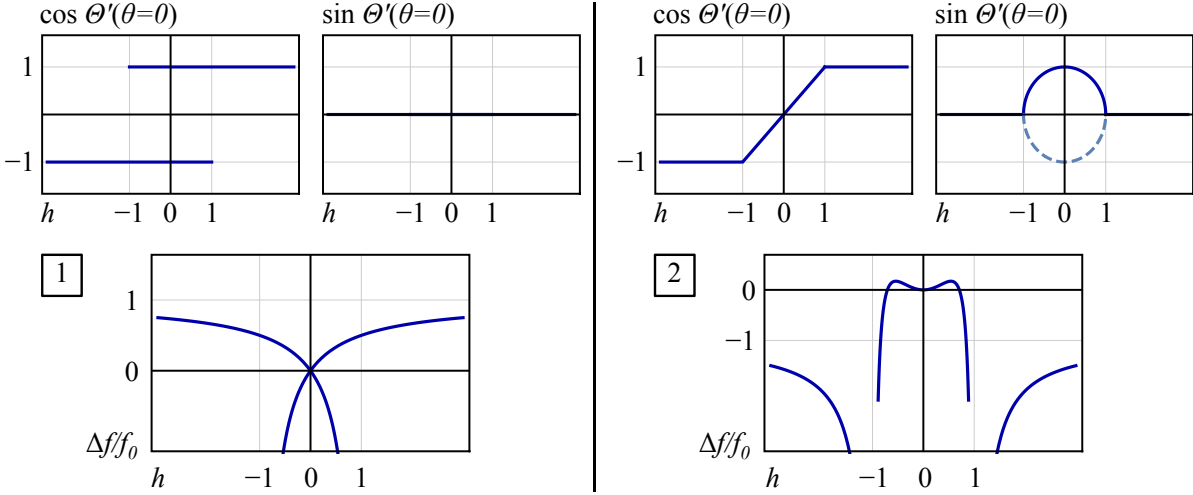


Figure 3.4. | Graphs of the torque-reduced relative frequency shift  $\Delta f/f_0$  vs. the reduced applied field  $h$  from equations (3.19) for configurations **1** and **2**. Dashed lines are horizontal and vertical asymptotes.

The multiple solutions (3.17) to the minimization problem represent different domains for the applied field. Validity of each solution switches at coercivity ( $|h| = 1$ ). Non-differentiable points at  $|h| = 1$  in angle are reflected by singularities in frequency shift, where the magnetization—physically impossible—seems to change its angle “immediately”, which would lead to an infinite torque.

High field branches ( $|h| > 1$ ) represent magnetization behavior according to the first two solutions of (3.17). At high field the system is in a stable local energy minimum, see figure 2.6. The optimal angles of the magnetization for both configurations then are equal and aligned to the applied field, where  $\cos \Theta' = 1$  corresponds to the  $+\hat{z}'$ -direction, and  $\cos \Theta' = -1$  to the  $-\hat{z}'$ -direction. For high applied field there is no component of the magnetization in  $\hat{y}'$ -direction,  $\sin \Theta' = 0$ .

At low field ( $|h| < 1$ ), it depends on the configuration whether the first two equations of (3.17) are valid (configuration **1**), or only the third solution (configuration **2**). Hence, we find one of two constant optimal angles of the magnetization for configuration **1**, and a smooth transition for the angle in configuration **2**. Both angle and frequency in configuration **1** show

magnetic hysteresis: Following one branch, passing coercivity, the second branch already is a valid solution, but is physically not occupied, until the metastable energy minimum associated with the first branch vanishes. At that point a jump to the second branch occurs, see also figures 2.6 and 3.3.

From the angle graphs in figure 3.4 at low field ( $|h| < 1$ ) we can see, that in configuration 1 the magnetization either points to the  $+\hat{z}'$ -direction, or to the  $-\hat{z}'$ -direction, depending on the applied magnetic field sweep history. There is no component in  $\hat{y}'$ -direction for any applied field (and neither in  $\hat{x}'$ -direction, by early assumption before entering calculation). In configuration 2 the angle graphs show a smooth transition for the magnetization from the  $+\hat{z}'$ - to the  $-\hat{z}'$ -direction. The projection to the  $y'$ -axis reveals the coherent rotation of the magnetization: When the  $z'$ -component of the magnetization is zero, the magnetization in fact is directed in  $\hat{y}'$ -direction, thus rotated towards the particle easy axis.

### On Sign Changes

According to equation (3.19) the frequency shift for both configurations in the high field limit differs by just a sign: The net anisotropy ( $D_{\perp} - D_{\parallel}$ ) for configuration 1 is positive (“positive anisotropy”, i.e. easy axis along  $\hat{z}'$ ), whereas for 2 it is negative (“negative anisotropy”, i.e. hard axis along  $\hat{z}'$ ).

The sign of the frequency shift in (3.9) is attributed to the curvature of the total magnetostatic energy as a function of the cantilever deflection angle  $\theta$ : For any given applied field, the magnetization will find its optimal angle with respect to that field *and* the anisotropy of the magnetic particle. Assuming these parameters fixed, oscillating the cantilever by a very small angle  $\theta$  then is equivalent to probing how optimal the alignment of the sample with respect to the fixed parameters is. If the sample alignment is close to an optimum with respect to the (fixed) applied field and magnetization, such that the energy is minimal, oscillation will yield a positive frequency shift for a positive energy landscape curvature. In case the alignment is rather unfavorable the measurement reveals a maximum in energy, i.e. a negative frequency shift. For clarity: The magnetization *is* at an optimal angle for the given applied field and given sample alignment (“configuration”). But if the sample were not fixed, similar to a compass needle, it may rotate to optimize *its* alignment. The stiffness of the cantilever is the reason for that rotation being prevented, and the counteracting torque in essence is measurable as a frequency shift.

In configuration 2 the smooth transition of the magnetization angle is reflected in frequency shift by sign changes: For very low applied field (around zero), the magnetization in its optimal angle is almost parallel to the easy axis, such that probing the alignment of the magnetic particle means finding it close to a minimum in energy. If the applied field increases a little bit, the optimal angle of the magnetization rotates away from the easy axis, towards the applied field direction. Now probing the alignment of the magnetic particle first reveals a zero frequency shift, namely the point of intermediate alignment at  $\pi/4 = 45^\circ$ , and then a negative frequency shift, when the alignment of particle and magnetization becomes unfavorable, what is called exhibiting negative anisotropy.

## On A General Solution

A general solution to the energy minimization problem is possible, but tedious due to the dependence of the magnetization angles  $\Theta'(\theta)$  and  $\Phi'(\theta)$  on the cantilever oscillation angle  $\theta$ . What can be found for the frequency shift for an ellipsoidal nanomagnet being in an arbitrary configuration with respect to the cantilever, is a combination of the characteristics of configurations [1], [2], and [3] [74]. In particular, plotting the projection of the magnetization to the  $z'$ -axis will result in a graph similar to figure 2.7, where the limiting hysteresis curves of a prolate ellipsoid in configurations [1] and [2] (as in figure 3.4), and transient configurations are shown. Consequently, a small misalignment of the particle principal axes with respect to the primed coordinate system (e.g. for non-ideal configurations [2] and [3]) is expected to cause hysteresis.

The frequency shift for an ellipsoidal nanomagnet in configuration [3] is expected to be zero for any applied field: The optimal angle of the magnetization in projection onto the circular sample cross-section is determined by the applied field only, since no shape anisotropy is apparent. As a consequence no torque is exerted on the cantilever. This expectation is supported by equation (3.20), describing high field behavior. Notably, we anticipate only even small deviation from the ideal alignment of configuration [3] to lead to measurable frequency shift in the first place, including hysteretic behavior. However, with respect to the applied field the alignment of a sample in configuration [3] and in configuration [2] is equivalent, so the magnetization states are expected to be identical for both configurations.

### 3.4.6. High Field Limit

For sufficiently high fields (HF) *in all three basic configurations* the magnetization points along the applied field  $\mathbf{M} \parallel \mathbf{H}$ , such that the polar angle of the magnetization equals the deflection angle  $\Theta' = \theta$ , and the azimuthal angle  $\Phi' = 0$ . The total energy of the sample-on-cantilever system (3.4) then becomes:

$$E_{tot, HF} = \frac{k_0}{2}(l_e \theta)^2 - \mu_0 V M_s H + \frac{\mu_0}{2} V M_s^2 (D_{\perp} \sin^2 \theta + D_{\parallel} \cos^2 \theta)$$

With (3.9) the resonant frequency shift is

$$\Delta f_{HF} = \frac{f_0}{2} \frac{\mu_0 V M_s^2}{k_0 l_e^2} (D_{\perp} - D_{\parallel}) \quad (3.20)$$

So for high fields in any configuration the resonant frequency shift is a constant and proportional to the net anisotropy. In particular, if the sample is an ellipsoidal nanomagnet, in configuration [3]  $D_{\perp} = D_{\parallel}$ , such that  $\Delta f_{HF} = 0$ .

### 3.4.7. Magnetization Curve

For experimentally given frequency shift data, we can produce a magnetization hysteresis curve similar to figure 2.2 by solving equation (3.19) for the saturation magnetization and transforming it into a function of the applied field,  $M_s \mapsto M(H)$ :

$$M(H) = \begin{cases} \frac{1}{VH} \left( \sqrt{\frac{\Delta f}{f_0} k_0 l_e^2 \cdot \left( \frac{\Delta f}{f_0} k_0 l_e^2 + \frac{2VH^2}{\mu_0(D_\perp - D_\parallel)} \right)} + \frac{\Delta f}{f_0} k_0 l_e^2 \right) & \text{for } H > -M_s(D_\perp - D_\parallel) \\ \frac{1}{VH} \left( \sqrt{\frac{\Delta f}{f_0} k_0 l_e^2 \cdot \left( \frac{\Delta f}{f_0} k_0 l_e^2 + \frac{2VH^2}{\mu_0(D_\perp - D_\parallel)} \right)} - \frac{\Delta f}{f_0} k_0 l_e^2 \right) & \text{for } H < M_s(D_\perp - D_\parallel) \end{cases} \quad (3.21)$$

Equation (3.19) assumes the magnetization  $M_s$  to be constant in magnitude and directed in its optimal angle, but the angle is not resolved in that equation. In configuration [1](#), the magnetization stays collinear with the applied field, whereas in configurations [2](#) and [3](#) coherent rotation takes place. Therefore only in configuration [1](#) the magnetization can be written as a function of the applied field, with no angular dependence, except for a sign. Then,  $\Delta f(H)$  is used as a parameter.

## 3.5. Derivation of Demagnetization Factors

### 3.5.1. Introduction

By magnetizing a ferromagnetic particle, a so called demagnetizing field is generated inside the particle (figure 2.3). This field generally is anisotropic and for poly- or noncrystalline particles only dependent on the shape of that particle (relation (2.7)). The shape anisotropy energy  $E_{ms}$  in equation (2.13) (and hence the resonant frequency shift (3.19)) is governed by the magnitude of that field, expressed in the demagnetization factors  $D_i$ . In the following the demagnetization factors for hollow nanotubes of hexagonal shape are derived for all three basic sample-on-cantilever configurations, corresponding to the samples we use for later experiments (section 4.3 and chapter 5).

The basis for the calculation of each demagnetization factor is the solution of Maxwell's magnetostatic equations [13], together with the boundary conditions of components  $H_\parallel$  and  $B_\perp$  being continuous parallel and perpendicular to the surface between two magnetic materials (section 2.2.3). These solutions are taken from literature (Osborn [19], Aharoni [75]), and adapted for our use.

For non-ellipsoidal magnetic samples neither the magnetization, nor the demagnetizing field is uniform. In approximation, uniformity of the fields can be achieved for sufficiently high applied fields. The demagnetization factors presented here are derived from fields averaged over the whole volume of the magnetic sample, called magnetometric demagnetization factors (section 2.2.3).



The shape of our samples roughly resembles a hollow cylinder (nanotube). The consideration of cylindrical magnetic samples in principle closely follows the earlier discussion for prolate ellipsoids in section 2.5, but for “ellipsoids” with polar and equatorial semi-axes  $a \gg b$ , i.e. an infinite aspect ratio. In this case of an infinitely long solid cylinder, the demagnetization factors are  $D_a = 0$ , and  $D_b = \frac{1}{2}$  [19], with  $D_a + 2D_b = 1$ . For each of the three basic configurations the combination of  $D_a$  and  $D_b$  for the coordinate directions  $\hat{x}'$ ,  $\hat{y}'$ , and  $\hat{z}'$  is as stated in table 2.1, section 2.5.2.

For hollow cylindrical samples, we expect a deviation of the demagnetizing field from the solid cylindrical sample due to the alteration of the topology. Numerical simulations suggest demagnetization factors in the range of  $D_b = 0.4\text{--}0.6$  [42]. However, since our samples are grown on a template with hexagonal cross-section, the topology is better described by a hollow prism with hexagonal cross-section, which we call a hexagonal nanotube.

### 3.5.2. Demagnetization Factors for a Hexagonal Nanotube

In order to determine the demagnetization factors for the calculation of the magnetostatic energy of a hexagonal nanotube (2.13), we start by considering a magnetic particle in the shape of a rectangular prism [75]. To resemble a hexagonally shaped hollow nanotube, we will arrange six of these prisms and superpose their individual contributions, neglecting any interaction between them.

See figure 2.4 for the primed coordinate system used in the following calculation. The unit vectors  $\hat{x}'$ ,  $\hat{y}'$ , and  $\hat{z}'$  align to the spanning of the dimensions  $a$ ,  $b$ , and  $c$  of one prism, respectively, as in [75] and figure 3.5. The magnetic field is applied in  $\hat{z}'$ -direction and the demagnetization factor  $D_c(a, b, c)$  in  $\hat{z}'$ -direction as a function of the dimensions is taken from [75]. Further demagnetization factors  $D_a(b, c, a)$  and  $D_b(c, a, b)$  (in  $\hat{x}'$ - and  $\hat{y}'$ -direction, respectively) for that same prism can be derived by applying the cyclic permutation  $(a\ b\ c)$ , i.e.  $a \mapsto b \mapsto c \mapsto a$ , twice.

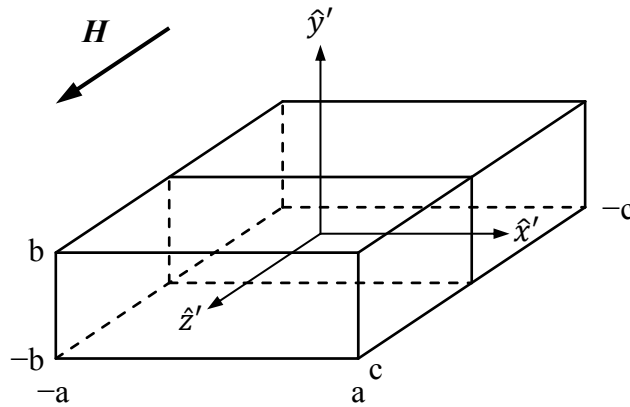


Figure 3.5. | Schematic diagram of the coordinate system used for equation (3.22). The magnetic field is applied in  $\hat{z}'$ -direction. Diagram similar to and adapted from [75].

$$\begin{aligned}
\pi \cdot D_c(a, b, c) = & \frac{\sqrt{a^2 + b^2 + c^2} (a^2 + b^2 - 2c^2)}{3abc} - \frac{(a^2 + b^2)^{3/2} + (a^2 + c^2)^{3/2} + (b^2 + c^2)^{3/2}}{3abc} \\
& + \frac{a^3 + b^3 - 2c^3}{3abc} + \frac{c}{ab} \left( \sqrt{a^2 + c^2} + \sqrt{b^2 + c^2} \right) + 2 \arctan \left( \frac{ab}{c\sqrt{a^2 + b^2 + c^2}} \right) \\
& + \frac{b^2 - c^2}{2bc} \ln \left( \frac{\sqrt{a^2 + b^2 + c^2} - a}{\sqrt{a^2 + b^2 + c^2} + a} \right) + \frac{a^2 - c^2}{2ac} \ln \left( \frac{\sqrt{a^2 + b^2 + c^2} - b}{\sqrt{a^2 + b^2 + c^2} + b} \right) \\
& + \frac{b}{2c} \ln \left( \frac{\sqrt{a^2 + b^2} + a}{\sqrt{a^2 + b^2} - a} \right) + \frac{a}{2c} \ln \left( \frac{\sqrt{a^2 + b^2} + b}{\sqrt{a^2 + b^2} - b} \right) \\
& + \frac{c}{2b} \ln \left( \frac{\sqrt{a^2 + c^2} - a}{\sqrt{a^2 + c^2} + a} \right) + \frac{c}{2a} \ln \left( \frac{\sqrt{b^2 + c^2} - b}{\sqrt{b^2 + c^2} + b} \right) \tag{3.22}
\end{aligned}$$

There exist three basic sample-on-cantilever configurations, which differ in the orientation of the sample long axis with respect to the cantilever axis  $\hat{z}'$  (see figure 2.6 and 3.6). For each of these configurations we choose a primary prism (the side of the hexagonal nanotube touching the cantilever) of width  $w$ , thickness  $t$ , and length  $l$ , and calculate its demagnetization factors:

	$\hat{x}'$	$\hat{y}'$	$\hat{z}'$	$D_w$	$D_t$	$D_l$
	$a$	$b$	$c$			
1	$w$	$t$	$l$	$D_a(w, t, l) = D_c(t, l, w)$	$D_b(w, t, l) = D_c(l, w, t)$	$D_c(w, t, l)$
2	$t$	$l$	$w$	$D_c(t, l, w)$	$D_a(t, l, w) = D_c(l, w, t)$	$D_b(t, l, w) = D_c(w, t, l)$
3	$l$	$t$	$w$	$D_c(l, t, w)$	$D_b(l, t, w) = D_c(w, l, t)$	$D_a(l, t, w) = D_c(t, w, l)$

**Table 3.1.** | On the left, list of dimensions of the primary prisms for the three basic sample-on-cantilever configurations, according to figure 3.5. On the right, demagnetization factors  $D_w$ ,  $D_t$  and  $D_l$  of those primary prisms, as calculated with the help of equation (3.22).

The demagnetization factors of the five other prisms are derived from the primary one. In order to do so, we recall the shape anisotropy energy term  $E_{ms}$  from equation (2.13) and rewrite it as a sum of the energies of each of the six prisms:

$$\begin{aligned}
E_{ms} = & \frac{\mu_0}{2} V M_s^2 \left( (D_x \sin^2 \Phi' + D_y \cos^2 \Phi') \sin^2 \Theta' + D_z \cos^2 \Theta' \right) \\
= & \frac{\mu_0 M_s^2}{2} \sum_{n=1}^6 V_n \left( (D_{x,n} \sin^2 \Phi' + D_{y,n} \cos^2 \Phi') \sin^2 \Theta' + D_{z,n} \cos^2 \Theta' \right)
\end{aligned}$$

In a regular hexagon, for reasons of symmetry, we consider three prism pairs instead of six single prisms. In each prism, the demagnetizing field assumes a value, which corresponds to the angle between that prism and the applied field in in  $\hat{z}'$ -direction. We can use  $\cos 60^\circ = \frac{1}{2}$  and  $\cos 30^\circ = \frac{\sqrt{3}}{2}$ , see figure 3.6. Hence the demagnetization factors  $D_l$ ,  $D_w$ , and  $D_t$  (corresponding to the demagnetizing field components in the directions of the length, width, and thickness of each prism) each contribute only by a trigonometric factor  $\xi_{i,n}$  to the total demagnetizing field

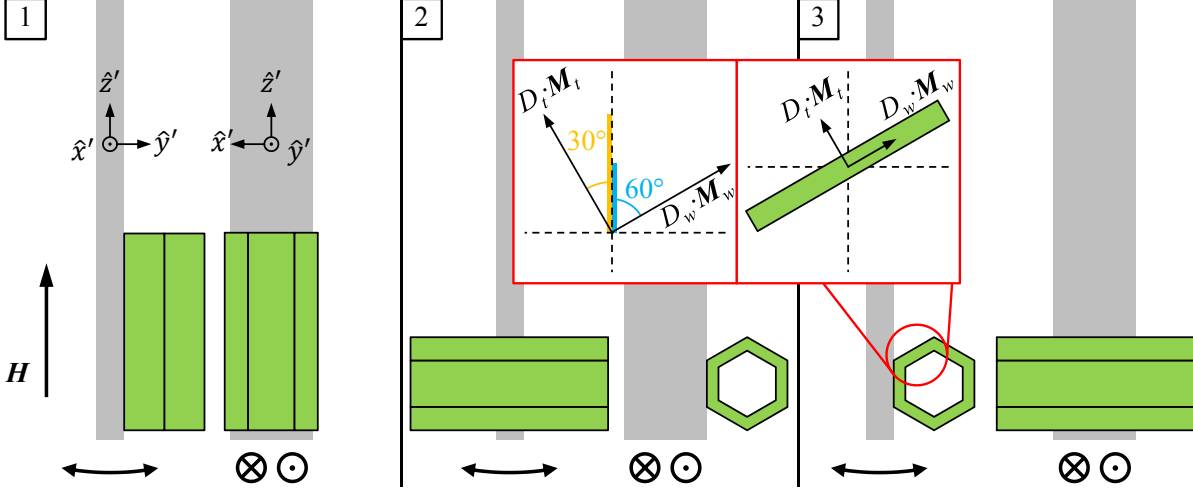


Figure 3.6. | Schematic diagram of the three basic sample-on-cantilever configurations (see also figure 2.6). From left to right three configurations [1], [2], and [3] are shown, each seen from the side in  $-\hat{x}'$ - and from the front in  $-\hat{y}'$ -direction. Grey areas symbolize the cantilever, black arrows below indicate the oscillation direction, green areas show the hexagonal nanotube facets. Inset exemplarily clarifies the orientation of the demagnetizing field projections within one prism for an applied field along the  $\hat{z}'$ -direction.

(figure 3.6). We derive the overall demagnetization factors from associating the  $\xi_{i,n}$  with their contribution to either  $D_x$ ,  $D_y$  or  $D_z$ .

$$\begin{aligned}
E_{ms} &= \frac{\mu_0 M_s^2}{2} \sum_{n=1}^3 2V_n \left( \underbrace{(\xi_{1,n} D_l + \xi_{2,n} D_w + \xi_{3,n} D_t)}_{D_{x,n}} \sin^2 \Phi' \right. \\
&\quad \left. + \underbrace{(\xi_{4,n} D_l + \xi_{5,n} D_w + \xi_{6,n} D_t)}_{D_{y,n}} \cos^2 \Phi' \right) \sin^2 \Theta' \\
&\quad \left. + \underbrace{(\xi_{7,n} D_l + \xi_{8,n} D_w + \xi_{9,n} D_t)}_{D_{z,n}} \cos^2 \Theta' \right) \\
&= \frac{\mu_0 M_s^2 V}{2} \left( \underbrace{\frac{1}{3} \sum_{n=1}^3 (\xi_{1,n} D_l + \xi_{2,n} D_w + \xi_{3,n} D_t)}_{D_x} \sin^2 \Phi' \sin^2 \Theta' \right. \\
&\quad \left. + \frac{1}{3} \sum_{n=1}^3 (\xi_{4,n} D_l + \xi_{5,n} D_w + \xi_{6,n} D_t) \cos^2 \Phi' \sin^2 \Theta' \right. \\
&\quad \left. + \frac{1}{3} \sum_{n=1}^3 (\xi_{7,n} D_l + \xi_{8,n} D_w + \xi_{9,n} D_t) \cos^2 \Theta' \right) \quad (3.23) \\
&\quad \underbrace{\hspace{10em}}_{D_z}
\end{aligned}$$

This relation leads to the demagnetization factors  $D_x$ ,  $D_y$ , and  $D_z$  of a hexagonal nanotube for the three basic sample-on-cantilever configurations, see table 3.2. For the samples used in our experiments, the calculations are carried out in appendix A.2.

	$D_x$	$D_y \equiv D_\perp$	$D_z \equiv D_\parallel$
1	$\frac{2}{3}D_w + \frac{1}{\sqrt{3}}D_t$	$\frac{1}{\sqrt{3}}D_w + \frac{2}{3}D_t$	$D_l$
2	$\frac{1}{\sqrt{3}}D_w + \frac{2}{3}D_t$	$D_l$	$\frac{2}{3}D_w + \frac{1}{\sqrt{3}}D_t$
3	$D_l$	$\frac{1}{\sqrt{3}}D_w + \frac{2}{3}D_t$	$\frac{2}{3}D_w + \frac{1}{\sqrt{3}}D_t$

Table 3.2. | Demagnetization factors  $D_x$ ,  $D_y$ , and  $D_z$  of a hexagonal nanotube for the three basic sample-on-cantilever configurations, including the factors  $\xi_{i,n}$  of equation (3.23), derived with the help of figure 3.6.

# 4. Experimental Setup

## 4.1. Introduction

In this chapter, we turn toward the specific components used to conduct dynamic cantilever magnetometry (DCM) measurements on ferromagnetic nanotubes. We specify the properties of the ultrasoft cantilever in section 4.2, and the probed samples in section 4.3. The experiments are carried out for two sets of nanotubes, each set grown in the same process, and each probed in the three basic configurations. Ni and CoFeB nanotubes are affixed to the tip of the cantilever as described in section 4.4. The basic technique of attaching samples to the tip of a cantilever can be used for a variety of experiments, we illuminate different possibilities of doing so in section 4.5. The measurement apparatus and the experimental procedure to obtain DCM data are explained in section 4.6.

## 4.2. Cantilever

The results presented in this thesis are obtained using DCM (section 3.3). The main component of this technique is a mechanical oscillator exhibiting beam-like shape, clamped at one end, free at the other, in the so-called cantilever configuration. As depicted in figure 4.1 (scanning electron microscopy (SEM) image), the cantilevers are fabricated as a part of a larger single-crystal Si substrate, defined by etching and left held by a Si chip holding three of such cantilevers [76]. Each experiment is carried out with yet another cantilever, i.e. each magnetic sample is affixed to its own cantilever, see section 4.4.

The cantilevers used here are about  $150\ \mu\text{m}$  long,  $3.5\ \mu\text{m}$  wide (shaft) and  $0.12\ \mu\text{m}$  thick. The cantilevers include a mass-loaded end (see figure 3.2) of  $18\ \mu\text{m}$  length,  $4.9\ \mu\text{m}$  width, and  $1.7\ \mu\text{m}$  thickness [76]. The motion of the cantilevers is detected by laser light<sup>a</sup> focused onto a  $11\ \mu\text{m}$ -wide paddle near the mass-loaded end [65]. The very end of the cantilever mass is tapered to a  $1\ \mu\text{m}$ -wide tip.

At  $T = 4.2\ \text{K}$  and at zero field the cantilevers (including nanotube samples) have resonant frequencies from  $2.1\ \text{kHz}$  to  $2.8\ \text{kHz}$  and quality factors  $Q_0$  from  $22 \cdot 10^3$  to  $42 \cdot 10^3$ . Their spring constants  $k_0$  are determined to range from  $40\ \mu\text{N/m}$  to  $70\ \mu\text{N/m}$ . We measure a negligible dependence of the mechanical dissipation on the applied magnetic field beyond that intrinsic

---

<sup>a</sup>Fiber optical laser interferometry [65], methods see section 4.6.

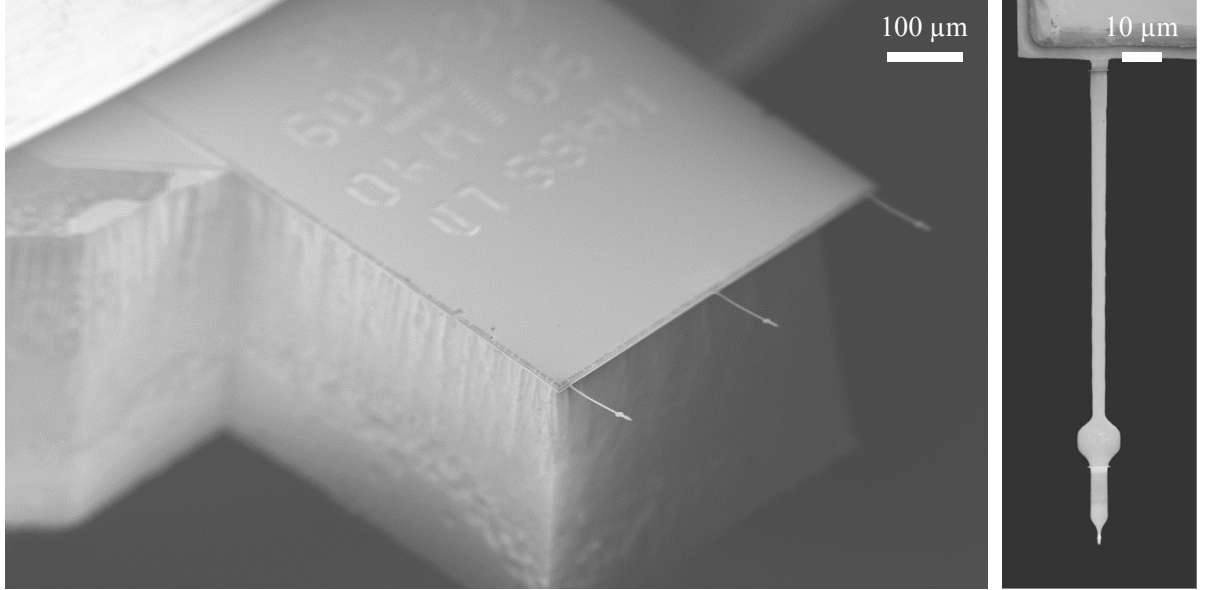


Figure 4.1. | SEM images of ultrasoft Si cantilevers held by a Si chip. On the right, detail of one cantilever.

to Si cantilevers [77]. Detailed data on the mechanical properties of the cantilevers used can be found in appendices B.1 and B.2.

The use of an effective length  $l_e$  in our calculations takes into account the mode shape of a deflected cantilever and is defined in figure 3.1. The fundamental mode shape and effective length of a cantilever as used in the experiments are calculated numerically, shown in figure 4.2 (finite element method, COMSOL Multiphysics, from [67]). In the figure, the graph on top shows the fundamental oscillation mode shape for the relative deflection  $y/y_{max}$  as a function of the relative cantilever position  $z/l$ , calculated for an oscillation amplitude  $y_{max} = 40$  nm and cantilever length  $l = 155$   $\mu\text{m}$ . A linear extrapolation on the 17  $\mu\text{m}$  long mass-loaded end of the cantilever reveals the effective length  $l_e = 0.70 \cdot l = 108$   $\mu\text{m}$ . The calculation is performed for small deflections  $y_{max}/l_e < 0.03^\circ \ll 1$  on the basis of the coordinates shown in figure 3.2. The motion of the cantilever is detected at its paddle (red marking,  $z/l = 0.85$ ), therefore the tip deflection is larger by a factor  $c = 1.27$ .

Below in figure 4.2, a graphical representation of numerical calculation data is given for the fundamental mode, and the second and third harmonics of the cantilever oscillation. Color from blue to red encodes increasing displacement. Where the first two harmonics only show one-dimensional deflection in the  $\hat{y}$ -direction, for the third harmonics a torsional mode enters. The eigenfrequencies are determined to be  $f_0 = 2.6$  kHz,  $f_1 = 34.6$  kHz, and  $f_2 = 73.2$  kHz, therefore we do not expect mode coupling.

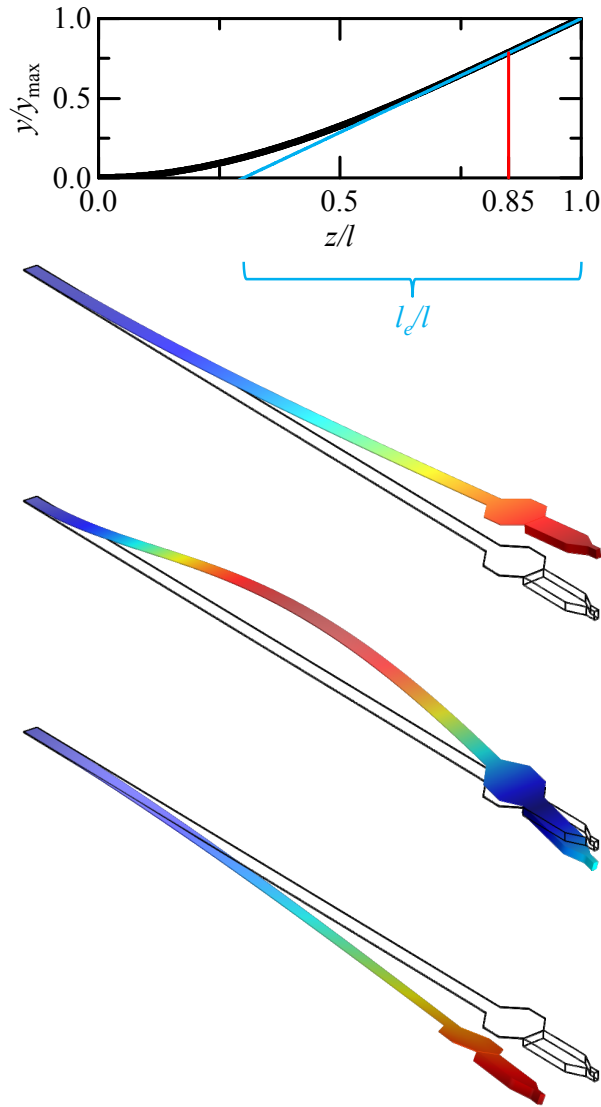


Figure 4.2. | Graph and numerical calculation for the fundamental mode shape and the first three harmonics of a cantilever as used in the experiments. In the graph, the effective length  $l_e$  is marked in blue, and the paddle position in red, coordinates on the basis of figure 3.2. For the numerical data, color from blue to red encodes increasing displacement. Numerical data from [67].

## 4.3. Magnetic Sample

### 4.3.1. Introduction

Ferromagnetic nanotubes are particularly interesting for their magnetization states, since the low-dimensionality of these structures results in magnetic configurations not present in macroscopic magnets [31, 34, 44, 78]. These structures avoid magnetization point singularities as present in solid magnetic cylinders [28], but support core-free magnetization states as a prerequisite for fast and controllable magnetization reversal, for example via the curling mode,

vortex wall formation, and propagation [29, 32, 36, 37, 50]. Additionally, possible dynamic effects during magnetization reversal include magnetic domain wall movement thus generating spin waves [73].

The magnetic samples that we are interested in are in the shape of a hollow prism with hexagonal cross-section and a very high aspect ratio above 30 : 1, which we call magnetic nanotube. The magnetic material is supported by a non-magnetic template, such that the samples exhibit a core-shell structure, using a hexagonally shaped GaAs nanowire as a core, and a grown shell of magnetically isotropic material, as shown in figure 4.3.

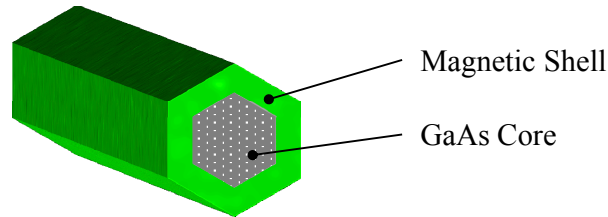


Figure 4.3. | Illustration of the principal structure of the investigated samples. The magnetic shell material (green) is supported by GaAs core material (grey).

For this thesis, two different sets of magnetic samples are probed. Within each set the samples undergo the same fabrication process. One set of samples is processed to be Ni nanotubes, the other to be CoFeB nanotubes. To characterize the samples, three nanotubes of each set are randomly chosen to be affixed to the tip of an ultrasoft cantilever in one of three basic configurations, see figure 4.8 and section 4.4. The Ni samples are named N1, N2, and N3, and the CoFeB samples are named C1, C2, and C3, accordingly.

### 4.3.2. Ni Nanotubes

The Ni nanotubes we use in the experiment consist of a GaAs core and a Ni shell. In a two-step process, first, GaAs nanowires are grown on a Si(111) substrate in a self-catalysed growth mode by means of molecular beam epitaxy (MBE) [40]. Second, the Ni shell is fabricated by atomic layer deposition (ALD). ALD is a chemically assisted deposition technique, which leads to a conformal coating of the covered surface [79]. During the process, an  $\text{Al}_2\text{O}_3$  capping layer is applied to the GaAs template, to prevent As from diffusing into the magnetic shell. Using successive precursor pulses the magnetic Ni layer is deposited. Finally  $\text{NiO}_x$  is reduced to metallic nickel. The Ni shell is polycrystalline, and therefore the Ni nanotube is found to exhibit *no* magneto-crystalline anisotropy [40]. The actual composition of the magnetic shell consists of Ni (80.1%),  $\text{Al}_2\text{O}_3$  (14.3%), and O (5.6%) in layers of 40 nm  $\text{NiO}_x$  and 25 nm  $\text{AlO}_x$  [80]. The nanotube fabrication process is performed by D. Ruffer<sup>b</sup> (GaAs nanowires),

---

<sup>b</sup>Laboratoire des matériaux semiconducteurs (LMSC) de l'institut des matériaux (IMX) et Section de science et génie des matériaux (SMX), Faculté des sciences et techniques de l'ingénieur (STI), Ecole polytechnique fédérale de Lausanne (EPFL), 1015 Lausanne, Suisse.



R. Huber<sup>c</sup>, and T. Schwarze<sup>c</sup> (Ni shell), material analysis by J. Arbiol<sup>d</sup> [22]. The saturation magnetization of Ni thin films [81] and ultrafine particles [82] at low temperatures is known to be between  $\mu_0 M_s = 0.56$  T to 0.63 T.

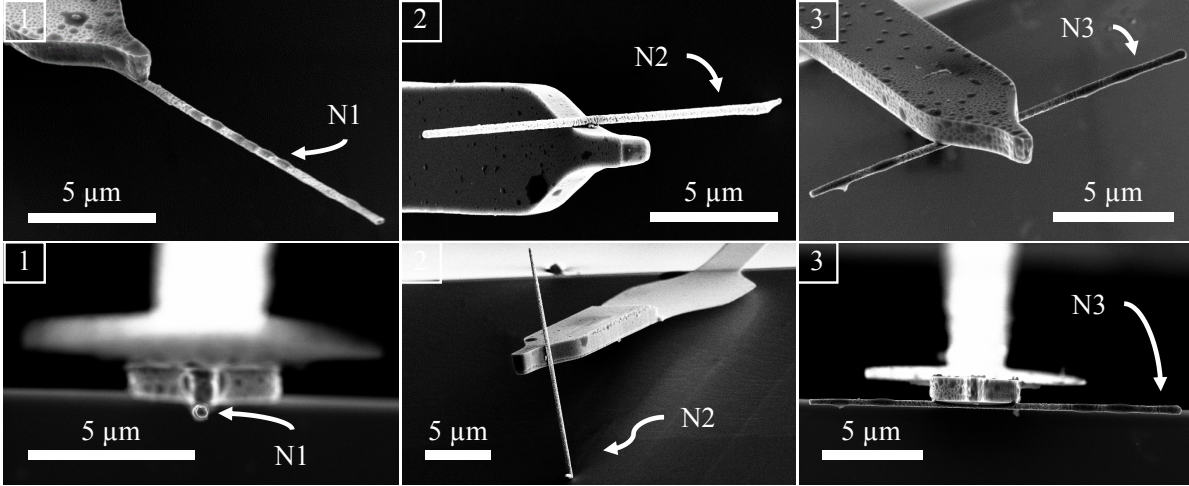


Figure 4.4. | SEM images showing the three basic configurations [1], [2], and [3] of the Ni nanotubes N1, N2, and N3, each affixed to the tip of an ultrasoft Si cantilever.

In figure 4.4 we show SEM images of the three samples N1, N2, and N3. Each nanotube is affixed to the tip of an ultrasoft Si cantilever in one of the three basic configurations. The nanotubes have lengths of about 20  $\mu\text{m}$ . Since the GaAs nanowires have the shape of a slightly sloped truncated cone, the nanotubes have an outer diameter which narrows from 380 nm to 270 nm. For detailed geometrical properties refer to appendix B.1.

In figure 4.5 we show SEM images of parts of the Ni nanotubes N1, N2, and N3. The upper row is showing N1 close to the cantilever, some middle part of N3, and one end of N3. From these details, the surface structure of the Ni nanotubes is visible. Rather than a smooth surface, slots and dents can be recognized, some of them approximately reaching down to the template material of the nanotube. The Ni shell is found to exhibit a surface roughness with peak-to-peak values of about 10 nm [40, 50]. The hexagonal structure of the GaAs template is not conformally repeated on the surface of the nanotube. Instead, the outer perimeter of the nanotubes—apart from the roughness—is rather circular in cross-section. In the lower row of figure 4.5, on the left, the hexagonal GaAs template is visible reaching out at one end of the nanotube N2. On the right hand side a detailed SEM image of a magnetic material extrusion at the other end of N2 is shown.

The liquid-like material visible on the cantilevers and nanotubes of figures 4.4 and 4.5 is likely due to hydrocarbon adsorption during the long periods in the cryogenic measurement system and/or leftover glue from the fabrication process (see section 4.4). This material is

<sup>c</sup>Lehrstuhl für Physik funktionaler Schichtsysteme, Physik Department E10, Technische Universität München, 85747 Garching, Deutschland.

<sup>d</sup>Institució Catalana de Recerca i Estudis Avançats (ICREA), Group of Advanced Electron Nanoscopy (GAeN) and Institut de Ciència de Materials de Barcelona (ICMAB-CSIC), Campus de la Universitat Autònoma de Barcelona, 08193 Bellaterra, España.

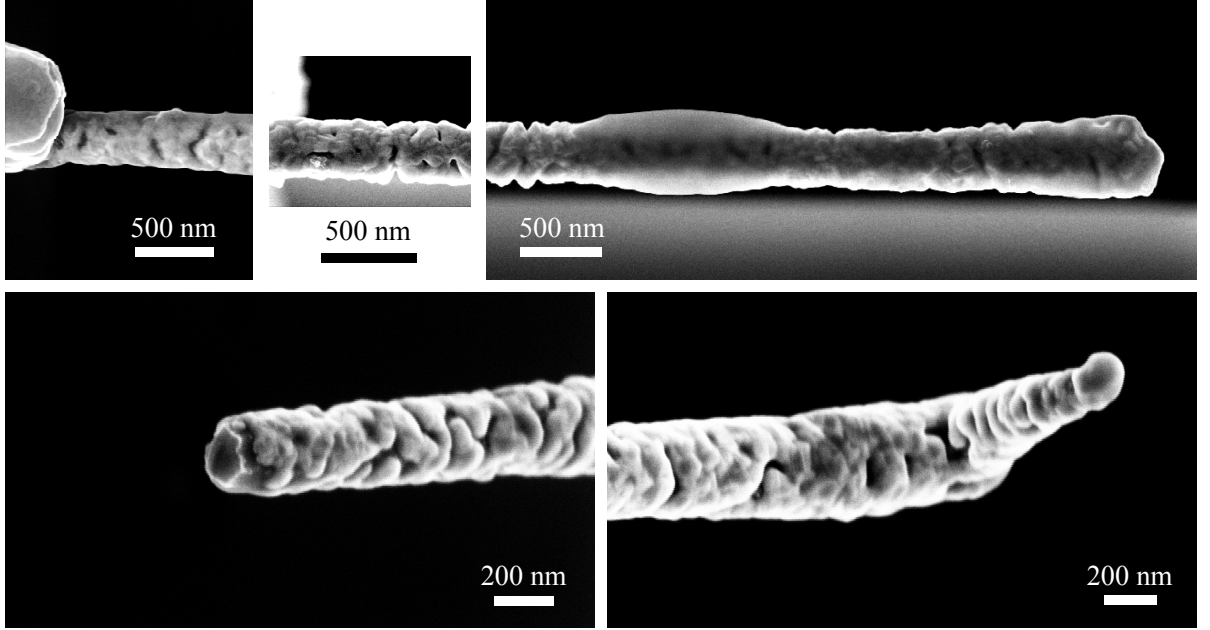


Figure 4.5. | SEM images showing parts of the Ni nanotubes N1, N2, and N3. In the upper row, one can see N1 close to the cantilever, some middle part of N3, and one end of N3. The liquid-like material visible on N3 likely is leftover glue from the fabrication process. Below both ends of N2 are shown. Note the GaAs template visible on the left, and the extrusion on the right.

non-magnetic and has not been seen to affect the magnetic response of our measurements. It will, however, shift the mechanical resonant frequency of the cantilever due to the increase in mass. This shift is later compensated by considering only the relative frequency shift during data analysis. Note, that the small material extrusion at one end of N2 may influence the net anisotropy of the sample.

The considerations of section 3.5 leading to equation (3.23) and the demagnetization factors of table 3.2 are based on a hexagonal nanotube made up of six separate rectangular prisms. We use this approximation to describe the Ni nanotubes. We expect this approximation to be valid, first, due to the hexagonal shape of the GaAs template nanowire (determining the inside shape of the Ni nanotube), and second, the approximation of the almost circular perimeter of the Ni nanotube by a hexagon: Where for a circle the ratio of “outer” and “inner” radius is 1, for a hexagon it is already  $\approx 1.15$ . Given the volume of the Ni nanotubes (appendix B.1), we can find the average facet size of a regular hexagonal nanotube with the same volume and shell thickness. From there we can calculate the expected demagnetization factors of Ni nanotubes in the three basic configurations as carried out in appendix A.2:

	$D_x$	$D_y \equiv D_{\perp}$	$D_z \equiv D_{\parallel}$	$(D_{\perp} - D_{\parallel})$
N1	0.597	0.645	0.002	0.643
N2	0.645	0.002	0.597	-0.595
N3	0.002	0.644	0.598	0.046

Table 4.1. | Demagnetization factors  $D_x$ ,  $D_y$ , and  $D_z$ , and the net anisotropy  $(D_{\perp} - D_{\parallel})$  calculated for the three Ni nanotubes of the three basic configurations.

### 4.3.3. CoFeB Nanotubes

Very similar to the Ni nanotubes, the CoFeB nanotubes used in our experiments consist of a GaAs core and magnetic shell material. In a two-step process, first, GaAs nanowires are grown on a Si(111) substrate using Ga droplets as catalysts by molecular beam epitaxy (MBE) [83]. Second, the CoFeB shell is fabricated by sputter deposition. Sputter deposition is a physical vapor deposition method, which involves the ejection of target material onto a substrate. Here, Xe ions are accelerated from a source into the  $\text{Co}_{20}\text{Fe}_{60}\text{B}_{20}$  target material, which hence is ejected towards the Si substrate to form a thin film of  $(30.0 \pm 0.2)$  nm thickness on impact. By rotating the substrate sample holder, it is possible to obtain homogeneously thick CoFeB shells. The boron is included only to avoid crystallization during the process, so there are only shape anisotropic effects in the amorphous shell material and no magneto-crystalline anisotropy is observed [84]. The actual composition of the magnetic shell consists of Fe (77%), Co (22%), and Xe (3%)<sup>e</sup> [83]. The nanotube fabrication process is performed by D. Ruffer<sup>b</sup> (GaAs nanowires), F. Heimbach<sup>c</sup>, and T. Rapp<sup>c</sup> (CoFeB shell), material analysis by J. Arbiol<sup>d</sup>. The saturation magnetization of the CoFeB shell has been reported by Schwarze and Grundler [72] to be  $\mu_0 M_s = 1.80$  T.

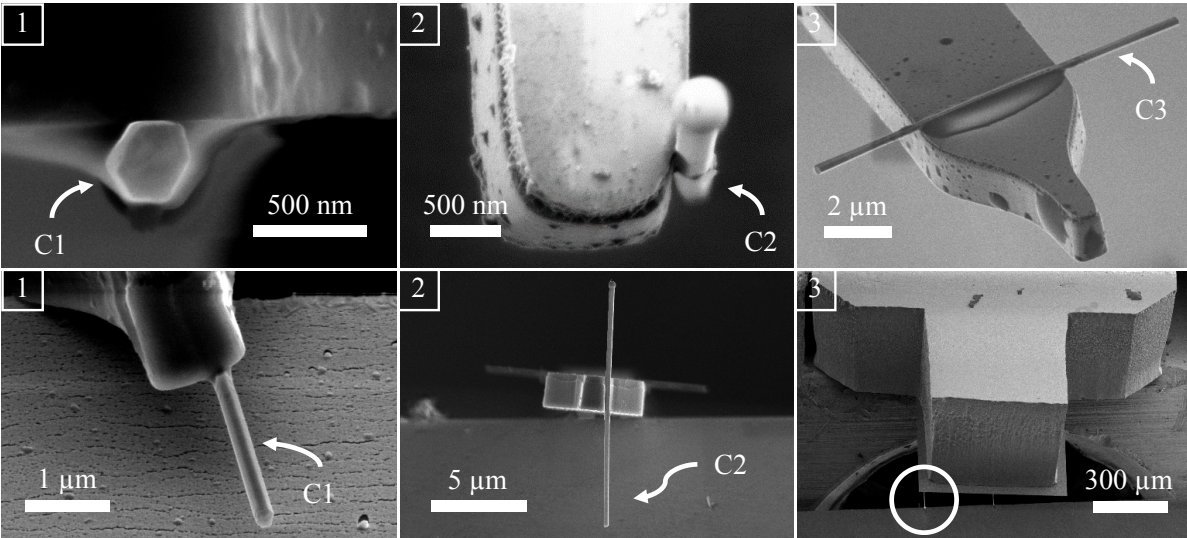


Figure 4.6. | SEM images showing the three basic configurations [1], [2], and [3] of the CoFeB nanotubes C1, C2, and C3, each affixed to the tip of an ultrasoft Si cantilever.

In figure 4.6 we show SEM images of the three samples C1, C2, and C3. Each nanotube is affixed to the tip of an ultrasoft Si cantilever in one of the three basic configurations. The nanotubes have lengths of about  $12 \mu\text{m}$ . Since the CoFeB nanotubes are hexagonal prisms, the total diameters are measured by SEM while facing both a facet, and an edge of the prism successively. Diameters are determined to be in the order of  $250 \text{ nm}$ . For detailed geometrical properties refer to appendix B.2.

<sup>e</sup>The content of boron cannot be obtained, since boron is not in range of the electron energy loss spectroscopy (EELS) performed in [83].

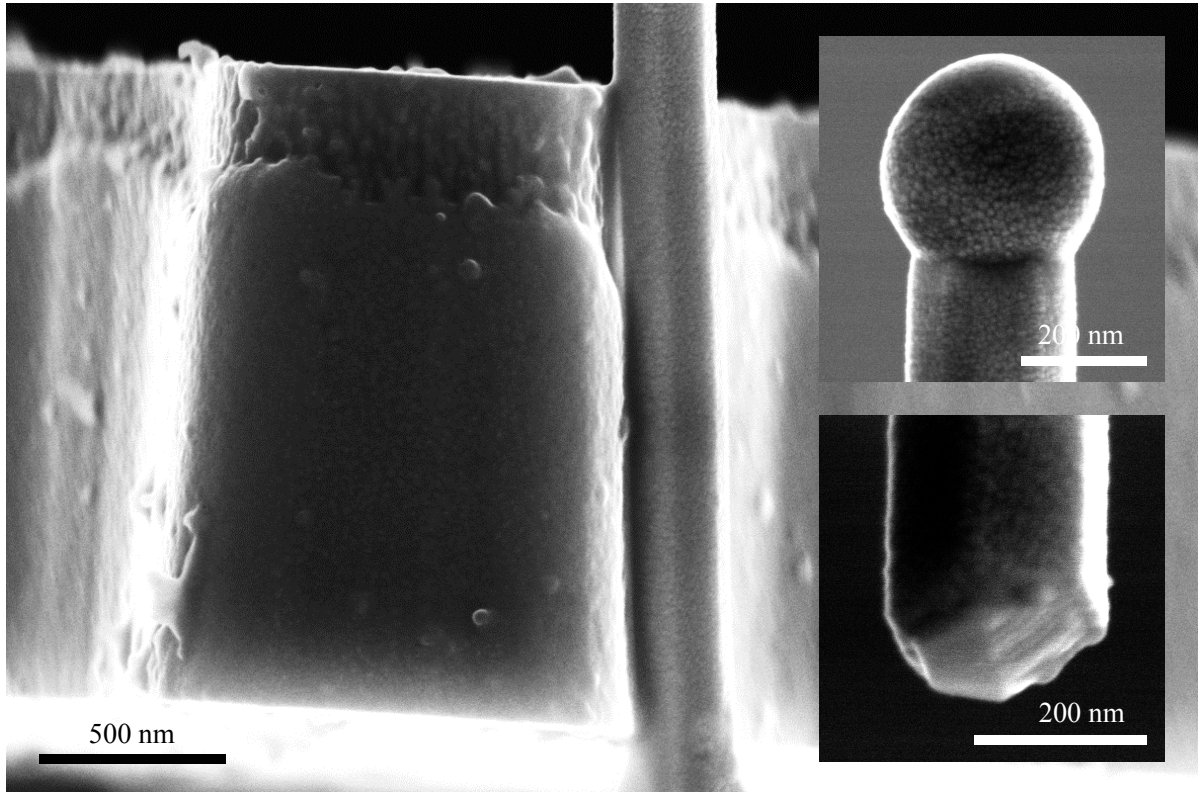


Figure 4.7. | SEM images showing parts of the CoFeB nanotube C2. In the main frame we see C2 affixed to an ultrasoft cantilever in configuration [2], facing the tip of the cantilever, and in the two insets, the two ends of C2 are depicted.

In figure 4.7 we show SEM images of parts of the CoFeB nanotube C2. In the main frame we see C2 affixed to an ultrasoft cantilever in configuration [2], facing the tip of the cantilever, and in the two insets, the two ends of C2 are depicted. The CoFeB shell surface is seen to be much smoother than compared to the Ni shell (section 4.3.2). The hexagonal cross-section of the core material is transferred to the CoFeB shell of the nanotube, as is apparent from the facets showing in the images. For all configurations we denote the alignment of the hexagonal perimeters to be as shown in figure 3.6: facets face the adherend surface. The spherical structure in the upper inset is the CoFeB-covered Ga catalyst particle. In the lower inset the cleaved edge of the GaAs template is visible underneath the shell material.

Demagnetization factors and net anisotropy are calculated for the dimensions found for the hexagonal CoFeB nanotubes. The cross-section of the nanotubes is not always a regular hexagon, as can be seen from the measured dimensions (appendix B.2). This may be due to directional coverage during sputter deposition of the CoFeB. Given the volume of the nanotubes, we can find the average facet size of a regular hexagonal nanotube with the same volume and shell thickness. From there we can calculate the expected demagnetization factors of CoFeB nanotubes in the three basic configurations as carried out in appendix A.2:

	$D_x$	$D_y \equiv D_{\perp}$	$D_z \equiv D_{\parallel}$	$(D_{\perp} - D_{\parallel})$
C1	0.596	0.645	0.002	0.643
C2	0.645	0.002	0.597	-0.595
C3	0.002	0.644	0.597	0.047

Table 4.2. | Demagnetization factors  $D_x$ ,  $D_y$ , and  $D_z$ , and the net anisotropy  $(D_{\perp} - D_{\parallel})$  calculated for the three CoFeB nanotubes of the three basic configurations.

## 4.4. Sample Fabrication

### 4.4.1. Introduction

Each individual nanotube we investigate is affixed to the tip of an ultrasoft cantilever in one of the three basic configurations [1], [2], and [3] shown in figure 4.8. To characterize the full sample anisotropy, three configurations are necessary. With each configuration we probe the net anisotropy of one principal axes of the magnetic sample. In agreement with the coordinates of figure 3.2, in figure 4.8 all configurations are depicted. In the upper row, the oscillation angle (yellow) of the cantilever is sketched together with the focused laser light (white) used to detect the motion of the cantilever<sup>a</sup>. The lower row shows details on the alignment of each sample with respect to the cantilever.

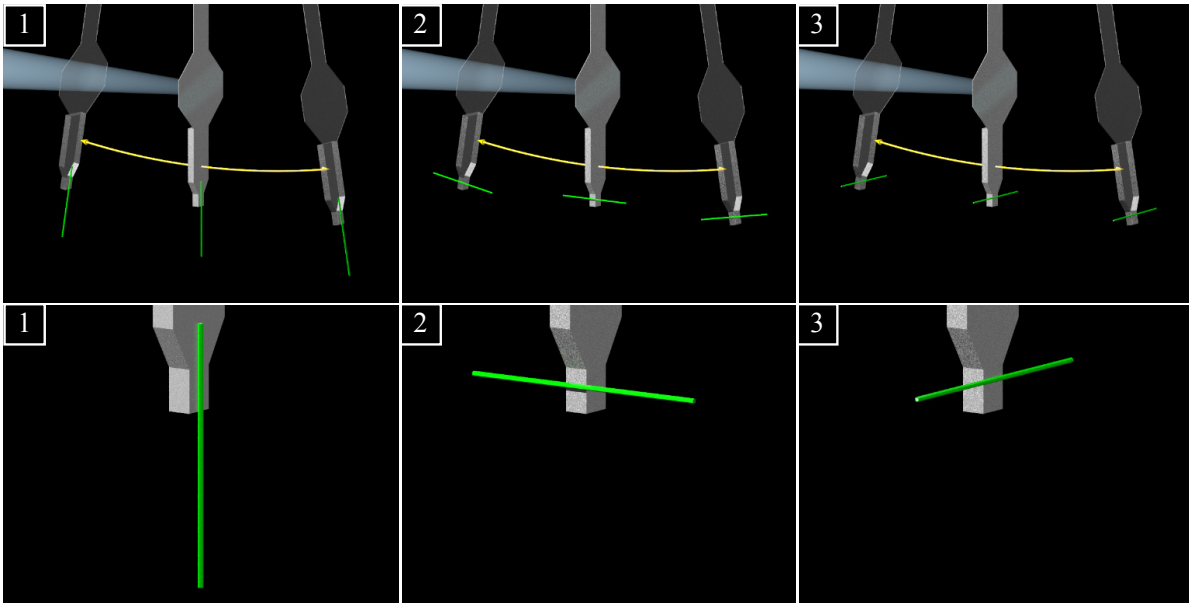


Figure 4.8. | Schematic diagram of the three sample-on-cantilever configurations. Upper row: The oscillation angle (yellow) of the cantilever is depicted together with the focused laser light (white) used to detect the motion of the cantilever. Lower Row: Details on the alignment of each sample with respect to the cantilever. Diagram is to scale, deflection exaggerated for clarity.

The growth of the Ni and CoFeB nanotubes is described in sections 4.3.2 and 4.3.3, respectively, as realized by collaborators. To fabricate the sample-on-cantilever system, individual

nanotubes are chosen from their substrate under an optical microscope, shown in figure 4.9a and glued to the cantilever using a micro-manipulator setup. The method was introduced by Fei Xue<sup>f</sup>, and has been further developed significantly since.

#### 4.4.2. Standard Procedure

As a tool to handle the nanotubes we use self-made glass needles, which are pulled from solid glass rods with the help of a two-step weight-controlled puller (Narishige PC-10). Heaters of the puller are set to about 65 %, pulling distance is 6 mm, using all weights. We achieve cone-shaped needle tips with tip diameters below 2  $\mu\text{m}$ , see e.g. figure 4.9b. The needles are controlled by precision hydraulic micro-manipulators (Narishige MMO-202ND, see in 4.9a, one on each side). During manipulation electrostatic charging can be avoided by putting a weak radioactive  $\alpha$ -source within centimeters to the working area.

Following the optical microscopic images of figure 4.9b–k (magnification  $\times 25$  and  $\times 400$ ), fabrication starts by preparing a cantilever with epoxy glue (Gatan G1): The glue is prepared by mixing five parts of the epoxy resin with one part hardener on a glass slide. Then a glass needle is dipped into the ready glue (figure 4.9b), such that a certain amount is picked up and held by the needle (figure 4.9c). For the preparation of configuration [2](#) the cantilever is put on its side, see figure 4.9d. Touching the cantilever tip with the drop of glue will deposit less than 100 fL. Minimal use of glue prevents diffusion from the tip towards larger surfaces of the cantilever.

With a new needle, an individual nanotube is chosen from the substrate surface, figure 4.9e. A small electrostatic charging here is welcome, since it will help to keep the nanotube at the needle during transfer. With the glass needle carrying the nanotube we approach the cantilever (figure 4.9f) and a second needle is used to adjust cantilever and nanotube alignment (figure 4.9f–h). A remainder drop of glue is visible on the right glass needle in figure 4.9h, which may well be glue which has already been deposited on the tip of the cantilever. Owing to the unfortunate tendency of the glue to float towards larger surfaces, one has to take special care to leave a little amount of glue behind on the cantilever tip.

After making contact between cantilever and nanotube (figure 4.9i), one needle after the other is released off the nanotube (figure 4.9i–k). This can be problematic due to alternating adhesion between the two needles and the nanotube. Combining deliberate deflection of the cantilever with valiant vibration will eventually leave the nanotube affixed to the cantilever. Time can also help (and hurt) the process for both glueing and nanotube attachment: Constant touch of two components over a few minutes seems to increase the likelihood of a solid contact.

Finally, the glue needs to cure approximately one day in ambient conditions, but in a undisturbed environment: Until final cure, vibrations may well alter the alignment of nanotube and cantilever unwillingly. Also, it is not advised to leave the sample in the focused light of the optical microscope, since—depending on the specific sample—it will damage the nanotube.

---

<sup>f</sup>High Magnetic Field Laboratory (HMFL), Anhui Institute of Optics and Fine Mechanics, Hefei Institutes of Physical Science, Chinese Academy of Sciences (CAS), Hefei 230031, China.

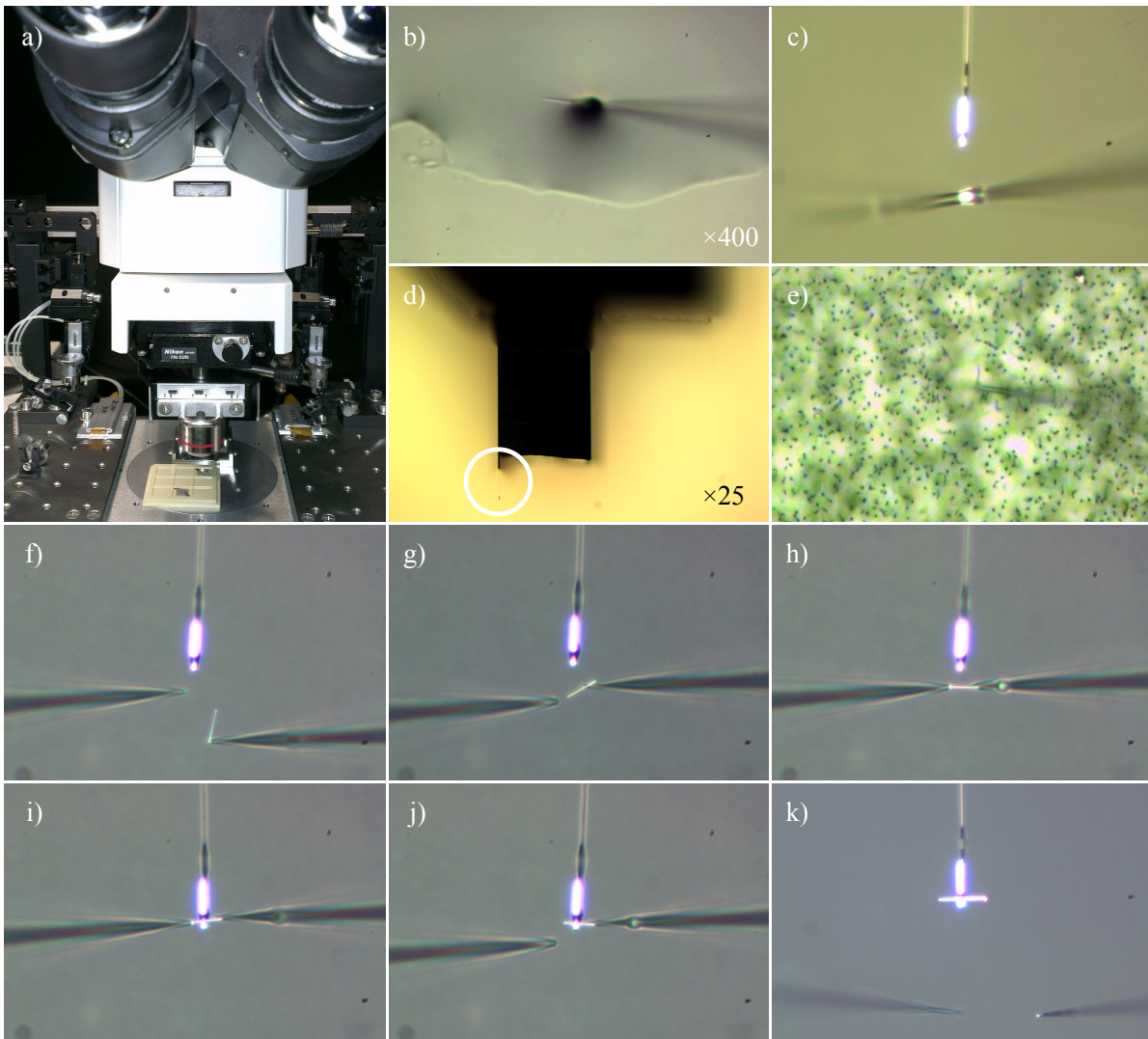


Figure 4.9. | Optical image of the optical microscope (a) and optical microscopic images of the sample fabrication procedure (b–k). Magnification is approximately  $\times 400$ , except for (d),  $\times 25$ .

## 4.5. Variations on Sample Fabrication

### 4.5.1. Introduction

The attachment of a sample to the tip of a cantilever is a basic technique for many experiments. In the context of magnetometry these samples may be magnetic nanotubes, as described in [22, 50], and in this thesis. A similar experimental setup has been used to perform magnetic resonance force microscopy (MRFM) measurements on viruses [11], drops of polystyrene [77], nanometer-sized GaAs particles [85], and nanowires containing phosphor [86]. Depending on the general state of the sample matter, different attachment procedures may prove useful.

#### 4.5.2. Dual Beam Microscopy and Nano-Manipulation

The utilization of optical microscopy and hydraulic manipulators allows the handling of nanometer-scale samples, as shown in section 4.4.2, but not so much the manual structuring of these objects. Focused electron and ion beam microscopy and electro-mechanical manipulators allow full access to the nanometer-scale, up to the point of precision positioning and construction of sample-on-cantilever systems.

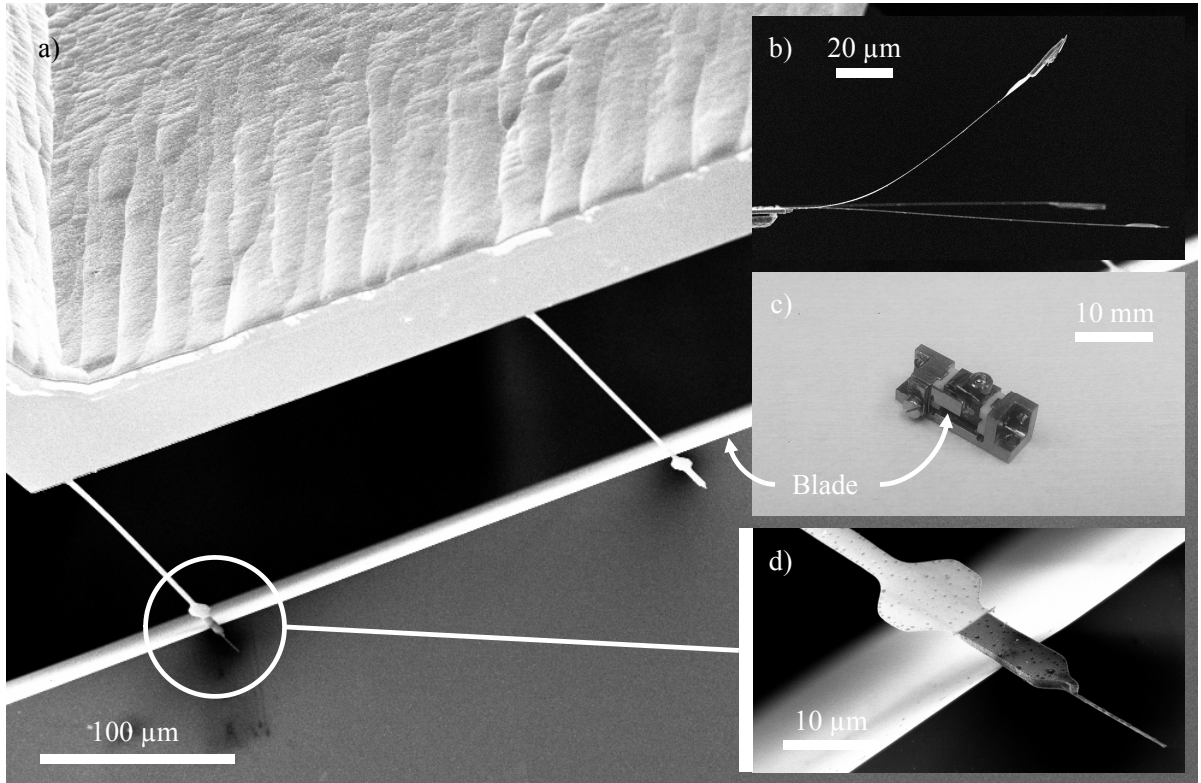


Figure 4.10. | Collection of SEM and optical images explaining the use of the cantilever Mini Blade Holder. Further commentary in section 4.5.2.

If an ultrasoft cantilever as in figure 4.10 is subject to a focused electron beam in a SEM or a focused ion beam (FIB), the impact of the particles will induce oscillation of the cantilever leading to blurred images, or—much worse—to (ion) particle implantation in the cantilever shaft. The latter will result in serious damage to the cantilever up to total loss, see figure 4.10b: Even short exposure can lead to the permanent bending of the cantilever and a reduction of its quality factor. Both to stabilize the cantilever mechanically and to shield it from ion beams, we introduce the “Mini Blade Holder” (by Fei Xue<sup>f</sup>) in figure 4.10c. Figure 4.10a shows how the cantilevers held by a Si chip each sit on a sub-nanometer sharp SiN blade. The detail in figure 4.10d reveals the nanotube sample N1 during characterization after the DCM measurements.

For the preparation of the GaAs sample investigated by Xue et al. [85], the majority of the fabrication procedure is done inside a dual beam microscope, combining a SEM with a FIB. The device includes an electro-mechanical nano-manipulator, which is seen in figure 4.11a,



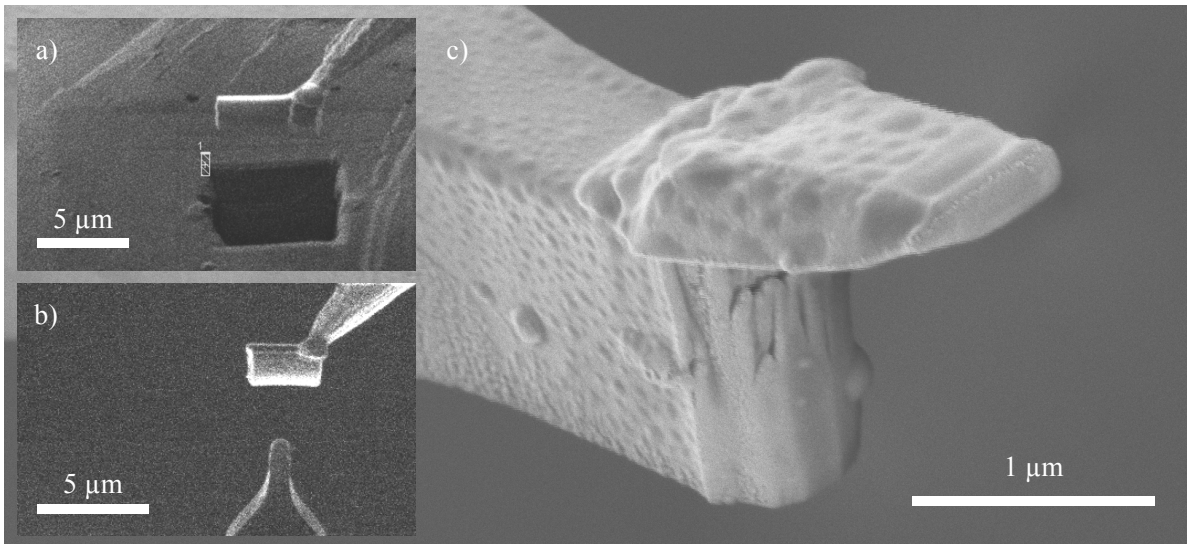


Figure 4.11. | Collection of SEM and FIB images explaining FIB-based methods of fabrication. Further commentary in section 4.5.2.

holding a slab of bulk GaAs material, which has just been milled by the FIB from a larger GaAs substrate. A thin layer of platinum is deposited on top of the slab to protect it from potential ion damage during the milling. In figure 4.11b the manipulator approaches the cantilever from “below” as compared to figure 4.10a,d, such that the ion beam is shielded from the cantilever shaft. Both figures 4.11e,f are micrographs taken with the FIB in imaging mode. The sample piece then is Pt-welded to the cantilever tip and cut to its final dimensions  $2.4\ \mu\text{m} \times 0.8\ \mu\text{m} \times 0.3\ \mu\text{m}$  using the FIB as a mill, the result is shown in figure 4.11c. The side of the sample which formerly was part of the GaAs substrate is oriented such that it faces away from the cantilever. A roughly 200 nm thick layer of the original Pt protection layer remains on this side of the sample particle.

### 4.5.3. Universal Sample-To-Cantilever Attachment Apparatus

For a vast variety of samples, no specialized technique exists for both handling and—much less so—attachment to a cantilever. Although following procedures pose mere suggestions they might be useful for future experiments.

In figure 4.12a we can see a device built from mostly optics experiments parts, mounted on a screw hole plate, allowing great flexibility in an attempt to find a universal sample-to-cantilever attachment apparatus. On the left is a clamp holding a glass slide, but the central part is a 3D-adjustable caliper stage. Clamped to its front, a cantilever holder facing down (bright metallic) maintains one cantilever chip. A magnified image in figure 4.12b reveals how the cantilever holder can be moved close to what is fastened in between two glass slides. Seen through an optical microscope, figure 4.12c shows a Cu grid as used as a sample holder in transmission electron microscopy (TEM). Visible on the left: the two glass slides used as a holder. On the right: a cantilever chip in an attempt to pick a T4-bacteriophage sample off the grid. As a

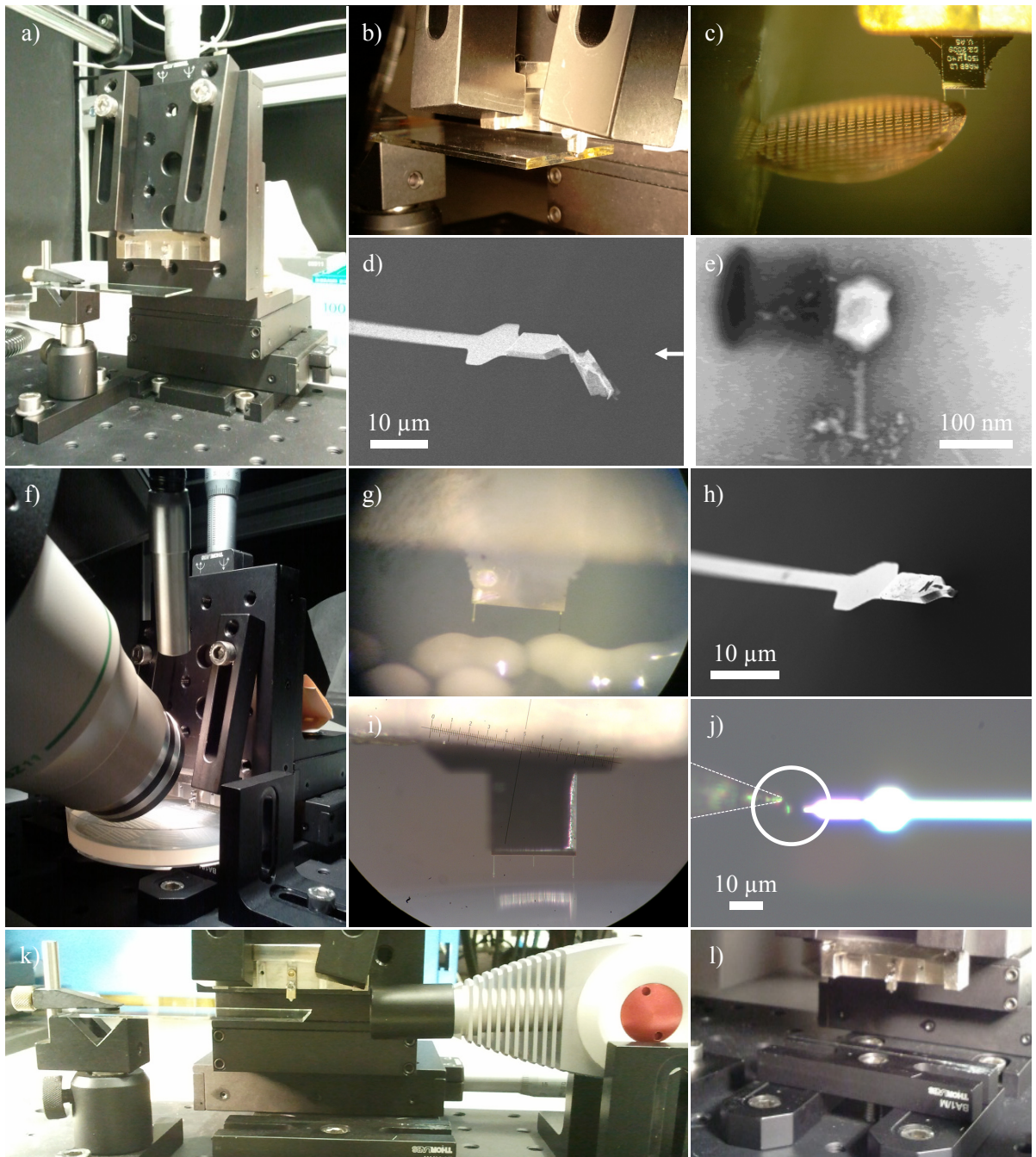


Figure 4.12. | Collection of optical, SEM, and TEM images explaining the use of the universal sample-to-cantilever attachment apparatus and results of corresponding fabrication procedures. Further commentary in section 4.5.3.

result, the nanometer-thick membrane, that is stretched within the grid, stays attached to the cantilever (figure 4.12d, SEM image). The phages are spread on that membrane (figure 4.12e, TEM image).

In figure 4.12f the optical microscope is pictured adjusted in front of the universal sample-to-cantilever attachment apparatus. In focus is a Petri dish containing a sample of *Caulobacter crescentus*, a rather large bacterium with an interesting life cycle. The magnified figure 4.12g shows a specimen colony punctured by a cantilever. In figure 4.12h we can see a cantilever with three individual bacteria attached. Although this is a nice proof of principle, the yield of the method is not yet high enough to obtain reliable results.

Figure 4.12l shows the stage which can hold different kinds of sample containers, such that also samples dissolved in liquids are accessible to the attachment procedure. In figure 4.12i the cantilever chip is reflected from the liquid, shortly before penetrating its surface. The liquid in this case also contains *Caulobacter crescentus* in a phosphoric buffer solution. With even another method involving the hydraulic micro-manipulators used in section 4.4.2, it is possible to pick a single bacterium with a glass needle (figure 4.12j). At this point the actual attachment procedure to the cantilever tip remains unclear, since glueing does not persist.

In another variation to the setup of figure 4.12a, in figure 4.12k we added a UV-light source on the right side. It may serve as illumination, or to cure a UV-light sensitive glue. A general problem to the universal sample-to-cantilever attachment apparatus is the likeliness of contamination of the cantilever with unwanted ambient substances.

## 4.6. Methods

### 4.6.1. Cryostat

DCM measurements are carried out isolated from vibrations, in a vacuum chamber with a pressure below  $10^{-6}$  mbar, at the bottom of a  $^4\text{He}$  cryostat (Janis) at 4.2 K. A superconducting NbTi/Cu magnet (Cryomagnetics) allows the application of a magnetic field  $\mu_0 H$  of up to  $\pm 6$  T parallel to the cantilever axis, i.e. along the  $\pm z$  axis of the coordinates of figure 3.2. The magnetic sample is placed in the vacuum chamber such that it is in the center of the solenoid within a homogeneous region of the generated field. The solenoid has an inner diameter of 15 cm, a height of 28 cm, and an inductance of 27.7 H, limiting the maximum sweep rate and the linearity of each sweep. We use sweep rates of about 8 mT/s. To confirm the actual applied field at any point, we use a Hall effect sensor [45] outputting a voltage proportional to the measured magnetic field.

### 4.6.2. Laser Interferometer

The motion of the cantilevers is detected by laser light focused onto a 11  $\mu\text{m}$  wide paddle near the mass-loaded end of the cantilever and reflected back into an optical fiber interferometer [65]. 100 nW of light are incident on the paddle from a temperature-tuned 1550 nm distributed feedback laser diode. The interferometer cavity is defined by the paddle single-crystal Si surface and—for reasons of enhancing the detection sensitivity [87]—a nanometer-thick Si layer

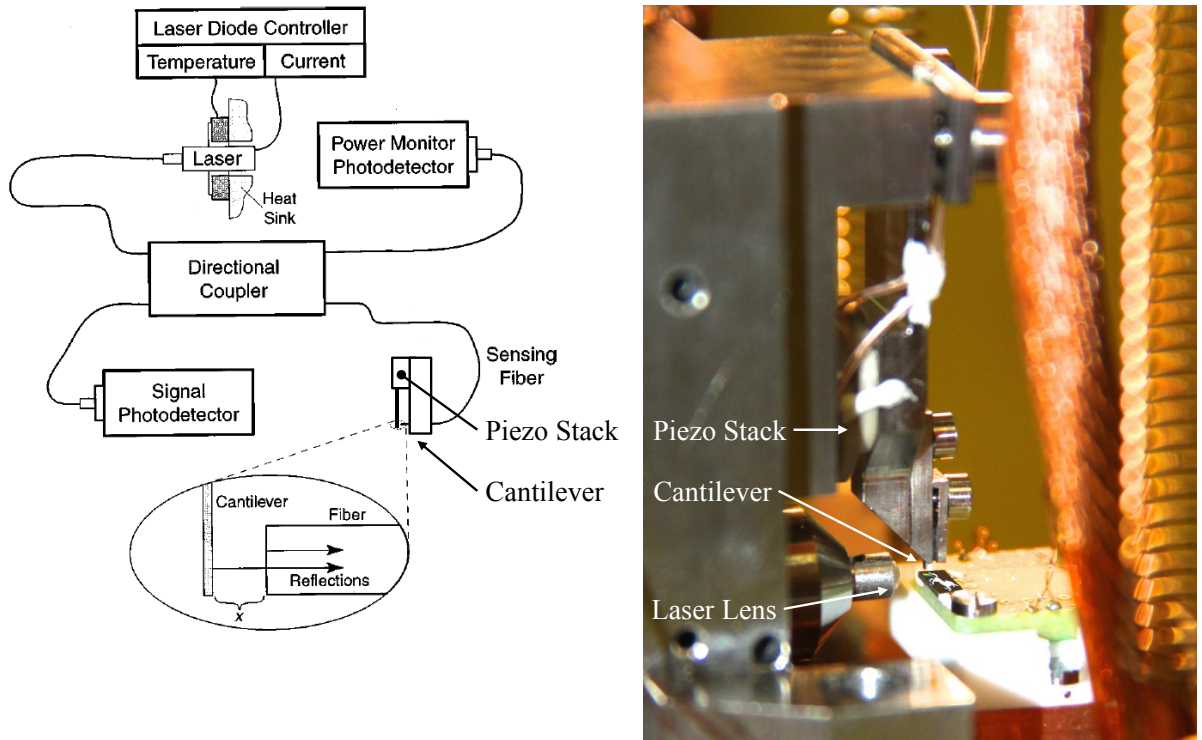


Figure 4.13. | Schematic diagram of the fiber optical laser interferometer and an optical image of the actual experimental assembly. Here,  $x$  is the length of the interferometer cavity. Diagram adapted from [88]. Our setup includes a lens within the interferometer cavity to focus the laser light from the fiber core onto the cantilever paddle and a piezoelectric element to self-oscillate the cantilever.

covering the cleaved end of the optical fiber. For adjusting the interferometer to maximum sensitivity, by tuning the temperature of the laser diode, the wavelength of the laser light can be altered. This is equivalent to, but experimentally simpler than adjusting the physical length of the interferometer cavity. Thereby we reach about 54% visibility. For details of an equivalent setup and on the adjustment procedure see [65] and [88]. Figure 4.13 (on the left) is a schematic diagram of the fiber optical laser interferometer as used in our experiments. Here,  $x$  is the length of the interferometer cavity. Diagram adapted from the original figure 1 of [88]. Our setup (optical image on the right) includes a lens within the cavity to focus the laser light from the fiber core onto the cantilever paddle, and back.

### 4.6.3. Experimental Procedure

The interferometric cantilever deflection signal is fed through a field programmable gate array circuit (FPGA, National Instruments) [87], back to a piezoelectric element which is mechanically coupled to the cantilever (figure 4.13, on the right). In this way we are able to detect the cantilever fundamental resonant frequency and self-oscillate the cantilever at that frequency and at the desired amplitude of typically  $y_{max} = 40$  nm.

Experimentally accessible quantities not only include the cantilever fundamental resonant frequency  $f_0$ , but also the spring constant  $k_0$ , the quality factor  $Q_0$ , and the dissipation  $\Gamma_0$ . The spring constant of each cantilever is determined through measurements of thermal noise spectra of the cantilevers at several temperatures, the quality factor is fit from the amplitude decay rate of a cantilever ring-down, and the dissipation can be calculated from the former, using equations (3.2).

By sweeping the applied magnetic field, we probe the applied field dependence of the resonant frequency of the cantilever. To ensure a magnetically well-defined state of the nanotube sample before we start data acquisition, we apply a field above  $\pm 1$  T to magnetize the nanotube to saturation. Sweeps are done in both directions towards positive and negative values, stepwise with different step sizes. After the applied field value is altered by one step, the resonant frequency of the cantilever is recorded at constant field, ensuring an equilibrated magnetization state. Each data point is acquired within 15 s to 60 s, depending on the applied field sweep rate, which makes it arduous to obtain a statistically adequate number of full field sweeps.

The field is swept, and the data is acquired, processed and recorded by a series of computer programs, called virtual instruments (VIs), that are subroutines of a Laboratory Virtual Instrument Engineering Workbench (LabVIEW, by National Instruments). These programs are coded and controlled via visual user interfaces.



# 5. Data and Discussion

## 5.1. Introduction

We present the data obtained by dynamic cantilever magnetometry (DCM) measurements as a result of the foregoing preparation of theoretical concepts and experimental methods. To describe our data we introduced the Stoner-Wohlfarth model in chapter 2.5. The model system is based on an ellipsoidal nanomagnet, exhibiting only shape anisotropy, which is described by the nanomagnet demagnetizing field. The magnetization within the nanomagnet is assumed to be constant at saturation and uniform in spatial dependence, allowing for coherent rotation. Even in the presence of incoherent reversal modes, the Stoner-Wohlfarth model still applies to sufficiently small magnetic particles, and to reversible changes even in larger magnetic samples, such as infinite cylinders [15]. For composed samples the model is also valid if separate particles do not interact.

Our nanometer-sized samples are in the shape of a hollow cylinder with hexagonal cross-section (“nanotubes”). Their demagnetization factors are calculated for six independent and non-interacting prisms composing a hexagonal structure. The interpretation of our data is developed along the lines of the Stoner-Wohlfarth model, complemented by recent studies of Harris [74] and Ruffer [42] in place of where our model is not able to produce such findings. However, we do not suppose the Stoner-Wohlfarth model to be valid for low values of the applied field, where we cannot assume a single-domain structure and neither coherent rotation or reversible changes are expected.

In DCM we measure the shift of the cantilever resonant frequency as a response to an applied field, relative to the resonant frequency at zero field. The data obtained for the Ni samples are qualitatively much alike the data obtained for CoFeB samples. Typical values differ by about a factor four in applied field, and a factor of two in frequency shift. Nevertheless, we identify certain features in the Ni data to supposedly depend on their surface roughness. Therefore the CoFeB nanotubes are considered the more ideal samples in the light of our model. The data presented for both Ni and CoFeB nanotubes are chosen from several runs of the experiment, however, the number of runs is not sufficient to provide statistically relevant data, due to the overall duration of a single applied field sweep. Ni data is previously published in Weber et al. [22].

We start by presenting obtained data for Ni and CoFeB nanotube DCM measurements in section 5.2, then we discuss the characteristics and features of the data in section 5.3. We suggest a model of magnetization state progression in order to give a consistent explanation of the findings of our experiments in section 5.4, and summarize in 5.5.

## 5.2. DCM Measurements

### 5.2.1. Ni High Applied Field Data

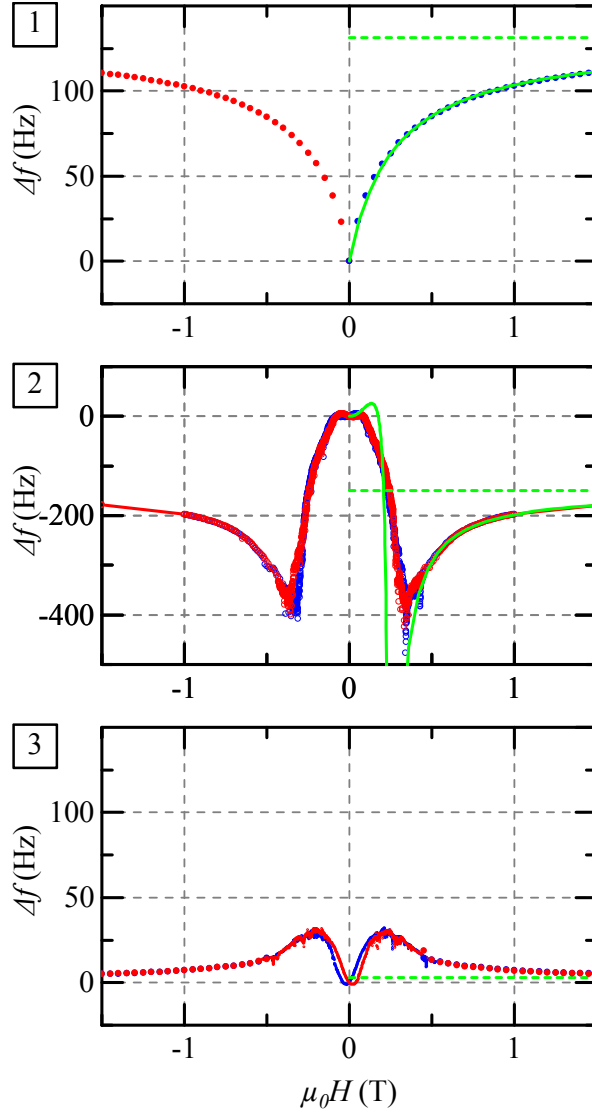


Figure 5.1. | DCM measurements and model fits of samples N1, N2, and N3 in three basic configurations for high applied fields. The frequency shift  $\Delta f$  is plotted as a function of the applied field  $\mu_0 H$ . Data points from applied field sweeps in positive direction are in red, data points from sweeps in negative direction are in blue. Green lines are model fits, green dashed lines are horizontal asymptotes.

In figure 5.1 we show DCM measurements and model fits of the samples N1, N2, and N3 in the three basic configurations for high applied fields. The frequency shift  $\Delta f$  in units of Hz is plotted as a function of the applied field  $\mu_0 H$  in units of T. During measurement, the applied field is swept from  $-6$  T to  $6$  T and vice versa, data is shown for the range of  $-1.5$  T to  $1.5$  T. Data points from applied field sweeps in positive direction are in red, whereas data points from sweeps in negative direction are in blue. Green lines are model fits, green dashed lines are



horizontal asymptotes. Fits and asymptotes are done for both positive and negative applied fields, but only shown for positive applied fields. For configuration [3] the same scale is chosen as for configuration [1] to relate the different frequency shift ranges.

The dependence of  $\Delta f$  on  $\mu_0 H$  is fundamentally different for each configuration. In configuration [1],  $\Delta f$  is positive for large  $|H|$  and approaches a constant value. In configuration [2],  $\Delta f$  becomes negative, and for large  $|H|$  eventually approaches a constant negative value. Two minima in  $\Delta f$  for each branch are observed near  $\pm 0.4$  T. Around these minima pronounced spikes are visible which in fact are not random, but reproducible in all measurement runs. In configuration [3],  $\Delta f$  is positive and goes through maxima at about  $\pm 0.2$  T, and for large  $|H|$  approaches a small positive value. Also here, in the range between  $\pm 0.1$  T to  $\pm 0.5$  T, spikes occur reproducibly throughout our measurements. From the data shown in figure 5.1, for both configurations [2] and [3] hysteresis is visible for low applied fields.

Focusing on high applied field data, according to equation (3.19), we can fit the graphs of configurations [1] and [2] to obtain values for the saturation magnetization  $M_s$  and the net anisotropy ( $D_\perp - D_\parallel$ ) of samples N1 and N2. In configuration [2] for low applied fields the third equation of (3.19) is valid. In figure 5.1 this third equation is not fit to the measured data, but plotted for the parameters fit to the high applied field data. For configuration [3] only a limit on the frequency shift can be fit, the saturation magnetization is estimated to be the average of N1 and N2. The fit in configuration [3] contains a large but unknown error due to sample-on-cantilever misalignment, see section 5.3.4. The constants in equation (3.19) are set to their measured values, see appendix B.1. Results in table 5.1:

	$\lim_{ H  \rightarrow \infty} \Delta f$ (Hz)	$\mu_0 M_s$ (T)	$(D_\perp - D_\parallel)_{\text{fit}}$	$(D_\perp - D_\parallel)_{\text{calc}}$
N1	131.5	$0.40 \pm 0.07$	$0.66 \pm 0.13$	0.64
N2	-150.0	$0.53 \pm 0.12$	$-0.46 \pm 0.13$	-0.60
N3	3.0	$0.47 \pm 0.12$	0.01	0.05

**Table 5.1.** | Fit parameters for samples N1, N2, and N3. Values for the limit on the frequency shift  $\lim \Delta f$ , the saturation magnetization  $\mu_0 M_s$ , and the net anisotropy  $(D_\perp - D_\parallel)_{\text{fit}}$  of samples N1 and N2 are extracted as fit parameters. For sample N3, only the limit can be fit, the saturation magnetization is set to the average of N1 and N2. Values of the net anisotropy are compared to their calculated values  $(D_\perp - D_\parallel)_{\text{calc}}$  of table 4.1.

### 5.2.2. Ni Low Applied Field Data

In figure 5.2 we show DCM measurements of the samples N1, N2, and N3 in the three basic configurations for low applied fields. The frequency shift  $\Delta f$  in units of Hz is plotted as a function of the applied field  $\mu_0 H$  in units of T. The graphs highlight applied field ranges of  $-30$  mT to  $30$  mT for configuration [1] and  $-120$  mT to  $120$  mT for configurations [2] and [3]. Data points from applied field sweeps in positive direction are in red, whereas data points from sweeps in negative direction are in blue. Green lines are model fits.

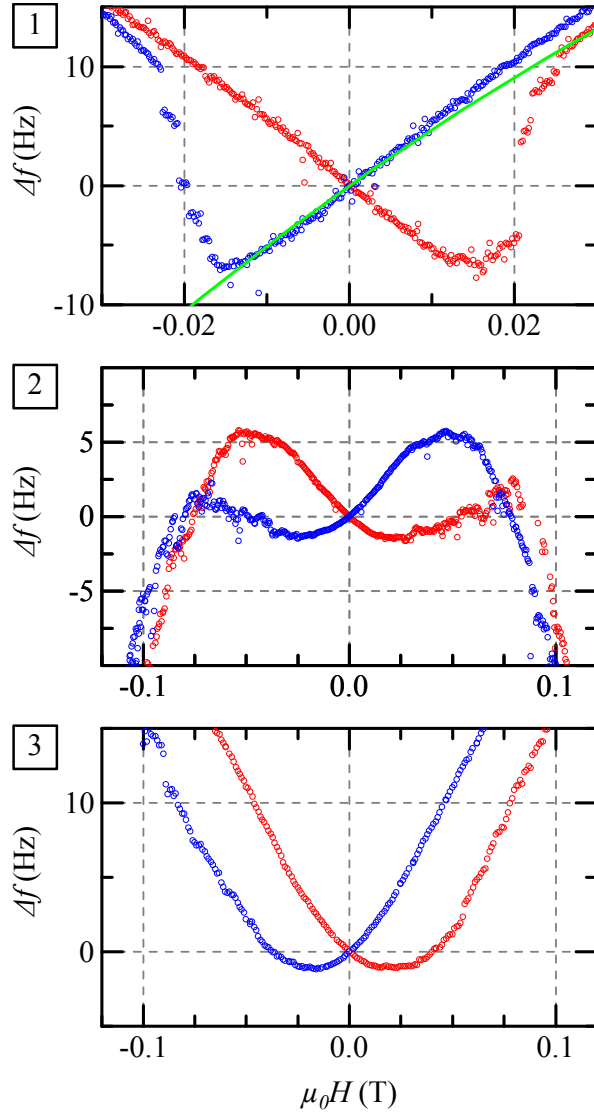


Figure 5.2. | DCM measurements of the samples N1, N2, and N3 in the three basic configurations. The frequency shift  $\Delta f$  is plotted as a function of the applied field  $\mu_0 H$ . The graphs highlight low applied field ranges. Data points from applied field sweeps in positive direction are in red, data points from sweeps in negative direction are in blue, green lines are model fits.

At low applied fields the data of *all* configurations show clear hysteresis. All graphs show sign changes of the frequency shift at least twice, of which one happens exactly at zero field. The data of configuration [1](#) exhibits jumps in frequency shift through a series of discrete steps. These steps occur in all measurement runs of this configuration at similar fields, but not equal in distribution and height in terms of frequency. Usually two to six steps can be observed in applied field ranges between  $\pm 15$  mT to  $\pm 25$  mT. In configuration [1](#), we observe a minimum in frequency shift near  $\pm 15$  mT. For fields higher than  $\pm 24$  mT (i.e. after the jumps), the difference in frequency shift between the red and blue branch is negligible. Hysteretic behavior is apparent in configuration [2](#) from a maximum in frequency shift near  $\mp 50$  mT (red/blue branch, respectively). Similarly, configuration [3](#) has a minimum at  $\pm 20$  mT (red/blue branch,

respectively). Note, that apparent gaps in the data of configurations [2] and [3] are not due to jumps, but to bad data points.

### 5.2.3. CoFeB High Applied Field Data

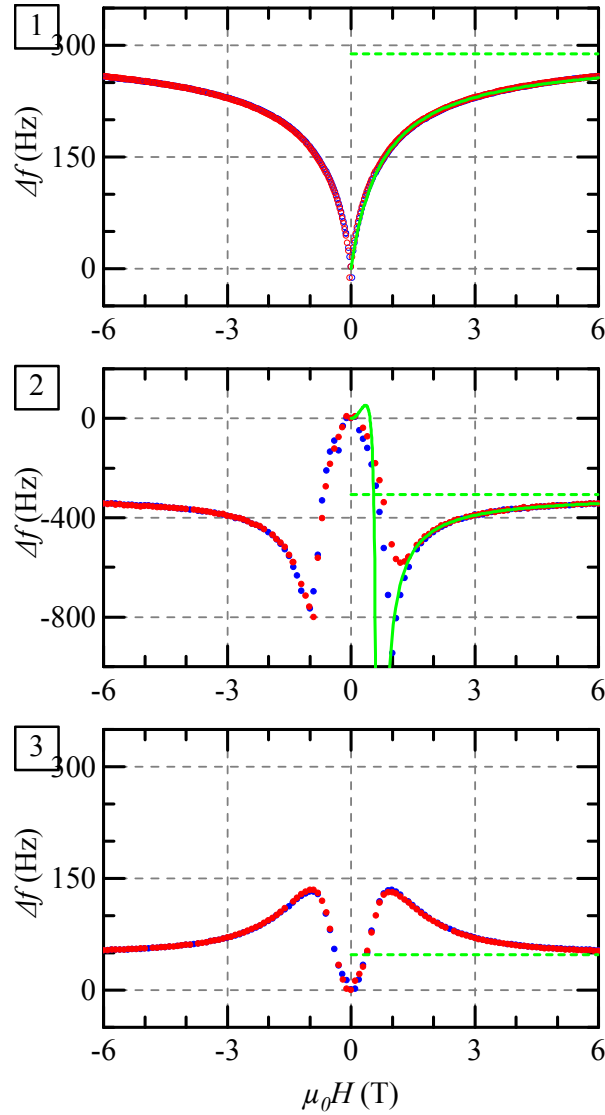


Figure 5.3. | DCM measurements and model fits of samples C1, C2, and C3 in three basic configurations for high applied fields. The frequency shift  $\Delta f$  is plotted as a function of the applied field  $\mu_0 H$ . Data points from applied field sweeps in positive direction are in red, whereas data points from sweeps in negative direction are in blue. Green lines are model fits, green dashed lines are horizontal asymptotes.

In figure 5.3 we show DCM measurements and model fits of the samples C1, C2, and C3 in the three basic configurations for high applied fields. The frequency shift  $\Delta f$  in units of Hz is plotted as a function of the applied field  $\mu_0 H$  in units of T. Data is shown for the range of  $-6$  T to  $6$  T. Data points from applied field sweeps in positive direction are in red, whereas data points from sweeps in negative direction are in blue. Green lines are model fits, green

dashed lines are horizontal asymptotes. Fits and asymptotes are done for both positive and negative applied fields, but only shown for positive applied fields. For configuration [3] the same scale is chosen as for configuration [1] to relate the different frequency shift ranges.

The dependence of  $\Delta f$  on  $\mu_0 H$  follows the description of what is written for the Ni data, except for scaling of about a factor of two in frequency and a factor of four in applied field: In configuration [1],  $\Delta f$  is positive for large  $|H|$  and approaches a constant value. In configuration [2],  $\Delta f$  becomes negative, and for large  $|H|$  eventually approaches a constant negative value. Two minima in  $\Delta f$  for each branch are observed near  $\pm 1.1$  T. In configuration [3],  $\Delta f$  is positive and goes through maxima at about  $\pm 0.9$  T, and for large  $|H|$  approaches a small positive value.

Focusing on high applied field data, according to equation (3.19), we can fit the graphs of configurations [1] and [2] to obtain values for the saturation magnetization  $M_s$  and the net anisotropy ( $D_\perp - D_\parallel$ ) of samples C1 and C2. In configuration [2] for low applied fields the third equation of (3.19) is valid. In figure 5.3 this third equation is not fit to the measured data, but plotted for the parameters fit to the high applied field data. For configuration [3] only a limit on the frequency shift can be fit, the saturation magnetization is estimated to be the average of C1 and C2. The fit in configuration [3] contains a large but unknown error due to sample-on-cantilever misalignment, see section 5.3.4. The constants in equation (3.19) are set to their measured values, see appendix B.2. Results in table 5.2:

	$\lim_{ H  \rightarrow \infty} \Delta f$ (Hz)	$\mu_0 M_s$ (T)	$(D_\perp - D_\parallel)_{\text{fit}}$	$(D_\perp - D_\parallel)_{\text{calc}}$
C1	288.0	$1.12 \pm 0.02$	$0.67 \pm 0.02$	0.64
C2	-305.2	$1.07 \pm 0.02$	$-0.62 \pm 0.02$	-0.59
C3	46.9	$1.09 \pm 0.03$	0.10	0.05

Table 5.2. | Fit parameters for samples C1, C2, and C3. Values for the limit on the frequency shift  $\lim \Delta f$ , the saturation magnetization  $\mu_0 M_s$ , and the net anisotropy  $(D_\perp - D_\parallel)_{\text{fit}}$  of samples C1 and C2 are extracted as fit parameters. For sample C3, only the limit can be fit, the saturation magnetization is set to the average of C1 and C2. Values of the net anisotropy are compared to their calculated values  $(D_\perp - D_\parallel)_{\text{calc}}$  of table 4.2.

#### 5.2.4. CoFeB Low Applied Field Data

In figure 5.4 we show DCM measurements of the samples C1, C2, and C3 in the three basic configurations for low applied fields. The frequency shift  $\Delta f$  in units of Hz is plotted as a function of the applied field  $\mu_0 H$  in units of T. On the left, the graphs highlight applied field ranges of  $-50$  mT to  $50$  mT for configuration [1] (figure 5.4a) and  $-500$  mT to  $500$  mT for configurations [2] and [3] (figures 5.4b-d). On the right hand side, for clarity, graphs for a medium applied field range are added: For configurations [2] and [3] we show data in the range of  $-1.5$  T to  $1.5$  T (figures 5.4e-g). Data points from applied field sweeps in positive direction are in red, whereas data points from sweeps in negative direction are in blue. Green lines are model fits.

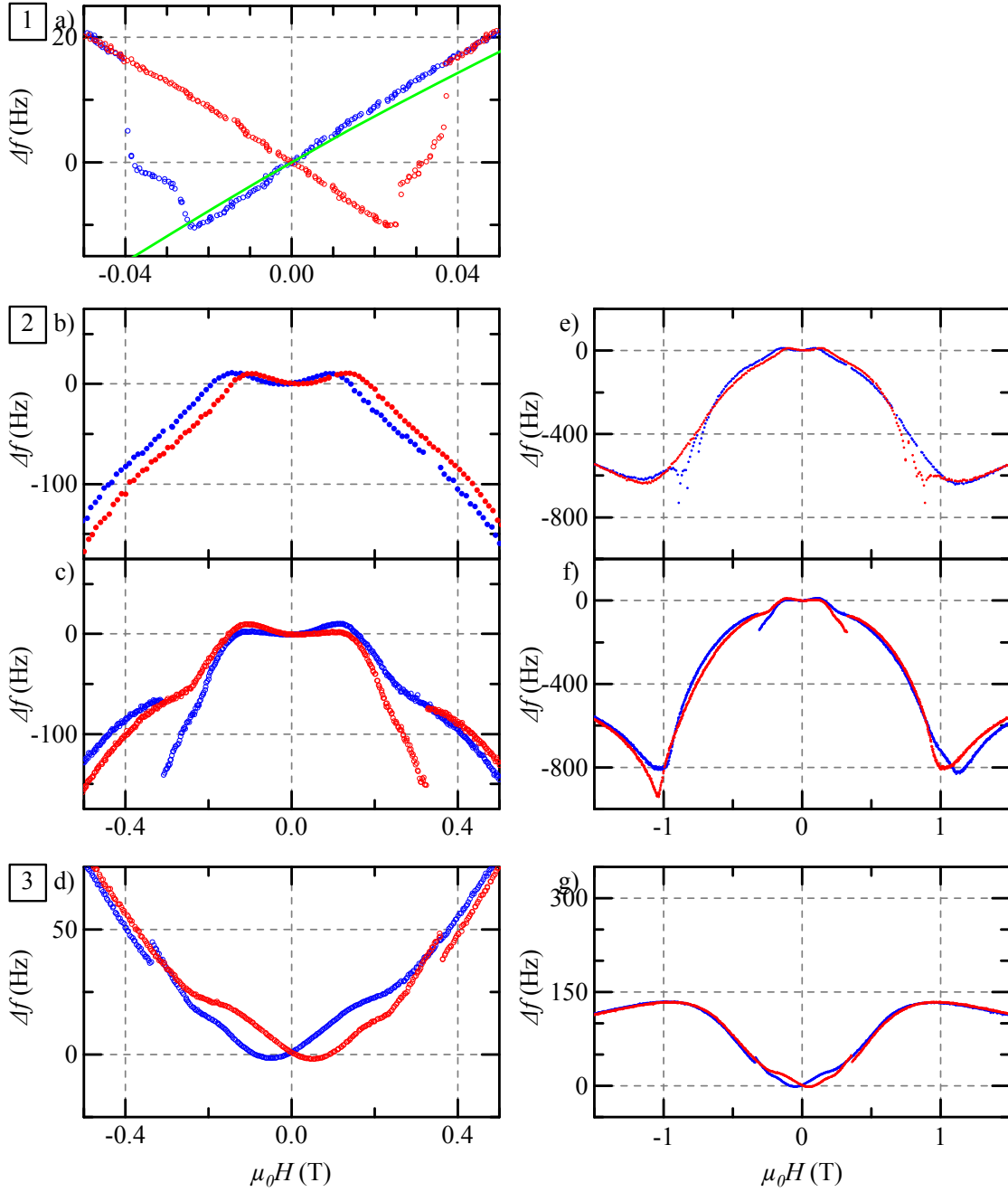


Figure 5.4. | DCM measurements of the samples C1, C2, and C3 in the three basic configurations. The frequency shift  $\Delta f$  is plotted as a function of the applied field  $\mu_0 H$ . On the left (a–d), the graphs highlight low applied field ranges, on the right hand side (e–g), for clarity, graphs for a medium applied field range are added. We distinguish a jump-case (c,f) from a no-jump-case (b,e) in configuration [2](#). Data points from applied field sweeps in positive direction are in red, whereas data points from sweeps in negative direction are in blue. Green lines are model fits.

Statements made for Ni data, accordingly also hold here: At low applied fields the data of *all* configurations show clear hysteresis. All graphs show sign changes of the frequency shift at least twice, of which one happens exactly at zero field.

The data of configuration [1] exhibits jumps in frequency shift through discrete steps. These steps occur in all measurements of this configuration at similar fields, but not equal in distribution and height in terms of frequency. Usually two steps encompassing an intermittent smooth progression can be observed in an applied field range of about  $\pm 25$  mT to  $\pm 45$  mT. In configuration [1], we observe a minimum in frequency shift near  $\pm 25$  mT. For fields higher than  $\pm 39$  mT (i.e. after the jumps), the difference in frequency shift between the red and blue branch is practically zero. The fit of high applied field data still holds for low applied fields.

In contrast to the data obtained for Ni sample N2, we discover a divided behavior of sample C2 in configuration [2]. Both a jump in frequency shift around  $\pm 320$  mT (figure 5.4c,f), and a smooth transition (figure 5.4b,e) together with the appearance of spikes around  $\pm 740$  mT to  $\pm 890$  mT can be observed, where the former case is seen to occur more often. Hysteretic behavior is apparent in configuration [2] from one maximum in frequency shift per sweep direction in the jump-case near  $\mp 100$  mT (red/blue branch, respectively). In the no-jump-case only a small hysteresis is visible, together with two rather symmetric maxima also near  $\pm 100$  mT. Note, an apparent gap in figure 5.4b,e is not due to a jump, but to bad data points.

For sample C3 in configuration [3] we measure transition via jump only, with the jump occurring at slightly higher applied field as in configuration [2] at  $\pm 350$  mT. Configuration [3] has a minimum at  $\pm 50$  mT (red/blue branch, respectively). Both in configurations [2] and [3] we observe deviations in the frequency shift curvature around  $\pm 200$  mT.

### 5.2.5. Magnetization Curves

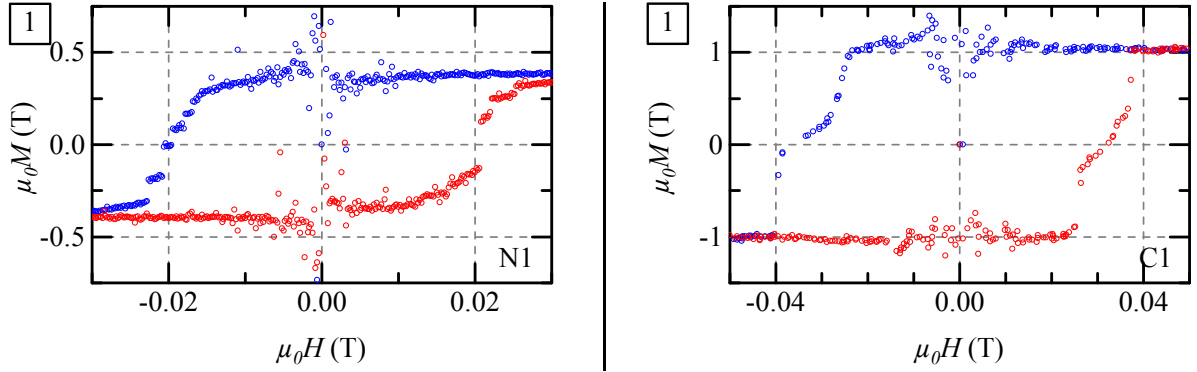


Figure 5.5. | Graphs of the magnetization  $\mu_0 M$  as a function of the applied field  $\mu_0 H$  (both in units of T) for configuration [1] of the Ni sample N1 (left hand side) and the CoFeB sample C1 (right hand side).

By the use of equation (3.21) and the fit parameters of tables 5.1 and 5.2, frequency shift data obtained in configuration [1] can be converted to a magnetization curve. In order to do so, the parameter  $M_s$  is treated as an implicit function of the applied field  $M(\Delta f(H))$ , and the measured frequency shift is used as a parameter.

Figure 5.5 shows graphs of the magnetization  $\mu_0 M$  as a function of the applied field  $\mu_0 H$  (both in units of T) for configuration [1] of the Ni sample N1 (left hand side) and the CoFeB sample

C1 (right hand side). Both magnetization curves show large spread around zero applied field, due to zero sensitivity in the frequency shift measurement at zero field, and additionally a singularity for the applied field in equation (3.21). The visible maximal magnetization under-values the fit saturation magnetization  $\mu_0 M_s^{\text{N1}} = (0.40 \pm 0.07)$  T and  $\mu_0 M_s^{\text{C1}} = (1.12 \pm 0.02)$  T slightly.

In table 5.3 the coercivities  $H_c = |M_s(D_\perp - D_\parallel)|$  for Ni and CoFeB nanotubes N1 and C1 in configuration [1](#) are listed, both from fits (figures 5.1 and 5.3) and read from frequency shift measurements (figures 5.2, 5.4, and 5.5). The fit and measured coercivities differ by a factor  $\eta$ .

	$\mu_0 H_{c,\text{fit}}$ (T)	$\eta$	$\mu_0 H_{c,\text{meas}}$ (T)
N1	0.26	11	0.024
C1	0.75	19	0.039

Table 5.3. | Coercivities for Ni and CoFeB nanotubes, both from fits and read from frequency shift measurements.

## 5.3. Discussion

### 5.3.1. Validity of Model

The model system which is described by the equations (3.19) is based on an ellipsoidal nanomagnet (sections 2.5 and 3.4), exhibiting only shape anisotropy (section 2.4.2). The magnetization within that nanomagnet is assumed to be constant at saturation and uniform in spatial dependence, allowing for coherent rotation. For composed samples the model is still valid if separate particles do not interact. The demagnetization factors are calculated for six independent and non-interacting prisms composing a nanotube with hexagonal cross-section.

For our data (figures 5.1 and 5.3) we can fit the model perfectly for high applied fields in configurations [1](#) and [2](#). For sufficiently high applied fields, certainly above 1.5 T, all requirements of the model are fulfilled: We probe nanotubes exhibiting only shape anisotropy, magnetized to saturation, and the magnetization is safely assumed to stay fixed in the direction of the applied field, thus ensuring uniformity and coherent rotation. Also for such high applied fields interaction between the six prisms, which actually are well interconnected parts of the hexagonal nanotube, is irrelevant.

For low applied fields in configuration [1](#), as can be seen in figures 5.2 and 5.4, the fit of high applied field data still holds qualitatively. From the model as described in the context of figures 2.6 and 3.3, we expect hysteresis and a sudden jump in frequency shift at coercivity. The reduced coercivity (table 5.3) is expected and explained in section 2.6.1. The assumption of more complex magnetization reversal mechanisms and/or multi-domain states may explain the occurrence of both smooth transition and discrete steps, see also section 5.3.5.

The fit for configuration [2] at low applied fields certainly is questionable. For low applied fields  $|H| < |H_c|$  the third equation of (3.19) is valid. This third equation is not fit to the measured data, but plotted for the parameters fit to the high applied field data. The magnetization cannot be assumed to be uniform at low applied fields, nor the rotation to be coherent. From the model for an ideal configuration [2] neither jumps nor hysteresis is expected. Small misalignment of the sample-on-cantilever system, i.e. non-ideal configuration alignment, together with certain low field magnetization states, may explain both observations, see also sections 5.3.4 and 5.3.5.

Although we do not provide an analytical expression for configuration [3] we assume the magnetization states and reversal mechanisms to be the same in principle as for configuration [2], because the alignment of the nanotube with respect to the applied field is equivalent to configuration [2], see figure 4.8 for instance.

In all three configurations the assumption of six non-interacting prisms composing the hexagonal nanotube may no longer hold for low applied fields. The prisms really are well interconnected such that the nanotube topology may readily cause a significant deviation from the modeled magnetization behavior.

In the light of numerical calculations including non-ideal configuration alignment [74], Ni data becomes more comprehensible than CoFeB data. This may be due to the surface imperfections of Ni nanotubes: While magnetization dynamics hoped for in nanometer-sized samples may be suppressed, the corrugated Ni surface could cause the nanotube to be in a multi-domain magnetization state (similar to figure 5.6b), thus following the modeled behavior in terms of a net magnetization. However, the CoFeB nanotube exhibiting a rather smooth surface structure may allow for unseen and non-trivial magnetization states at low applied fields.

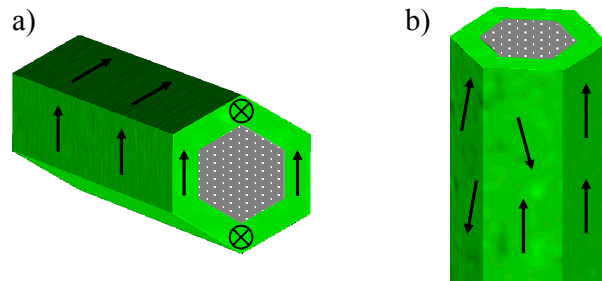


Figure 5.6. | Illustration of a possible “onion” magnetization state (a) within a nanotube, consisting of two oppositely oriented circumferential domains, and confining states in which all magnetic moments align along the easy anisotropy axis. Illustration of a possible multi-domain state (b) in configuration [1]. Black arrows symbolize microscopic magnetic moments.

Possible states include transitional domain structures, which would constrain magnetic moments within the nanotube, resulting in a positive net anisotropy. One possibility is the “onion state”, figure 5.6a. Such a transitional domain structure would then occur as a result of the applied field sweep history, and superimpose hysteresis in addition to possible configuration misalignment. Micromagnetic simulations and analytic calculations (see section 2.6.2) suggest the existence of a global vortex state, where the microscopic magnetic moments are aligned circumferentially around the perimeter of the nanotube sample [29, 33, 40, 41].



### 5.3.2. Saturation Magnetization And Net Anisotropy

From the aforementioned we conclude, that the high field fit parameters including the saturation magnetization and the net anisotropy, are systematically accurate. For the saturation magnetization we fit  $\mu_0 M_s^{\text{Ni}} = (0.47 \pm 0.12) \text{ T}$  and  $\mu_0 M_s^{\text{CoFeB}} = (1.09 \pm 0.03) \text{ T}$  in average. The value for the Ni nanotube is consistent with the one reported for bulk Ni ( $\mu_0 M_s = 0.51 \text{ T}$ , [23]), Ni thin films ( $\mu_0 M_s = 0.56 \text{ T}$ , [81]), and close to what was stated for ultrafine particles ( $\mu_0 M_s = 0.63 \text{ T}$ , [82]). This is comprehensible since the shell structure of the nanotube somewhat resembles a rolled-up thin film. Additionally, it can be challenging to determine the volume of nanometer-sized particles precisely. The fit value for the CoFeB nanotube is significantly lower than the one reported ( $\mu_0 M_s = 1.80 \text{ T}$ , [72]). This may be due to anomalies in the CoFeB amorphous structure currently under investigation [42, 83].

Comparing the calculated with the fit net anisotropies, we find excellent agreement (see tables 5.1 and 5.2), yet the fit values are slightly off the calculated values. Small misalignments from the ideal configurations [1], [2], and [3] can alter the expected frequency shift in the high field limit [74].

Notably in configuration [3], from the discussion in sections 3.4.5 and 3.4.6, we expect zero frequency shift for any applied field, and thus zero net anisotropy for ellipsoidal nanomagnets. The sheer presence of measurable frequency shift is mainly attributed to configuration misalignment [74]. The actual geometry of the nanotube is expected to play a minor role: In configuration [3] we probe the cross-section of the nanotube, which for the calculation of the net anisotropy is modeled as an ideal hexagon made of six independent rectangular prisms. From figure 4.7 one can see that the latter is a simplification of the real situation. Still, a small contribution from the probed geometry to the net anisotropy value is possible.

The net anisotropy calculated for sample N2 is still in range of the given standard deviation of the fit net anisotropy, but shows the largest deviation of all other calculated values. This deviation might be caused by a small material extrusion at one end of N2, see figure 4.5.

### 5.3.3. Magnetization Curves

DCM is a tool to probe the saturation magnetization and net anisotropy of magnetic samples. It is not a method to directly measure the magnetization as a function of the applied field. Within the assumptions of the Stoner-Wohlfarth model, for an ellipsoidal nanomagnet, one can calculate the magnetization curve in terms of the applied field from frequency shift data. Being aware of the limitations of our actual samples, we can still calculate such curves for configuration [1] by using equation (3.21).

Around zero applied field, the graphs of figure 5.5 show a large spreading, which is due to the singularity of equation (3.21) at zero applied field.

Figure 5.5 allows the determination of each coercivity, see table 5.3. The coercivities calculated from frequency shift fit parameters differ by factor  $\eta = 11$  and 19, as expected from explanation in section 2.6.1. From the magnetization curves in figure 5.5, we recognize the characteristic rectangular shape of the magnetization curves introduced in the context of figure 2.7 for configuration [1]. Assuming a small configuration misalignment, we actually might see a slightly altered shape, as shown in figure 2.7 for small angle deviations, and as a consequence, might underestimate the measured coercivity.

From the horizontal asymptotes—the high applied field data—of the magnetization curves we confirm the saturation magnetization of tables 5.1 and 5.2, noting that the visible maximal magnetization undervalues the fit saturation magnetization slightly. Assuming small misalignment of the sample-on-cantilever system for both samples in configuration [1], the fit saturation magnetization poses the upper limit to the magnetization as stated in section 2.5.5.

### 5.3.4. Hysteresis

From the model introduced in section 2.5, we calculate three solutions (3.16) to the energy minimization problem describing the optimal angle of the magnetization within the magnetic sample. Whether all three of those solutions are valid or only two, depends on the sign of the net anisotropy ( $D_{\perp} - D_{\parallel}$ ).

In case of positive anisotropy (configuration [1]), two solutions are valid for the applied field domain  $|H| < |H_c|$ , allowing for two directions of the magnetization to be energetically favorable. At coercivity, a discontinuous change (“jump”) in magnetization direction occurs, from one solutions to the other. Therefore we expect hysteresis for positive anisotropy (section 2.5.4).

In the case the net anisotropy is negative (configurations [2] and [3]), only one solution is valid at any time<sup>a</sup>, as seen in figure 2.6. The magnetization angle shifts smoothly, such that we do not expect hysteresis within the model assumptions.

We see hysteretic behavior for all samples in all configurations. Slight sample-on-cantilever misalignment, i.e. non-ideal configurations [1], [2], and [3], is shown to give rise to hysteresis: Early investigation on magnetic samples in the shape of prolate ellipsoids by Stoner and Wohlfarth [20] show how the transition in alignment of what we call configuration [2] to configuration [1] changes the magnetization curve from being diagonal to rectangular, see figure 2.7.

More recent numerical calculations by Harris [74] lead to the same answer considering the frequency shift in DCM for arbitrary configurations and a three-dimensional magnetization vector. Due to the nature of these calculations their results are unsuitable to fit our data. By assuming approximately ideal configurations and solving special cases in section 3.4.3 we still can illuminate the general magnetization behavior of our samples.

---

<sup>a</sup>Neglecting the infinite number of solutions due to the  $\pi$ -periodic symmetry of the physical system.

### 5.3.5. Discontinuities In Frequency Shift

If we interpret jumps as a signature of positive anisotropy as in configuration [1], non-ideal sample-on-cantilever alignment can give reason to the jumps observed in configurations [2] and [3]. Certain magnetization state predispositions may occur statistically, which especially for very slight sample-on-cantilever misalignment may lead to different applied field ranges for the discontinuities to appear, as observed for sample C2.

For Ni sample N1, in configuration [1], the assumption of more than one magnetic domain explains the occurrence of discrete steps instead of one jump upon magnetization reversal. We expect a rather simple domain structure from the corrugated surface structure of that sample, maybe similar to figure 5.6b. Magnetization reversal in these domains may lead to steps in frequency shift. The statistical nature of domain formation and magnetization reversal may be the reason for the irregularity of the steps in terms of applied field value and frequency shift.

In Buchter et al. [50], the nature of jumps in frequency shift for the same sample have been further investigated. By simultaneous detection of excitations in the cantilever displacement and jumps in frequency shift during continuous applied field sweeps the mechanical response of magnetization reversal is revealed. Moreover, by applying both spatially sensitive nanoSQUID-magnetometry and integral DCM, one can connect the occurrence of jumps in frequency shift with localized magnetization reversal (supplementary material of [50]).

The surface structure of CoFeB sample C1 is much more well defined. The intermittent smooth transition in frequency shift in figure 5.4a can be seen in several measurements, and may be due to actual magnetization rotation, initiated and followed by a discontinuous change. Magnetization reversal mechanisms suggested in literature include the curling mode for instance, see section 2.6.2, which might nucleate by sudden circumferential alignment of the microscopic magnetic moments in the sample, followed by a moving vortex domain wall. Especially for smooth transitions around zero frequency shift (see section 5.3.6), the existence of a global vortex state is suggested, where all magnetic moments are aligned circumferentially around the perimeter of the nanotube.

In the data taken for Ni sample N2 in configuration [2], the lack of jumps at lower field may well be due to the surface roughness of the Ni sample. Interesting microscopic magnetization states may be hidden in the multi-domain average. At higher field we observe spikes in frequency shift, see figure 5.1 and highlighted for sample N2 in figure 5.7. The spikes are not random in nature, but reproducible in many sweeps obtained for these samples.

The energy landscape as depicted in figure 2.6 is highly dependent on the structure of the nanotube. Even for an ideal sample in configuration [2], around coercivity the energy curve is rather flat with two local energy minima relatively close by, only separated by a small energy barrier. Additional corrugation might make jumping from one minimum to the other easy under small perturbation. Ni nanotubes exhibit a rather irregular surface structure, as seen in figure 4.5. A therefore corrugated energy landscape might be the reason for irregular

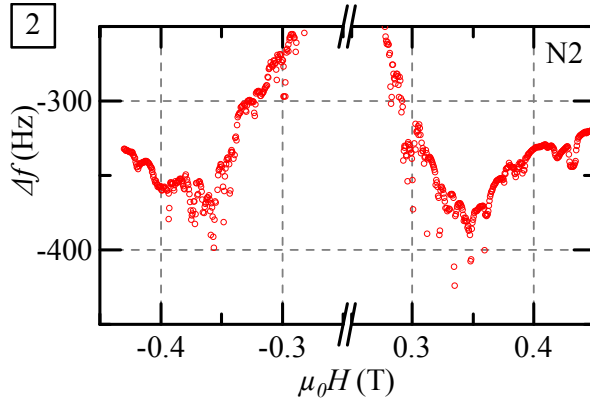


Figure 5.7. | DCM measurements of sample N2 in configuration [2](#). The frequency shift  $\Delta f$  is plotted as a function of the applied field  $\mu_0 H$ . The graph highlights applied field ranges showing reproducible spikes in the frequency shift. Only data points from applied field sweeps in positive direction are shown, in red.

magnetization states during magnetization reversal. Only when the influence of the applied field is rising, magnetization states may become more well defined.

We expect discontinuities in frequency shift as a signature of positive anisotropy in any configuration for different applied field ranges, dependent on the degree of configuration misalignment. Our observations are summarized in section 5.4 in an attempt to suggest a consistent magnetization reversal model.

### 5.3.6. Discussion Of Frequency Shift

The sign of the frequency shift determines, whether the occupied magnetization state exhibits a positive or negative anisotropy, according to the sign of the curvature of the total magnetostatic energy with respect to the cantilever deflection, see section 3.4.5. We examine applied field sweeps in positive direction for each configuration, statements apply for negative sweep direction accordingly.

In the high field limit, where the magnetization state is well defined uniformly along the applied field direction, the sign of the frequency shift tells us the configuration of the sample in question: From a positive frequency shift we know that the alignment of the magnetization is in direction of the sample easy axis, thus we look at configuration [1](#). From a negative frequency shift at high applied field, we know the sample easy axis is misaligned with the magnetization, so we consider configuration [2](#). In the case of configuration [3](#), we expect a small positive frequency shift equivalent to the alignment of the magnetization along two edges of the hexagonal cross-section of the nanotube. Sample-on-cantilever misalignment can cause changes to these high field limits.

For low applied fields the situation is more complex. In configuration [1](#) (figures 5.2 and 5.4), during the applied field sweep in positive direction, we follow the frequency shift progressing from positive values through the origin to negative values where we then observe discontinuous

changes towards positive frequency shift. Only positive anisotropy is observed for sample N1 where the magnetization always seems to point along the easy axis of the nanotube, differently from for sample C1 where we see a smooth transition between the steps (figure 5.4a): If we assume the initial jump to be the onset of magnetization reversal, we may observe the signature of the reversal mode in the smooth transition around zero frequency shift. In an energy picture, the smooth transition from negative frequency shift to positive, is a transition from an unfavorable energy maximum to a favorable minimum. In case of transversal net magnetization rotation, zero frequency shift stands for an intermediate angle of the net magnetization between easy and hard axis of the sample. Micromagnetic simulations and analytic calculations (see section 2.6.2) suggest magnetization reversal via curling and moving vortex domain walls as reversal mechanism, including but not limited to a global vortex state, which would show zero net magnetization by aligning the microscopic magnetic moments circumferentially around the perimeter of the nanotube sample.

In configuration [2], coming from negative applied field, we observe the frequency shift progressing from negative values through zero to a positive maximum at negative low field, and back through to the origin, see figures 5.1, 5.2, 5.3, and 5.4b,c,e,f. We interpret, that in the beginning the magnetization points transversal to the easy axis of the nanotube, revealing the negative anisotropy of the configuration, and then rotating towards the easy axis for increasing field, thus passing the zero frequency shift, when the net magnetization angle is intermediate, before the frequency shift is zero again as a consequence of zero applied field.

The fact that the frequency shift is “more negative” around 0.4 T for N2 (1.1 T for C2) than for the high field limit is attributed to the less strong confinement of the magnetization to the applied field direction as compared to the high field limit: Probing the alignment of magnetization and easy axis by deflecting the cantilever at very high field will leave the magnetization practically independent of the anisotropy, which is like probing a wide maximum in energy (small curvature) in terms of the deflection angle, whereas doing so at lower field will lead to a small change in angle of the magnetization as a consequence of the influence of the anisotropy, that is a narrow energy maximum (large curvature) in terms of the cantilever deflection angle. We will use a similar argument to explain the different depth of the minima around 1.1 T for C2 in the jump- and no-jump-case (see figure 5.9), after introducing certain microscopic magnetization states in section 5.4.

Frequency shift progression in configuration [2] from the origin towards positive applied field shows divided behavior, see figures 5.2, and 5.4b,c,e,f. See figure 5.8 for a comparison of jump- and no-jump-case. We will focus on the peculiarities of our samples.

The frequency shift progression of sample C2 in the no-jump-case is symmetric in the low field range, but shows spikes around +800 mT, see figure 5.9. Symmetric behavior is what we would expect from a unperturbed rotation of the net magnetization, in an ideal configuration [2], see section 3.4.5. Ambiguous change between jump- and no-jump-case is associated with certain magnetization state predispositions.

For sample C2 in the jump-case, at low field on the positive side of the origin we observe a flat of zero frequency shift, turning towards a negative shift, then a jump towards “less negative” shift, followed by mentioned high field behavior. Zero frequency shift stands for an intermediate

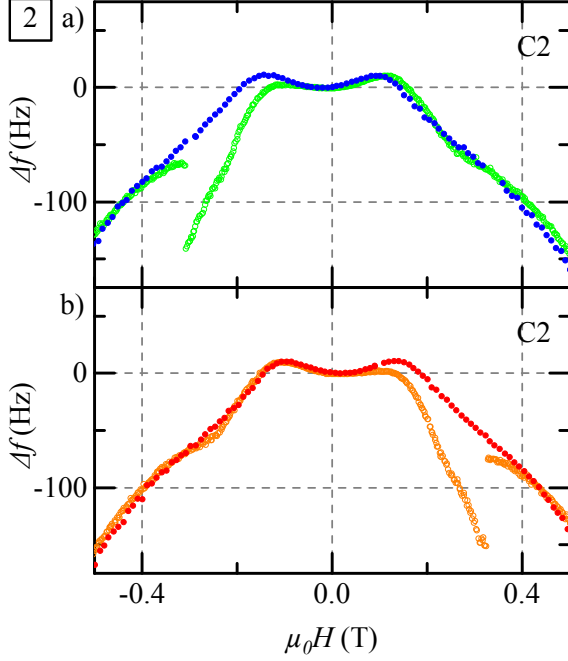


Figure 5.8. | DCM measurements of sample C2 in configuration [2](#). The frequency shift  $\Delta f$  is plotted as a function of the applied field  $\mu_0 H$ . The graph compares jump- (green, orange) and no-jump-case (blue, red) in negative (a), and positive (b) applied field sweep direction, respectively, at low applied field range.

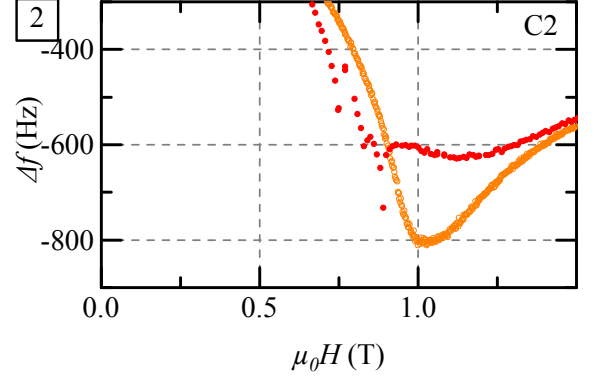


Figure 5.9. | DCM measurements of sample C2 in configuration [2](#). The frequency shift  $\Delta f$  is plotted as a function of the applied field  $\mu_0 H$ . The graph compares jump- (orange) and no-jump-case (red) in positive applied field sweep direction at medium applied field range. Spikes and minima in frequency shift are highlighted.

angle of the net magnetization between easy and hard axis of the sample, i.e. “neither minimum nor maximum” in energy, or zero net magnetization. A number of magnetization states may fulfill these criteria. Among them are curling- or vortex-mode states, or a mixture of these, and also axial states with anti-parallel alignment of the magnetic moments. These states may ultimately lead to the observed jump in frequency shift, when the increasing applied field is suddenly able to realign microscopic magnetic moments to form a more axially uniform magnetization state, thus respecting the sample easy axis and placing the net magnetization angle in a “less negative” energy maximum. Suggestions for possible transient magnetization states are summarized in section 5.4.

Apart from not showing a jump, the behavior of the Ni sample N2 is similar to the one described for sample C2 in the jump-case. Deviations may well be due to the surface roughness of the Ni sample. The Ni sample may be well described by a model involving configuration misalignment, thus expecting a jump, but interesting microscopic magnetization states may be hidden in the multi-domain average, or entirely suppressed, wherefore we see no jump.

For configuration [3](#) we observe a small positive frequency shift for high (negative) applied field, in the progress of increasing applied field towards positive values the frequency shift increases slightly, before it falls to zero at zero applied field. Frequency shift is symmetric except for a small hysteresis, jumps occur for sample C3, but not for N3. Explanations follow above

statements: Sample-on-cantilever misalignment may cause jumps in configuration [3] due to superimposed positive anisotropy, but averaging effects in N3 might hide these discontinuities. More importantly, said misalignment causes non-zero frequency shift in the first place, supposedly supported by a small positive anisotropy originated in the hexagonal cross-section of the nanotube, such that the easy axis corresponds to an alignment of the magnetization along two edges of the hexagon.

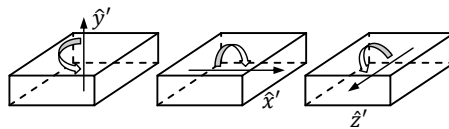
## 5.4. State Progression

In the following we summarize our observations in an attempt to suggest a magnetization state progression scheme, which—together with the phenomena illustrated before—allows for a consistent explanation of the data presented. We include recent studies of Harris [74] and Ruffer [42] in place of where our model of six independent prisms is not able to produce such findings. These studies include numerical calculations of a model similar to ours, but including configuration misalignment, and micromagnetic simulations that hint on likely nucleation sites of magnetization reversal at low applied fields at the inner corners of hexagonal nanotube samples.

The data obtained for the Ni samples are qualitatively much alike the data obtained for CoFeB samples. Nevertheless, we identify certain features in the Ni data to supposedly depend on the sample surface roughness. Therefore the CoFeB nanotubes being the more ideal samples in the light of our model are the starting point to the suggested magnetization state progression.

We begin by making certain assumptions on how magnetization rotation is prioritized within a hexagonal nanotube. Within one of the six prisms forming the nanotube (coordinates as in figure 3.5, Aharoni [75]), it is energetically decreasingly favorable for the magnetization to rotate

- A around  $\hat{y}'$ ,
- B around  $\hat{x}'$ ,
- and C around  $\hat{z}'$ ,



according to the demagnetization factors calculated in section 3.5. These rules apply to how we picture the magnetization reversal in each configuration. The sketch above is meant to illustrate the *rotation axis* of microscopic magnetic moments within one prism, the magnetization is *not* shown.

In figure 5.10 DCM measurements of the sample C1 in configuration [1] are shown for low applied fields, equivalent to figure 5.4a. The frequency shift  $\Delta f$  in units of Hz is plotted as a function of the applied field  $\mu_0 H$  in units of T, only the applied field sweep in positive direction is shown. Certain field ranges are highlighted with grey boxes. Underneath the graph these boxes are repeated to symbolize suggested magnetization states 1 to 5. The red boxes relate to the corresponding data points, since we later show figures with two sets of data. Within the red box we show symbolic pictures of the nanotube sample in configuration [1], black arrows represent microscopic magnetic moments.

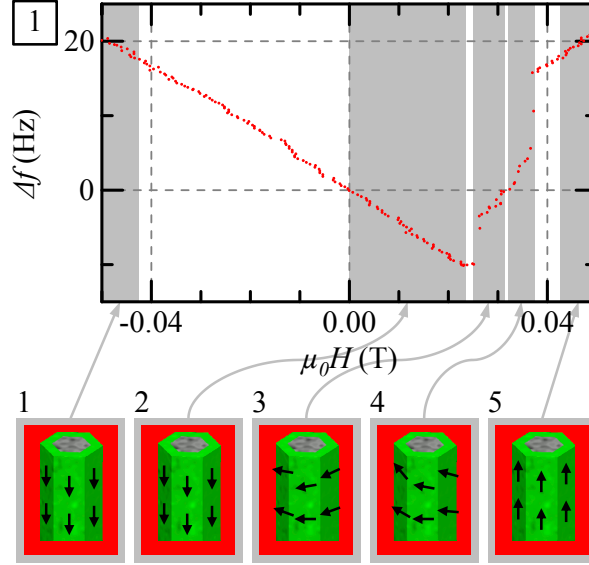


Figure 5.10. | DCM measurements of the sample C1 in configuration 1 for low applied fields. The frequency shift  $\Delta f$  is plotted as a function of the applied field  $\mu_0 H$ . Data points from applied field sweeps in positive direction are in red. Certain field ranges are highlighted with grey boxes. Underneath the graph these boxes are repeated to symbolize suggested magnetization states 1 to 5. Black arrows represent microscopic magnetic moments.

For configuration 1, in magnetization state 1, coming from high negative applied field, the magnetization is aligned uniformly along the easy axis of the nanotube. After crossing zero field, magnetization state 2 is unchanged compared to 1, but the frequency shift is negative due to different signs of applied field and magnetization direction. After the first jump, in state 3, magnetization reversal has nucleated via curling mode and changed magnetization direction discontinuously. From 3 to 4 magnetization rotation following rule A causes a smooth transition in frequency shift, possibly passing a global vortex magnetization state, until after state 4 the last jump leads again to a uniform axial magnetization state 5.

In figure 5.11 we see DCM measurements of the samples C2 and C3 in configurations 2 and 3 for medium applied fields, equivalent to figure 5.4e,f,g, respectively, with the no-jump- (orange) and the jump-case (red) depicted in one graph. At the bottom, figure 5.8b is repeated for configuration 2 and the corresponding data of figure 5.4d is added for configuration 3, magnifying the low field region. Only the applied field sweeps in positive direction are shown. Certain field ranges are highlighted with grey boxes. Between the graphs these boxes are repeated to symbolize suggested magnetization states 1 to 5. The red and orange boxes relate to corresponding data points. Within the boxes we show symbolic pictures of the nanotube samples in configurations 2 and 3, black arrows represent microscopic magnetic moment vectors. In order to exemplify the three-dimensional orientation of these vectors, in the nanotube cross-section may be drawn combined arrows which should be understood to be directed as according to their vector sum.

For configuration 2, in magnetization state 1, coming from high magnetic field, the magnetization is aligned uniformly along the hard axis of the nanotube. Towards zero field the



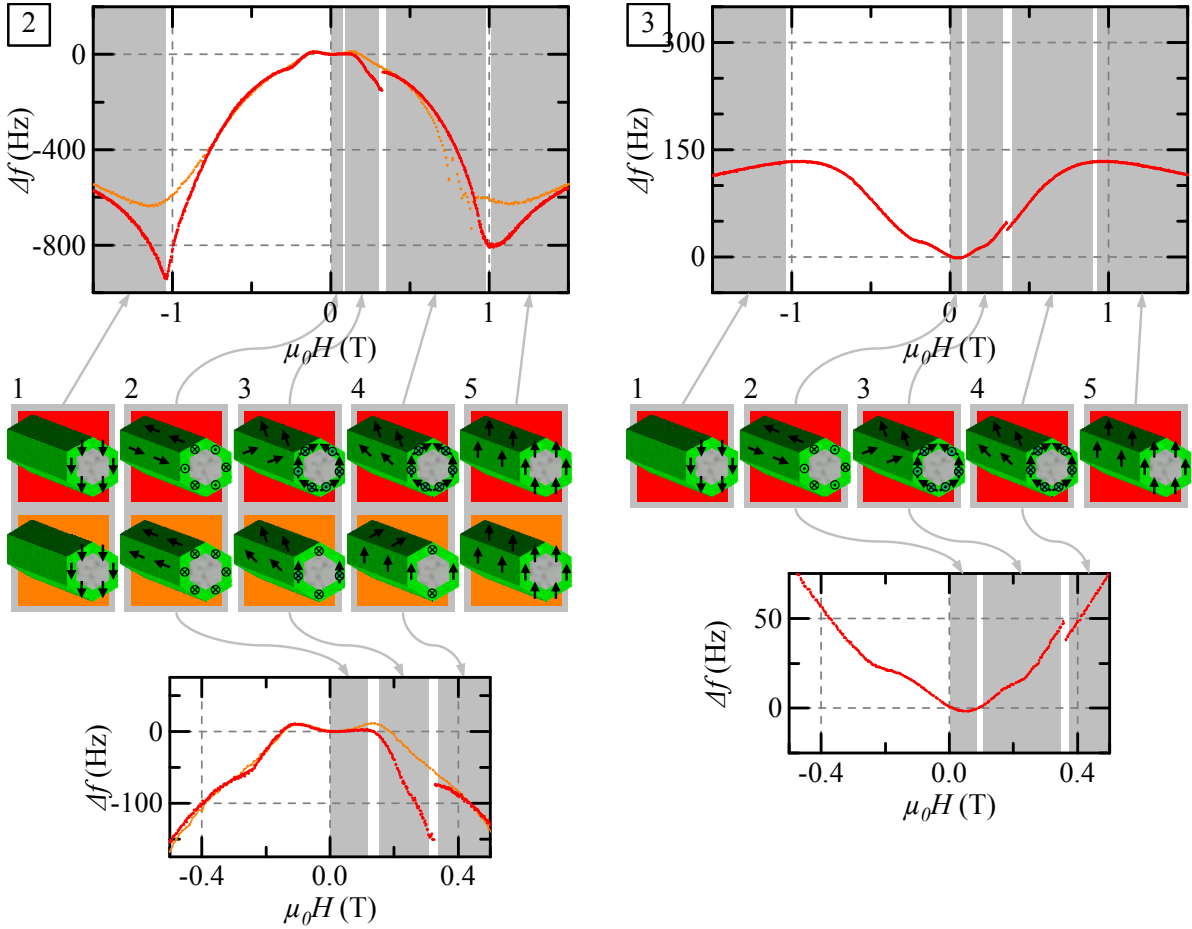


Figure 5.11. | DCM measurements of the samples C2 and C3 in configurations [2](#) and [3](#) for medium (at the top) and low applied fields (at the bottom). The frequency shift  $\Delta f$  is plotted as a function of the applied field  $\mu_0 H$ . Data points from applied field sweeps in positive direction for the no-jump-case are depicted in orange and for the jump-case in red. Certain field ranges are highlighted with grey boxes. Between the graphs these boxes are repeated to symbolize suggested magnetization states 1 to 5. Black arrows represent microscopic magnetic moments.

magnetization rotates as expected from the analytic model within each prism, first according to rule C, and then according to rule A. Deviations in the frequency shift curvature around  $-0.2$  T may be explained by magnetization rotation depending on the hexagonal structure of the sample. After crossing the zero field, we propose a divided behavior: In one case, in preparation of the jump (red data), the magnetic moments might realign to an axial anti-parallel configuration. Initiated maybe by random perturbations, state 2 (red) should be energetically favorable. In our data the process of the anti-parallel alignment of the magnetic moments may not be visible, because we have no sensitivity for  $H = 0$  T. This red state 2 then would be rather stable giving rise to the flat around zero frequency shift, i.e. the magnetic moments add up to zero net magnetization.

In the other case, when all magnetic moments stay parallel, the magnetization state 2 (orange) leads to a maximum in frequency shift due to a net magnetization favorably aligned with the easy axis of the nanotube. In a model-like behavior, these magnetic moments start rotating

towards the applied field again, as depicted in orange state 3, following rule A, leading to a sign change in frequency shift at a certain intermediate alignment of magnetization and easy axis. Supported by micromagnetic simulations, for magnetic moments situated in the edge of the hexagonal structure, the alignment to the easy axis may persist longer. The orange state 4 then evolves by rotation of the magnetization towards the applied field still following rule A, and resembles what has been mentioned as the “onion state”, consisting of two oppositely oriented circumferential domains, and confining edge states in which all magnetic moments align along the easy anisotropy axis. In late orange state 4, these confinements release in what we see as spikes in frequency shift. At this point also, we find the minimum in frequency shift, as a result of the combination of advanced alignment of magnetization and applied field, and yet significant influence of the anisotropy axis. In the final orange state 5, the magnetic moments have completely rotated towards the applied field, by a combination of rule B and C.

From the axial anti-parallel alignment (red state 2), the magnetic moments also start rotating (rule A), but the net magnetization, by vector sum, then immediately is unfavorably pointing along the hard axis (red state 3), making the frequency shift negative. This situation is only released, when a discontinuous change (jump in frequency shift) flips one half of the magnetic moments to fit the direction of the other half, resembling a somewhat tilted divided-circumferential state (red state 4). The net magnetization then points more towards easy axis direction than before, making the state energetically less unfavorable. In late red state 4 we find the minimum in frequency shift, as a result of the combination of advanced alignment of magnetization and applied field, and yet significant influence of the anisotropy axis. The minimum is deeper than in the orange no-jump-case (highlighted in figure 5.9), because the angular confinement of the net magnetization in the red state is smaller than in the onion state, such that the onion state superimposes a quasi-positive anisotropy. Speaking in terms of energy, the red state 4 poses a rather narrow maximum in energy, i.e. a high negative curvature. The magnetization state from here progresses as one would expect from the analytic model. The magnetic moments rotate towards the applied field to assume the final red state 5, in accordance to rule C.

As the reason for hysteresis and thus the occurrence of jumps in configurations [\[2\]](#) and [\[3\]](#) we propose a small configuration misalignment. For configuration [\[2\]](#) the misalignment supposedly is very small, such that by random perturbation we observe either the red jump-case, or the orange no-jump-case: In an ideal configuration [\[2\]](#) for low applied field the magnetization would rotate as expected from the analytic model. Since there is no preferred direction given by the configuration with respect to the applied field (or just a very small preference), rotation continues without discontinuous changes. The red jump-case is characteristic for configuration misalignment. When the magnetization by rotation aligns with the easy anisotropy axis of the nanotube, the applied field is small but still non-zero. With even further decreasing, ultimately zero field, the magnetic moments might realign to the energetically favorable axial anti-parallel alignment.

For configuration [\[3\]](#) we assume a larger configuration misalignment since we observe only the jump-case. The symbolic pictures of the magnetization states 1 to 5 are identical to the ones for the jump-case in configuration [\[2\]](#), and statements made for that case hold equivalently. In addition to the superposed positive anisotropy by configuration misalignment, here, we

probe the magnetization states with respect to the nanotube cross-section, such that any net magnetization alignment along the actual nanotube hard axis, now is an alignment to the easy axis of the hexagonal cross-section.

For configuration [3], in magnetization state 1, coming from high magnetic field, the magnetization is aligned uniformly along the easy axis of the nanotube cross-section. Towards zero field the magnetization rotates as expected from the analytic model within each prism, first according to rule C, and then according to rule A. Deviations in the frequency shift curvature around  $-0.2$  T may be explained by magnetization rotation depending on the hexagonal structure of the sample. After crossing the zero field, the magnetic moments might realign to an axial anti-parallel configuration (state 2) with zero net magnetization. Here, probing the alignment of the net magnetization reveals a small negative frequency shift as a consequence of possible misalignment of the magnetic moments with the easy axis of the nanotube cross-section.

From the axial anti-parallel alignment (state 2), the magnetic moments start rotating towards the applied field direction state 3 according to rule A. The net magnetization in state 3, by vector sum, then is pointing along the cross-sectional easy axis, making the frequency shift become positive. When a discontinuous change releases the axial anti-parallel alignment, one half of the magnetic moments flip to fit the direction of the other half (state 4). The net magnetization may lose little magnitude in the direction of the cross-sectional easy axis, resulting in a jump in frequency shift, marking a less favorable alignment of net magnetization and anisotropy. From here, as one would expect from the analytic model, the magnetic moments rotate towards the applied field, in accordance to rule C.

## 5.5. Findings Review

In summary, by performing DCM measurements we are able to gain insight into the microscopic magnetization behavior of Ni and CoFeB nanotube samples.

To describe our data we introduce a model system based on an ellipsoidal nanomagnet. The magnetization is assumed to be constant at saturation and uniform in spatial dependence, allowing for coherent rotation. By solving for the optimal angle of the sample magnetization for three special cases of sample-on-cantilever configuration, we can determine basic sample properties such as saturation magnetization and net anisotropy. For high applied fields we can describe the obtained data perfectly, while for low applied fields the sensitivity of the experimental method allows us to further illuminate microscopic characteristics. For the saturation magnetization we fit  $\mu_0 M_s^{\text{Ni}} = (0.47 \pm 0.12)$  T and  $\mu_0 M_s^{\text{CoFeB}} = (1.09 \pm 0.03)$  T in average.

Our nanometer-sized samples are in the shape of a hollow cylinder with hexagonal cross-section. Their demagnetization factors are calculated for six independent and non-interacting prisms composing a hexagonal structure. Comparing the calculated with the fit net anisotropy, we find excellent agreement. Depending on the orientation of the nanotube, we find net anisotropy demagnetization factors of 0.67 (sample C1) and  $-0.62$  (sample C2), numbers detailed for Ni in table 5.1 and for CoFeB in table 5.2.

In DCM we measure the shift of the cantilever resonant frequency as a response to an applied magnetic field. Each sample-on-cantilever configuration gives fundamentally different results. While the data obtained for Ni samples is qualitatively much alike the data obtained for CoFeB samples, most statements hold for both sample materials. However, Ni samples generally show features in frequency shift as a result of a rather corrugated surface structure. Similar to previous measurements of large ensembles of magnetic samples, a disordered magnetic domain structure gives an averaged picture, hiding details on microscopic magnetization states, but providing evidence for distinct multi-domain states.

CoFeB samples, in contrast, show a clean magnetic shell and therefore are considered the more ideal samples in the light of our model. Frequency shift data reveals the complex signature of potential circumferential magnetization states, and exposes magnetization reversal modes. Examples of such signature can be found in configuration [1] where a smooth transition from negative to positive frequency shift indicates magnetization reversal, maybe via curling mode and possibly including a global vortex state. In configuration [2] two cases of magnetization state progression can be observed. By comparison of different magnetization state predispositions one can potentially identify directionally confining magnetization states such as the onion state. Frequency shift plateaus at low field highlight the stability of such magnetic moment configurations.

Hysteresis found in configurations [2] and [3] and a measurable frequency shift in configuration [3] are mostly attributed to sample-on-cantilever misalignment. Complementing the original model by numerical calculations coping with said misalignment, and micromagnetic simulations that hint on likely nucleation sites of magnetization reversal helps to provide for a consistent magnetization state progression scheme to explain our data, but certain features remain unclear and will be subject to further investigation.

# 6. Conclusions

## 6.1. Summary

For the experiments presented in this thesis we employ highly sensitive dynamic cantilever magnetometry (DCM). This technique allows us to investigate the weak magnetic response of individual magnetic nanotubes without averaging over an inhomogeneous ensemble.

DCM is a tool to probe the saturation magnetization and net anisotropy of a wide range of magnetic samples and to gain insight into microscopic magnetization states and magnetization reversal mechanisms. In DCM we measure the shift of the cantilever resonant frequency as a function of both the applied field and the alignment of the sample. Applied field and sample magnetization result in a torque acting on the cantilever, adding to the mechanical restoring force, effectively stiffening or softening the cantilever, and thus shifting its resonant frequency (section 3.3).

Ferromagnetic nanotubes are particularly interesting for their magnetization states, since the low-dimensionality of these structures results in magnetic configurations not present in macroscopic magnets. These structures avoid magnetization point singularities as present in solid magnetic cylinders [28], but support core-free magnetization states, a prerequisite for fast magnetization reversal [29]. A circumferential vortex magnetization state has been reported [33] and an onion state has been suggested [40, 41], the latter consisting of two oppositely oriented circumferential domains (section 2.6.2).

The magnetic samples we are interested in are in the shape of a hollow prism with hexagonal cross-section and a high aspect ratio. Our samples exhibit a core-shell structure, using a hexagonally shaped GaAs nanowire as a core, and a grown shell of magnetically isotropic material, such that the nanotubes exhibit shape anisotropy only. Two different sets of magnetic samples are probed. One set of samples is processed to be Ni nanotubes, the other to be CoFeB nanotubes (section 4.3).

A single nanotube sample is affixed to the end of an ultrasoft cantilever in one of three basic configurations 1, 2, and 3 (figure 4.8), with the nanotube easy axis aligned along the  $z'$ -,  $y'$ -, and  $x'$ -axis (figure 2.4), respectively, to characterize the sample anisotropy. To fabricate the sample-on-cantilever system, individual nanotubes are chosen from their substrate under an optical microscope, and glued to the cantilever using a micro-manipulator setup (section 4.4). Measurements are performed in vacuum at cryogenic temperatures in the center of a superconducting solenoid.

To describe our data we introduce a model system based on an ellipsoidal nanomagnet. The magnetization within the nanomagnet is assumed to be constant at saturation and uniform in spatial dependence, allowing for coherent rotation. By minimizing the total energy of the sample-on-cantilever-system we can solve for the optimal angle of the sample magnetization for each deflection angle of the cantilever. The cantilever resonant frequency shift then is a function of the curvature of the total magnetostatic energy. We derive an expression of the frequency shift in terms of the applied field, the saturation magnetization and the demagnetization factors of the magnetic sample (section 3.4). The nanotube demagnetization factors are calculated for six independent and non-interacting prisms composing a hexagonal structure (section 3.5).

The dependence of the frequency shift on the applied field is fundamentally different for each configuration. In the special cases of configurations [1](#) and [2](#) at high applied field our data is perfectly described by our model, for configuration [3](#) we expect zero frequency shift. Hysteresis found in configurations [2](#) and [3](#) and a measurable frequency shift in configuration [3](#) are mostly attributed to sample-on-cantilever misalignment. Our model is complemented by numerical calculations coping with said misalignment [74]. For the saturation magnetization we fit  $\mu_0 M_s^{\text{Ni}} = (0.47 \pm 0.12) \text{ T}$  and  $\mu_0 M_s^{\text{CoFeB}} = (1.09 \pm 0.03) \text{ T}$  in average. Comparing the calculated with the fit net anisotropy, we find good agreement (section 5.3).

We do not suppose the model to be valid for low applied field, where we cannot assume a single-domain structure and neither coherent rotation or reversible changes are expected. Instead, low applied field data shows signature of microscopic magnetization states (section 5.2). Micromagnetic simulations on magnetization reversal [42] help to provide for a consistent magnetization state progression scheme to explain our data (section 5.4), but certain features remain unclear and left to further investigation.

While the data obtained for Ni samples is qualitatively much alike the data obtained for CoFeB samples, most statements hold for both sample materials. Typical values differ by about a factor four in applied field, and a factor of two in frequency shift. However, Ni samples generally show reproducible features in frequency shift as a result of a rather corrugated surface structure. Similar to previous measurements on large ensembles of magnetic samples, a disordered magnetic domain structure leads to averaged data [15, 22, 40]. While details on microscopic magnetization states are hidden, the data provides evidence of distinct multi-domain states.

CoFeB samples, in contrast, show a clean magnetic shell and therefore are considered the more ideal samples in the light of our model. Frequency shift data reveals the complex signature of potential circumferential magnetization states, and exposes magnetization reversal modes. Examples of such signature can be found in configuration [1](#) where a smooth transition from negative to positive frequency shift indicates magnetization reversal, maybe via curling mode and possibly including a global vortex state. In configuration [2](#) two cases of magnetization state progression can be observed. By comparison of different magnetization state predispositions one can possibly identify directionally confining magnetization states maybe similar to the onion state. Frequency shift plateaus at low field highlight the stability of such magnetic moment configurations (section 5.3).

## 6.2. Outlook

Our data provides us with most interesting insight on the existence of low applied field magnetization states, but DCM is not the ideal tool to identify and prove their microscopic magnetic moment configuration. While the obtained frequency shift data allows for drawing conclusions on net magnetization and anisotropic properties of transient magnetization states, the method lacks in actual spatial information.

One possibility to overcome this limitation is, as shown in Buchter et al. [50], the introduction of a nanometer-sized scanning superconducting quantum interference device (nanoSQUID) to the magnetometry setup. Due to its high sensitivity even small magnetization changes during magnetization reversal can be probed. NanoSQUIDs have been used to map the stray field of individual nanotubes while simultaneously probing their volume magnetization. For instance, this potentially allows the distinction of a global vortex state exhibiting vanishing stray field from other states with zero net magnetization. Additionally, spatial resolution allows for narrowing down possible magnetization nucleation sites.

Ultimately, the description of magnetic domain structure and magnetic moment configuration requires actual magnetic imaging techniques. Magnetic force microscopy (MFM) is a scanning probe technique sensitive to the gradients of the stray field. The method is capable of mapping surface domains and domain walls [41, 51–53], which may prove sufficient for our magnetic shell thicknesses, but tip-sample interaction may also influence metastable magnetization states. Another emerging high resolution scanning probe technique involves nitrogen vacancy centers (NVCs) in diamond to map magnetic dipole fields in the sub-nanometer range [54]. Additional information on the magnetization direction in surface domain structures can possibly be obtained via X-ray magnetic circular dichroism photoelectron emission microscopy (XMCD-PEEM) [34, 44], and electron holography [56]. Aforementioned methods are reviewed in section 3.2. A general concern regarding the use of said methods in view of our nanotube samples is the influence of the tubular sample structure on the interpretation of acquired data. Also, applying high enough magnetic fields can be experimentally difficult to realize in ambient conditions.

DCM is distinguished from other means of cantilever torque magnetometry by achieving a high measurement precision in counting a frequency, rather than recording a direct current signal [64]. However, the frequency shift is proportional to the applied field and thus zero at zero applied field.

In order to improve the sensitivity of our method for low applied field measurements one might employ phase-locked cantilever magnetometry (PLCM, mode 3 in section 3.2) introduced by Jang et al. [64]. PLCM involves the measurement of the resonant cantilever displacement by applying a secondary magnetic field at the cantilever resonant frequency. Superposition of the magnetic fields should leave the net magnetization unperturbed, but allows recording cantilever response even at zero applied field. The method can be further improved by adding a third solenoid in a vector magnet configuration. Thereby in principle the exact angle of the net magnetization within the nanotube can be probed.

Using our DCM method as it offers rich opportunity to investigate the magnetization and anisotropy of a wide variety of samples. Among them are nanotubes of different geometry or other magnetic materials, there is also room for improvement of existing sample types, as we can infer from our data.

We have seen the nanotube sample surface structure to have a great influence on the magnetization behavior. From a rather corrugated surface of the Ni nanotubes, deposition methods have come a long way to the fabrication of the much more ideal CoFeB sample. An even smoother surface may be achieved in another variation on sample processing, in order to optimize the sample magnetization behavior towards model predictions. From a magnetic material point of view, permalloy, a Ni-Fe-alloy, would provide for supplementary studies of the saturation magnetization for comparison to values given in literature.

The investigated samples distinguish themselves from our model especially in shell thickness and cross-section: To avoid magnetic domain formation, future samples may exhibit reduced shell thickness, which also may lead to a more conformal coating of the hexagonal core material. At the same time, further efforts can be taken in developing our model systems towards resembling actual sample structures. Numerical calculations and micromagnetic simulations mark a milestone in the attempt to find a general solution to describe our data [42, 74].

For future DCM experiments it may be interesting to characterize the magnetization behavior of circular cylinders compared to hexagonal structures, since the influence of shape anisotropy on the optimal angle of the magnetization within the magnetic sample is significant. Size-dependent properties may be investigated by probing larger tubular structures like rolled up nanomembranes [33, 35, 44], and compared to magnetic particles in the nanometer range, e.g. in the context of carbon nanotubes [61].

Apart from ferromagnets, DCM offers the capability to study other manifestations of magnetism. A rather exotic and nontrivial spin structure is represented in magnetic skyrmions and is subject to current investigation [89]. Doubly clamped mechanical oscillators have been used to test Abrikosov's supercurrent vortex theory [63, 90], and PLCM has proven useful for the study of superconducting material by attachment of annular samples to a cantilever [60], thus disclosing a whole new range of samples as well for DCM.

With this thesis we demonstrate the potential of DCM as a powerful micromagnetic toolbox. By establishing a multitude of sample-to-cantilever attachment procedures, numerous samples are made accessible to cantilever-based magnetometry. DCM is set up as a high precision method of magnetization data acquisition, while possibly interfering electro- and magneto-static fields are avoided by a purely optical readout. For data analysis and interpretation, existing model systems can be adjusted for individual sample geometry and alignment, advancing dynamic cantilever magnetometry to broaden our understanding of micrometer-scale magnetism.



## References

- [1] Richard P. Feynman. “There’s plenty of room at the bottom”. *Caltech Engineering and Science*, **23**(5):22–36, February 1960.
- [2] Stéphane Mornet, Sébastien Vasseur, Fabien Grasset, and Etienne Duguet. “Magnetic nanoparticle design for medical diagnosis and therapy”. *J. Mater. Chem.*, **14**(14):2161–2175, July 2004. doi: 10.1039/B402025A.
- [3] Q. A. Pankhurst, J. Connolly, S. K. Jones, and J. Dobson. “Applications of magnetic nanoparticles in biomedicine”. *J. Phys. D: Appl. Phys.*, **36**(13):R167, July 2003. doi: 10.1088/0022-3727/36/13/201.
- [4] Sang Jun Son, Jonathan Reichel, Bo He, Mattan Schuchman, and Sang Bok Lee. “Magnetic nanotubes for magnetic-field-assisted bioseparation, biointeraction, and drug delivery”. *J. Am. Chem. Soc.*, **127**(20):7316–7317, May 2005. doi: 10.1021/ja0517365.
- [5] Esther Amstad, Stefan Zurcher, Alireza Mashaghi, Joyce Y. Wong, Marcus Textor, and Erik Reimhult. “Surface functionalization of single superparamagnetic iron oxide nanoparticles for targeted magnetic resonance imaging”. *Small*, **5**(11):1334–1342, 2009. doi: 10.1002/smll.200801328.
- [6] Dong-Hyun Kim, Elena A. Rozhkova, Ilya V. Ulasov, Samuel D. Bader, Tijana Rajh, Maciej S. Lesniak, and Valentyn Novosad. “Biofunctionalized magnetic-vortex microdiscs for targeted cancer-cell destruction”. *Nat Mater*, **9**(2):165–171, February 2010. doi: 10.1038/nmat2591.
- [7] Wei-Syuan Lin, Hong-Ming Lin, Hsiang-Hsin Chen, Yeu-Kuang Hwu, and Yuh-Jing Chiou. “Shape effects of iron nanowires on hyperthermia treatment”. *Journal of Nanomaterials*, **2013**:e237439, May 2013. doi: 10.1155/2013/237439.
- [8] J. A. Sidles, J. L. Garbini, K. J. Bruland, D. Rugar, O. Züger, S. Hoen, and C. S. Yannoni. “Magnetic resonance force microscopy”. *Rev. Mod. Phys.*, **67**(1):249–265, January 1995. doi: 10.1103/RevModPhys.67.249.
- [9] M. Poggio and C. L. Degen. “Force-detected nuclear magnetic resonance: recent advances and future challenges”. *Nanotechnology*, **21**(34):342001, August 2010. doi: 10.1088/0957-4484/21/34/342001.
- [10] H. J. Mamin, T. H. Oosterkamp, M. Poggio, C. L. Degen, C. T. Rettner, and D. Rugar. “Isotope-selective detection and imaging of organic nanolayers”. *Nano Lett.*, **9**(8):3020–3024, August 2009. doi: 10.1021/nl901466p.
- [11] C. L. Degen, M. Poggio, H. J. Mamin, C. T. Rettner, and D. Rugar. “Nanoscale magnetic resonance imaging”. *PNAS*, **106**(5):1313–1317, February 2009. doi: 10.1073/pnas.0812068106.

- [12] Stuart S. P. Parkin, Masamitsu Hayashi, and Luc Thomas. “Magnetic domain-wall race-track memory”. *Science*, **320**(5873):190–194, April 2008. doi: 10.1126/science.1145799.
- [13] James Clerk Maxwell. “A dynamical theory of the electromagnetic field”. *Phil. Trans. R. Soc. Lond.*, **155**:459–512, January 1865. doi: 10.1098/rstl.1865.0008.
- [14] Ralph Skomski and J. M. D. Coey. *Permanent Magnetism*. Institute of Physics Publishing, January 1999. ISBN 9780750304788.
- [15] Allan H. Morrish. *The Physical Principles of Magnetism*. Wiley, January 2001. ISBN 9780780360297.
- [16] Amikam Aharoni. *Introduction to the Theory of Ferromagnetism*. Oxford University Press, 2000. ISBN 9780198508090.
- [17] Charles-Augustin de Coulomb. “Septième mémoire sur l’électricité et le magnétisme”. *Histoire de l’Académie Royale des Sciences*, pages 455–505, 1789.
- [18] J. M. D. Coey. “New permanent magnets; manganese compounds”. *J. Phys.: Condens. Matter*, **26**(6):064211, February 2014. doi: 10.1088/0953-8984/26/6/064211.
- [19] J. A. Osborn. “Demagnetizing factors of the general ellipsoid”. *Phys. Rev.*, **67**(11-12):351–357, June 1945. doi: 10.1103/PhysRev.67.351.
- [20] E. C. Stoner and E. P. Wohlfarth. “A mechanism of magnetic hysteresis in heterogeneous alloys”. *Phil. Trans. R. Soc. Lond. A*, **240**(826):599–642, May 1948. doi: 10.1098/rsta.1948.0007.
- [21] B. C. Stipe, H. J. Mamin, T. D. Stowe, T. W. Kenny, and D. Rugar. “Magnetic dissipation and fluctuations in individual nanomagnets measured by ultrasensitive cantilever magnetometry”. *Phys. Rev. Lett.*, **86**(13):2874–2877, March 2001. doi: 10.1103/PhysRevLett.86.2874.
- [22] D. P. Weber, D. Ruffer, A. Buchter, F. Xue, E. Russo-Averchi, R. Huber, P. Berberich, J. Arbiol, A. Fontcuberta i Morral, D. Grundler, and M. Poggio. “Cantilever magnetometry of individual ni nanotubes”. *Nano Lett.*, **12**(12):6139–6144, December 2012. doi: 10.1021/nl302950u.
- [23] Charles Kittel. *Introduction to Solid State Physics*. Wiley, 8th edition, November 2004. ISBN 978-0471415268. URL <http://archive.org/details/IntroductionToSolidStatePhysics>.
- [24] L. Ruppert. *History of the International Electrotechnical Commission*. Bureau Central de la Commission Electrotechnique Internationale, Geneve, Suisse, 1956.
- [25] R. B. Goldfarb and F. R. Fickett. *Units for Magnetic Properties*. Number 696 in NBS Special Publication. U.S. Department of Commerce, National Bureau of Standards, Boulder 80303, Colorado, USA, March 1985.
- [26] William Fuller Brown. “Theory of the approach to magnetic saturation”. *Phys. Rev.*, **58**(8):736–743, October 1940. doi: 10.1103/PhysRev.58.736.
- [27] L. D. Landau and E. M. Lifshitz. *Mechanics, Third Edition: Volume 1*. Butterworth-Heinemann, Oxford, 3 edition edition, January 1976. ISBN 9780750628969.
- [28] Riccardo Hertel and Jürgen Kirschner. “Magnetic drops in a soft-magnetic cylinder”. *Journal of Magnetism and Magnetic Materials*, **278**(3):L291–L297, July 2004. doi: 10.

1016/j.jmmm.2004.02.032.

- [29] P. Landeros, O. J. Suarez, A. Cuchillo, and P. Vargas. “Equilibrium states and vortex domain wall nucleation in ferromagnetic nanotubes”. *Phys. Rev. B*, **79**(2):024404, January 2009. doi: 10.1103/PhysRevB.79.024404.
- [30] Z. Wang. “Spin waves in nickel nanorings of large aspect ratio”. *Phys. Rev. Lett.*, **94**(13), 2005. doi: 10.1103/PhysRevLett.94.137208.
- [31] Jesco Topp. “Internal spin-wave confinement in magnetic nanowires due to zig-zag shaped magnetization”. *Phys. Rev. B*, **78**(2), 2008. doi: 10.1103/PhysRevB.78.024431.
- [32] P. Landeros and Álvaro S. Núñez. “Domain wall motion on magnetic nanotubes”. *Journal of Applied Physics*, **108**(3):033917, August 2010. doi: 10.1063/1.3466747.
- [33] Robert Streubel, Jehyun Lee, Denys Makarov, Mi-Young Im, Daniil Karnaushenko, Luyang Han, Rudolf Schäfer, Peter Fischer, Sang-Koog Kim, and Oliver G. Schmidt. “Magnetic microstructure of rolled-up single-layer ferromagnetic nanomembranes”. *Adv. Mater.*, **26**(2):316–323, January 2014. doi: 10.1002/adma.201303003.
- [34] Robert Streubel, Volodymyr P. Kravchuk, Denis D. Sheka, Denys Makarov, Florian Kronast, Oliver G. Schmidt, and Yuri Gaididei. “Equilibrium magnetic states in individual hemispherical permalloy caps”. *Applied Physics Letters*, **101**(13):132419, September 2012. doi: 10.1063/1.4756708.
- [35] Robert Streubel, Denys Makarov, Jehyun Lee, Christian Müller, Michael Melzer, Rudolf Schäfer, Carlos Cesar Bof Bufon, Sang-Koog Kim, and Oliver G. Schmidt. “Rolled-up permalloy nanomembranes with multiple windings”. *SPIN*, **03**(03):1340001, September 2013. doi: 10.1142/S2010324713400018.
- [36] P. Landeros, S. Allende, J. Escrig, E. Salcedo, D. Altbir, and E. E. Vogel. “Reversal modes in magnetic nanotubes”. *Applied Physics Letters*, **90**(10):102501, March 2007. doi: 10.1063/1.2437655.
- [37] J. Escrig, J. Bachmann, J. Jing, M. Daub, D. Altbir, and K. Nielsch. “Crossover between two different magnetization reversal modes in arrays of iron oxide nanotubes”. *Phys. Rev. B*, **77**(21):214421, June 2008. doi: 10.1103/PhysRevB.77.214421.
- [38] Ole Albrecht, Robert Zierold, Sebastián Allende, Juan Escrig, Christian Patzig, Bernd Rauschenbach, Kornelius Nielsch, and Detlef Görlitz. “Experimental evidence for an angular dependent transition of magnetization reversal modes in magnetic nanotubes”. *Journal of Applied Physics*, **109**(9):093910, May 2011. doi: 10.1063/1.3583666.
- [39] Julien Bachmann, Juan Escrig, Kristina Pitzschel, Josep M. Montero Moreno, Jing Jing, Detlef Görlitz, Dora Altbir, and Kornelius Nielsch. “Size effects in ordered arrays of magnetic nanotubes: Pick your reversal mode”. *Journal of Applied Physics*, **105**(7):07B521, March 2009. doi: 10.1063/1.3074109.
- [40] Daniel Ruffer, Rupert Huber, Paul Berberich, Stephan Albert, Eleonora Russo-Averchi, Martin Heiss, Jordi Arbiol, Anna Fontcuberta i Morral, and Dirk Grundler. “Magnetic states of an individual ni nanotube probed by anisotropic magnetoresistance”. *Nanoscale*, **4**(16):4989–4995, July 2012. doi: 10.1039/C2NR31086D.
- [41] F. Castaño. “Metastable states in magnetic nanorings”. *Phys. Rev. B*, **67**(18), 2003. doi: 10.1103/PhysRevB.67.184425.

- [42] Daniel Ruffer. *Magnetic States and Spin-Wave Modes in Single Ferromagnetic Nanotubes*. PhD thesis, EPFL, Lausanne, Switzerland, 2014.
- [43] W. L. Bragg. “The diffraction of short electromagnetic waves by a crystal”. In *Proceedings of the Cambridge Philosophical Society*, volume 17, pages 43–57. Cambridge Philosophical Society, Cambridge, 1913. URL <http://archive.org/details/proceedingsofcam1718191316camb>.
- [44] Robert Streubel, Dominic J. Thurmer, Denys Makarov, Florian Kronast, Tobias Kossob, Volodymyr Kravchuk, Denis D. Sheka, Yuri Gaididei, Rudolf Schäfer, and Oliver G. Schmidt. “Magnetically capped rolled-up nanomembranes”. *Nano Lett.*, **12**(8):3961–3966, August 2012. doi: 10.1021/nl301147h.
- [45] E. H. Hall. “On a new action of the magnet on electric currents”. *American Journal of Mathematics*, **2**(3):287–292, September 1879. doi: 10.2307/2369245.
- [46] M. Daub, M. Knez, U. Goesele, and K. Nielsch. “Ferromagnetic nanotubes by atomic layer deposition in anodic alumina membranes”. *Journal of Applied Physics*, **101**(9):09J111, May 2007. doi: 10.1063/1.2712057.
- [47] Julien Bachmann, Jing, Mato Knez, Sven Barth, Hao Shen, Sanjay Mathur, Ulrich Gösele, and Kornelius Nielsch. “Ordered iron oxide nanotube arrays of controlled geometry and tunable magnetism by atomic layer deposition”. *J. Am. Chem. Soc.*, **129**(31):9554–9555, August 2007. doi: 10.1021/ja072465w.
- [48] Yuen Tung Chong, Detlef Görlitz, Stephan Martens, Man Yan Eric Yau, Sebastian Allende, Julien Bachmann, and Kornelius Nielsch. “Multilayered core/shell nanowires displaying two distinct magnetic switching events”. *Advanced Materials*, **22**(22):2435–2439, 2010. doi: 10.1002/adma.200904321.
- [49] Andreas Rudolph, Marcello Soda, Matthias Kiessling, Tomasz Wojtowicz, Dieter Schuh, Werner Wegscheider, Josef Zweck, Christian Back, and Elisabeth Reiger. “Ferromagnetic GaAs/GaMnAs core-shell nanowires grown by molecular beam epitaxy”. *Nano Lett.*, **9**(11):3860–3866, November 2009. doi: 10.1021/nl9020717.
- [50] A. Buchter, J. Nagel, D. Ruffer, F. Xue, D. P. Weber, O. F. Kieler, T. Weimann, J. Kohlmann, A. B. Zorin, E. Russo-Averchi, R. Huber, P. Berberich, A. Fontcuberta i Morral, M. Kemmler, R. Kleiner, D. Koelle, D. Grundler, and M. Poggio. “Reversal mechanism of an individual ni nanotube simultaneously studied by torque and SQUID magnetometry”. *Phys. Rev. Lett.*, **111**(6):067202, August 2013. doi: 10.1103/PhysRevLett.111.067202.
- [51] S. Li. “Flux closure structures in cobalt rings”. *Phys. Rev. Lett.*, **86**(6):1102–1105, 2001. doi: 10.1103/PhysRevLett.86.1102.
- [52] Sakhrat Khizroev, Mark H. Kryder, Dmitri Litvinov, and David A. Thompson. “Direct observation of magnetization switching in focused-ion-beam-fabricated magnetic nanotubes”. *Applied Physics Letters*, **81**(12):2256–2257, September 2002. doi: 10.1063/1.1508164.
- [53] H. Campanella, M. Jaafar, J. Llobet, J. Esteve, M. Vázquez, A. Asenjo, R. P. del Real, and J. A. Plaza. “Nanomagnets with high shape anisotropy and strong crystalline anisotropy: perspectives on magnetic force microscopy”. *Nanotechnology*, **22**(50):505301, December 2011. doi: 10.1088/0957-4484/22/50/505301.

- [54] L. Rondin, J.-P. Tetienne, T. Hingant, J.-F. Roch, P. Maletinsky, and V. Jacques. “Magnetometry with nitrogen-vacancy defects in diamond”. *Rep. Prog. Phys.*, **77**(5):056503, May 2014. doi: 10.1088/0034-4885/77/5/056503.
- [55] Hendrik Antoon Lorentz. *La théorie électromagnétique de Maxwell et son application aux corps mouvants*. Archives néerlandaises des sciences exactes et naturelles, T. XXV. E.J. Brill, Leiden, 1892. URL <http://archive.org/details/lathorielectrom00loregoog>.
- [56] Rafal E. Dunin-Borkowski, Takeshi Kasama, Alexander Wei, Steven L. Tripp, Martin J. Hÿtch, Etienne Snoeck, Richard J. Harrison, and Andrew Putnis. “Off-axis electron holography of magnetic nanowires and chains, rings, and planar arrays of magnetic nanoparticles”. *Microsc. Res. Tech.*, **64**(5-6):390–402, August 2004. doi: 10.1002/jemt.20098.
- [57] John Kerr. “XLIII. on rotation of the plane of polarization by reflection from the pole of a magnet”. *Philosophical Magazine Series 5*, **3**(19):321–343, 1877. doi: 10.1080/14786447708639245.
- [58] D. A. Allwood, Gang Xiong, M. D. Cooke, and R. P. Cowburn. “Magneto-optical kerr effect analysis of magnetic nanostructures”. *J. Phys. D: Appl. Phys.*, **36**(18):2175, September 2003. doi: 10.1088/0022-3727/36/18/001.
- [59] A. C. Bleszynski-Jayich, W. E. Shanks, B. Peaudecerf, E. Ginossar, F. von Oppen, L. Glazman, and J. G. E. Harris. “Persistent currents in normal metal rings”. *Science*, **326**(5950):272–275, October 2009. doi: 10.1126/science.1178139.
- [60] J. Jang, D. G. Ferguson, V. Vakaryuk, R. Budakian, S. B. Chung, P. M. Goldbart, and Y. Maeno. “Observation of half-height magnetization steps in sr2ruo4”. *Science*, **331**(6014):186–188, January 2011. doi: 10.1126/science.1193839.
- [61] Palash Banerjee, F. Wolny, D. V. Pelekhov, M. R. Herman, K. C. Fong, U. Weissker, T. Mühl, Yu Obukhov, A. Leonhardt, B. Büchner, and P. Chris Hammel. “Magnetization reversal in an individual 25 nm iron-filled carbon nanotube”. *Applied Physics Letters*, **96**(25):252505, June 2010. doi: 10.1063/1.3440951.
- [62] SangGap Lee, Eric W. Moore, Steven A. Hickman, Jonilyn G. Longenecker, and John A. Marohn. “Switching through intermediate states seen in a single nickel nanorod by cantilever magnetometry”. *Journal of Applied Physics*, **111**(8):083911, April 2012. doi: 10.1063/1.3699363.
- [63] C. A. Bolle, V. Aksyuk, F. Pardo, P. L. Gammel, E. Zeldov, E. Bucher, R. Boie, D. J. Bishop, and D. R. Nelson. “Observation of mesoscopic vortex physics using micromechanical oscillators”. *Nature*, **399**(6731):43–46, May 1999. doi: 10.1038/19924.
- [64] Joonho Jang, Raffi Budakian, and Yoshiteru Maeno. “Phase-locked cantilever magnetometry”. *Applied Physics Letters*, **98**(13):132510, March 2011. doi: 10.1063/1.3572026.
- [65] D. Rugar, H. J. Mamin, and P. Guethner. “Improved fiber-optic interferometer for atomic force microscopy”. *Applied Physics Letters*, **55**(25):2588–2590, December 1989. doi: 10.1063/1.101987.
- [66] Andrew N Cleland. *Foundations of Nanomechanics From Solid-State Theory to Device Applications*. Springer Berlin Heidelberg, Berlin, Heidelberg, 2003. ISBN 9783662052877 3662052873. URL <http://dx.doi.org/10.1007/978-3-662-05287-7>.

- [67] Michele Montinaro. *Coupling of Nanomechanical Resonators to Controllable Quantum Systems*. PhD thesis, Universität Basel, Basel, Switzerland, 2014. URL <http://edoc.unibas.ch>.
- [68] John A. Marohn, Raúl Fainchtein, and Doran D. Smith. “An optimal magnetic tip configuration for magnetic-resonance force microscopy of microscale buried features”. *Applied Physics Letters*, **73**(25):3778–3780, December 1998. doi: 10.1063/1.122892.
- [69] Moresi Giorgio, Beat Meier, Richard Magin, and Ernst Meyer. “Magnetic damping losses of tipped cantilevers”. *Nanotechnology*, **17**(3):871, February 2006. doi: 10.1088/0957-4484/17/3/043.
- [70] J. G. E. Harris, D. D. Awschalom, F. Matsukura, H. Ohno, K. D. Maranowski, and A. C. Gossard. “Integrated micromechanical cantilever magnetometry of  $\text{Ga}_{1-x}\text{Mn}_x\text{As}$ ”. *Applied Physics Letters*, **75**(8):1140–1142, August 1999. doi: 10.1063/1.124622.
- [71] Akashdeep Kamra, Michael Schreier, Hans Huebl, and Sebastian T. B. Goennenwein. “Theoretical model for torque differential magnetometry of single-domain magnets”. *Phys. Rev. B*, **89**(18):184406, 2014. doi: 10.1103/PhysRevB.89.184406.
- [72] T. Schwarze and D. Grundler. “Magnonic crystal wave guide with large spin-wave propagation velocity in CoFeB”. *Applied Physics Letters*, **102**(22):222412, June 2013. doi: 10.1063/1.4809757.
- [73] Ming Yan, Christian Andreas, Attila Kákay, Felipe García-Sánchez, and Riccardo Hertel. “Chiral symmetry breaking and pair-creation mediated walker breakdown in magnetic nanotubes”. *Applied Physics Letters*, **100**(25):252401, June 2012. doi: 10.1063/1.4727909.
- [74] Jack Gwynne Emmet Harris. *High sensitivity magnetization studies of semiconductor heterostructures*. Ph.d., University of California, Santa Barbara, United States – California, 2000. URL <http://search.proquest.com/docview/304600438/abstract?accountid=14616>.
- [75] Amikam Aharoni. “Demagnetizing factors for rectangular ferromagnetic prisms”. *Journal of Applied Physics*, **83**(6):3432–3434, March 1998. doi: 10.1063/1.367113.
- [76] B.W. Chui, Y. Hishinuma, R. Budakian, H.J. Mamin, T.W. Kenny, and D. Rugar. “Mass-loaded cantilevers with suppressed higher-order modes for magnetic resonance force microscopy”. In *TRANSDUCERS, Solid-State Sensors, Actuators and Microsystems, 12th International Conference on, 2003*, volume 2, pages 1120–1123 vol.2, June 2003. doi: 10.1109/SENSOR.2003.1216966. 00025.
- [77] Fei Xue, P. Peddibhotla, M. Montinaro, D. P. Weber, and M. Poggio. “A geometry for optimizing nanoscale magnetic resonance force microscopy”. *Applied Physics Letters*, **98**(16):163103, April 2011. doi: 10.1063/1.3579521.
- [78] Z. Wang. “Spin-wave quantization in ferromagnetic nickel nanowires”. *Phys. Rev. Lett.*, **89**(2), 2002. doi: 10.1103/PhysRevLett.89.027201.
- [79] R. Huber, T. Schwarze, P. Berberich, T. Rapp, and D. Grundler. “Atomic layer deposition for the fabrication of magnonic metamaterials”. In *Metamaterials 2011: The Fifth International Congress on Advanced Electromagnetic Materials in Microwaves and Optics, Metamorphose-VI*, pages 588–590, Barcelona, Spain, 2011. ISBN 978-952-67611-0-7.

- [80] F. Heimbach. “Characterization of thin films used to prepare ferromagnetic nanotubes on GaAs nanowires”, March 2014. Oral Presentation.
- [81] C. A. Neugebauer. “Saturation magnetization of nickel films of thickness less than 100 Å”. *Phys. Rev.*, **116**(6):1441–1446, December 1959. doi: 10.1103/PhysRev.116.1441.
- [82] Wei Gong, Hua Li, Zhongren Zhao, and Jinchang Chen. “Ultrafine particles of Fe, Co, and Ni ferromagnetic metals”. *Journal of Applied Physics*, **69**(8):5119–5121, April 1991. doi: 10.1063/1.348144.
- [83] Daniel Ruffer, Marlou Slot, Rupert Huber, Thomas Schwarze, Florian Heimbach, Gözde Tütüncüoğlu, Federico Matteini, Eleonora Russo-Averchi, András Kovács, Rafal Dunin-Borkowski, Reza R. Zamani, Joan R. Morante, Jordi Arbiol, Anna Fontcuberta i Morral, and Dirk Grundler. “Anisotropic magnetoresistance of individual CoFeB and Ni nanotubes with values of up to 1.4% at room temperature”. *APL Materials*, **2**(7):076112, July 2014. doi: 10.1063/1.4891276.
- [84] A. T. Hindmarch, C. J. Kinane, M. MacKenzie, J. N. Chapman, M. Henini, D. Taylor, D. A. Arena, J. Dvorak, B. J. Hickey, and C. H. Marrows. “Interface induced uniaxial magnetic anisotropy in amorphous CoFeB films on AlGaAs(001)”. *Phys. Rev. Lett.*, **100**(11):117201, March 2008. doi: 10.1103/PhysRevLett.100.117201.
- [85] Fei Xue, D. P. Weber, P. Peddibhotla, and M. Poggio. “Measurement of statistical nuclear spin polarization in a nanoscale GaAs sample”. *Phys. Rev. B*, **84**(20):205328, November 2011. doi: 10.1103/PhysRevB.84.205328.
- [86] P. Peddibhotla, F. Xue, H. I. T. Hauge, S. Assali, E. P. a. M. Bakkers, and M. Poggio. “Harnessing nuclear spin polarization fluctuations in a semiconductor nanowire”. *Nat Phys*, **9**(10):631–635, October 2013. doi: 10.1038/nphys2731.
- [87] P. Peddibhotla. *Magnetic Resonance Force Microscopy: Harnessing Nuclear Spin Fluctuations*. PhD thesis, Universität Basel, Basel, Switzerland, 2013. URL <http://edoc.unibas.ch>.
- [88] K. J. Bruland, J. L. Garbini, W. M. Dougherty, S. H. Chao, S. E. Jensen, and J. A. Sidles. “Thermal tuning of a fiber-optic interferometer for maximum sensitivity”. *Review of Scientific Instruments*, **70**(9):3542–3544, September 1999. doi: 10.1063/1.1149947.
- [89] A. Mehlin, F. Xue, and M. Poggio. “Stabilized skyrmion phase in MnSi nanowires detected by dynamic cantilever magnetometry”. *submitted*, July 2014.
- [90] A. A. Abrikosov. “The magnetic properties of superconducting alloys”. *Journal of Physics and Chemistry of Solids*, **2**(3):199–208, 1957. doi: 10.1016/0022-3697(57)90083-5.
- [91] Zhuoyi. “Periodic table of the elements by fiveless on deviantART”, January 2013. URL <http://fav.me/d2fq88e>.





## **A. Source Code Wolfram Mathematica**

# On Frequency Shift

`Clear["Global`*"]`

Greek letter names are the primed coordinate system, small  $\theta$  is the angle between applied field and z'-axis.

`R = RotationTransform[ $\theta$ , {1, 0, 0}]`

`MM = M (Sin[Theta] Sin[Phi], Sin[Theta] Cos[Phi], Cos[Theta])`

`MR = R [MM]`

`HH = {0, 0, 1} H`

$$\text{TransformationFunction} \left[ \begin{pmatrix} 1 & 0 & 0 & 0 \\ 0 & \cos(\theta) & -\sin(\theta) & 0 \\ 0 & \sin(\theta) & \cos(\theta) & 0 \\ 0 & 0 & 0 & 1 \end{pmatrix} \right]$$

`{M Sin[Phi] Sin[Theta], M Cos[Phi] Sin[Theta], M Cos[Theta]}`

`{M Sin[Phi] Sin[Theta],  
M Cos[Phi] Cos[Theta] Sin[Theta] - M Cos[Theta] Sin[Theta],  
M Cos[Theta] Cos[Theta] + M Cos[Phi] Sin[Theta] Sin[Theta]}  
{0, 0, H}`

So we will stay in the unprimed coordinate system:

## Total Energy:

$$Ez = -\mu \mathbf{V} \cdot \mathbf{MR} \cdot \mathbf{HH}$$

$$= -H \mu (M \cos[\text{Theta}] \cos[\theta] + M \cos[\text{Phi}] \sin[\text{Theta}] \sin[\theta])$$

$$Hdm = \begin{pmatrix} Dx & 0 & 0 \\ 0 & Dy & 0 \\ 0 & 0 & Dz \end{pmatrix} \cdot \mathbf{MM};$$

`Ems = FullSimplify[- $\mu$  / 2 V R [Hdm] . MR];`  
`Ems = FullSimplify[Ems]`

$$\frac{1}{4} - M^2 V \mu (2 Dz \cos[\text{Theta}]^2 + (Dx + Dy + (-Dx + Dy) \cos[2 \text{Phi}]) \sin[\text{Theta}]^2)$$

`Eosc = k / 2 (1 sin[ $\theta$ ])^2`

$$\frac{1}{2} k \frac{1}{2} \sin^2(\theta)$$

`Etot = Ez + Ems + Eosc`

$$\frac{1}{4} - M^2 V \mu$$

$$(2 Dz \cos[\text{Theta}]^2 + (Dx + Dy + (-Dx + Dy) \cos[2 \text{Phi}]) \sin[\text{Theta}]^2) + \frac{1}{2} k \frac{1}{2} \sin^2(\theta) - H \mu (M \cos[\text{Theta}] \cos[\theta] + M \cos[\text{Phi}] \sin[\text{Theta}] \sin[\theta])$$

## Find Frq Shift:

`Etot = Ez + Ems + Eosc`  
`Etot = Etot /. Theta -> Theta[ $\theta$ ] /. Phi -> Phi[ $\theta$ ]`

$$\frac{1}{4} - M^2 V \mu$$

$$(2 Dz \cos[\text{Theta}]^2 + (Dx + Dy + (-Dx + Dy) \cos[2 \text{Phi}]) \sin[\text{Theta}]^2) + \frac{1}{2} k \frac{1}{2} \sin^2(\theta) - H \mu (M \cos[\text{Theta}] \cos[\theta] + M \cos[\text{Phi}] \sin[\text{Theta}] \sin[\theta])$$

$$\frac{1}{2} - k \frac{1}{2} \sin^2(\theta) -$$

`H  $\mu$  (M Cos[ $\theta$ ] Cos[Theta[ $\theta$ ]] + M Cos[Phi[ $\theta$ ]] Sin[ $\theta$ ] Sin[Theta[ $\theta$ ]]) +`

$$\frac{1}{4} - M^2 V \mu (2 Dz \cos[\text{Theta}[ $\theta$ ]]^2 +$$

$$(Dx + Dy + (-Dx + Dy) \cos[2 \text{Phi}[ $\theta$ ]]) \sin[\text{Theta}[ $\theta$ ]]^2)$$

`deriv1st = D [Etot,  $\theta$ ]`

$$k \frac{1}{2} \cos[\theta] \sin[\theta] -$$

`H  $\mu$  (-M Cos[Theta[ $\theta$ ]] Sin[ $\theta$ ] + M Cos[ $\theta$ ] Cos[Phi[ $\theta$ ]] Sin[Theta[ $\theta$ ]] -`

`M Sin[ $\theta$ ] Sin[Phi[ $\theta$ ]] Sin[Theta[ $\theta$ ]] Phi'[ $\theta$ ] +`

`M Cos[Phi[ $\theta$ ]] Cos[Theta[ $\theta$ ]] Sin[ $\theta$ ] Theta'[ $\theta$ ] -`

`M Cos[ $\theta$ ] Sin[Theta[ $\theta$ ]] Theta'[ $\theta$ ] +`

$$\frac{1}{4} - M^2 V \mu (-2 (-Dx + Dy) \sin[2 \text{Phi}[ $\theta$ ]] \sin[\text{Theta}[ $\theta$ ]]^2 \text{Phi}'[\theta] -$$

`4 Dz Cos[Theta[ $\theta$ ]] Sin[Theta[ $\theta$ ]] Theta'[ $\theta$ ] +`

`2 (Dx + Dy + (-Dx + Dy) Cos[2 Phi[ $\theta$ ]])`

`Cos[Theta[ $\theta$ ]] Sin[Theta[ $\theta$ ]] Theta'[ $\theta$ ])`

Second derivative of the energy:

`deriv2nd = D [deriv1st,  $\theta$ ]`

$$k \frac{1}{2} \cos[\theta]^2 - k \frac{1}{2} \sin[\theta]^2 - H \mu$$

$$(-M \cos[\theta] \cos[\text{Theta}[ $\theta$ ]] - M \cos[\text{Phi}[ $\theta$ ]] \sin[\theta] \sin[\text{Theta}[ $\theta$ ]] -$$

$$2 M \cos[\theta] \sin[\text{Phi}[ $\theta$ ]] \sin[\text{Theta}[ $\theta$ ]] \text{Phi}'[\theta] -$$

$$M \cos[\text{Phi}[ $\theta$ ]] \sin[\theta] \sin[\text{Theta}[ $\theta$ ]] \text{Phi}'[\theta] +$$

$$2 M \cos[\theta] \cos[\text{Phi}[ $\theta$ ]] \cos[\text{Theta}[ $\theta$ ]] \text{Theta}'[\theta] +$$

$$2 M \sin[\theta] \sin[\text{Theta}[ $\theta$ ]] \text{Theta}'[\theta] -$$

$$2 M \cos[\text{Theta}[ $\theta$ ]] \sin[\theta] \sin[\text{Phi}[ $\theta$ ]] \text{Phi}'[\theta] \text{Theta}'[\theta] -$$

$$M \cos[\theta] \cos[\text{Theta}[ $\theta$ ]] \text{Theta}'[\theta] -$$

$$M \cos[\text{Phi}[ $\theta$ ]] \sin[\theta] \sin[\text{Theta}[ $\theta$ ]] \text{Theta}'[\theta]^2 -$$

$$M \sin[\theta] \sin[\text{Phi}[ $\theta$ ]] \sin[\text{Theta}[ $\theta$ ]] \text{Phi}'[\theta] +$$

$$M \cos[\text{Phi}[ $\theta$ ]] \cos[\text{Theta}[ $\theta$ ]] \sin[\theta] \text{Theta}'[\theta] -$$

$$M \cos[\theta] \sin[\text{Theta}[ $\theta$ ]] \text{Theta}'[\theta] +$$

$$\frac{1}{4} - M^2 V \mu (-4 (-Dx + Dy) \cos[2 \text{Phi}[ $\theta$ ]] \sin[\text{Theta}[ $\theta$ ]]^2 \text{Phi}'[\theta]^2 -$$

$$4 (-Dx + Dy) \cos[\text{Theta}[ $\theta$ ]] \sin[2 \text{Phi}[ $\theta$ ]] \sin[\text{Theta}[ $\theta$ ]]$$

$$\text{Phi}'[\theta] \text{Theta}'[\theta] - 4 Dz \cos[\text{Theta}[ $\theta$ ]]^2 \text{Theta}'[\theta]^2 +$$

$$2 (Dx + Dy + (-Dx + Dy) \cos[2 \text{Phi}[ $\theta$ ]]) \cos[\text{Theta}[ $\theta$ ]]^2 \text{Theta}'[\theta]^2 +$$

$$4 Dz \sin[\text{Theta}[ $\theta$ ]]^2 \text{Theta}'[\theta]^2 -$$

$$2 (Dx + Dy + (-Dx + Dy) \cos[2 \text{Phi}[ $\theta$ ]]) \sin[\text{Theta}[ $\theta$ ]]^2 \text{Theta}'[\theta]^2 -$$

$$2 (-Dx + Dy) \sin[2 \text{Phi}[ $\theta$ ]] \sin[\text{Theta}[ $\theta$ ]]^2 \text{Phi}'[\theta] \text{Theta}'[\theta] -$$

$$4 Dz \cos[\text{Theta}[ $\theta$ ]] \sin[\text{Theta}[ $\theta$ ]] \text{Theta}'[\theta] +$$

$$2 (Dx + Dy + (-Dx + Dy) \cos[2 \text{Phi}[ $\theta$ ]])$$

$$\cos[\text{Theta}[ $\theta$ ]] \sin[\text{Theta}[ $\theta$ ]] \text{Theta}'[\theta])$$

$Dk = \text{FullSimplify}[\text{Derivative}[0, 0] / 1 \wedge 2]$

$$\frac{1}{1^2} \left( k \cdot 1^2 + \frac{H V \mu}{2} \left( \cos[\text{Theta}[0]] (1 - 2 \cos[\text{Phi}[0]]) \text{Theta}'[0] + \text{Theta}''[0]^2 \right) + \frac{\sin[\text{Theta}[0]] (2 \sin[\text{Phi}[0]] \text{Phi}'[0] + \text{Theta}''[0])}{2} + \frac{1}{2} M^2 V \mu \left( (Dx - Dy) \sin[2 \text{Phi}[0]] \sin[\text{Theta}[0]] + (4 \cos[\text{Theta}[0]] \text{Phi}'[0] \text{Theta}'[0] + \sin[2 \text{Theta}[0]] \text{Phi}''[0]) + \frac{1}{2} (Dx + Dy - 2 Dz) (2 \cos[2 \text{Theta}[0]] \text{Theta}'[0]^2 + \sin[2 \text{Theta}[0]] \text{Theta}''[0]) - \frac{1}{2} (Dx - Dy) \cos[2 \text{Phi}[0]] (-2 \text{Phi}'[0]^2 + 2 \cos[2 \text{Theta}[0]] (\text{Phi}'[0]^2 + \text{Theta}''[0]^2) + \sin[2 \text{Theta}[0]] \text{Theta}''[0]) \right) \right)$$

### Special Case (Eq. 3.18)

$\text{FullSimplify}[Dk /. \text{Phi}[0] \rightarrow 0 /. \text{Phi}'[0] \rightarrow 0]$

$$\frac{1}{1^2} \left( k \cdot 1^2 + M V \mu \left( H \cos[\text{Theta}[0]] (-1 + \text{Theta}'[0])^2 + (Dy - Dz) M \cos[2 \text{Theta}[0]] \text{Theta}'[0]^2 + (H + (Dy - Dz) M \cos[\text{Theta}[0]]) \sin[\text{Theta}[0]] \text{Theta}''[0] \right) \right)$$

### Test for known solutions:

$Dw1 = \text{FullSimplify}[w0 / 2 / k * \text{Factor}[Dk /. \text{Theta}[0] \rightarrow 0 /. \text{Theta}'[0] \rightarrow H / (M (Dy - Dz) + H) /. \text{Phi}[0] \rightarrow 0]]$

$$\frac{1}{2} w0 \left( 1 + \frac{(Dy - Dz) H M^2 V \mu}{k \cdot 1^2 (H + (Dy - Dz) M)} \right)$$

$Dw2 = \text{FullSimplify}[w0 / 2 / k * \text{Factor}[Dk /. \text{Theta}[0] \rightarrow \text{Pi} /. \text{Theta}'[0] \rightarrow H / (-M (Dy - Dz) + H) /. \text{Phi}[0] \rightarrow 0]]$

$$\frac{1}{2} w0 \left( 1 + \frac{(Dy - Dz) H M^2 V \mu}{k \cdot 1^2 (H + (-Dy + Dz) M)} \right)$$

$Dw3 = \text{FullSimplify}[\text{w0} / 2 / k * (\text{Dk} /. \text{Theta}[0] \rightarrow \text{ArcCos}[-H / (M (Dy - Dz))]) /. \text{Theta}'[0] \rightarrow H^2 / (M^2 (Dy - Dz)^2 - H^2) /. \text{Phi}[0] \rightarrow 0 /. \text{Phi}'[0] \rightarrow 0]$

$$\frac{1}{2} w0 \left( 1 + \frac{H^2 (2 H^2 - (Dy - Dz)^2 M^2) V \mu}{(Dy - Dz) k \cdot 1^2 (-H^2 + (Dy - Dz)^2 M^2)} \right)$$

### High Field Behavior:

$\text{Etot} = \text{Ez} + \text{Ems} + \text{Eosc} /. \text{Theta} \rightarrow \theta /. \text{Phi} \rightarrow 0$

$\text{DKHF} = \text{FullSimplify}[\text{D}[\text{D}[\text{Etot}, \theta], \theta] /. \theta \rightarrow 0] / 1 \wedge 2]$

$$\frac{1}{2} k \cdot 1^2 \sin[\theta]^2 + \frac{1}{4} M^2 V \mu (2 Dz \cos[\theta]^2 + 2 Dy \sin[\theta]^2) + H V \mu (M \cos[\theta]^2 + M \sin[\theta]^2) + k + \frac{(Dy - Dz) M^2 V \mu}{1^2}$$

# Demagnetization Factors

## Coordinate System

J. Appl. Phys., Vol. 63, No. 6, 15 March 1998

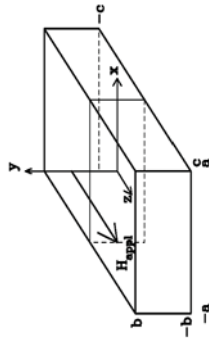


FIG. 1. The coordinate system used in the calculations. Its origin is at the center of the rectangular prism. The field  $H_{app}$  is applied along the z axis.

Taken from Aharoni98.

index	1	2	3	comment
coordinates	x	y	z	stay with cantilever, applied field in z direction, oscillation in y direction
parallel	w	t	l	are dimensions with stay with individual stripe,
SUPERPEN	t	l	w	assignment describing "first stripe",
PERPEN	l	t	w	which is the one attached to cantilever

Sample data taken from SampleSpecifications\_ Table. w is calculated as an average side length of an hexagon with the same volume/cross sectional area as the one of our sample with total widths hexD and hexC (in the document D and d, respectively).

## General Formula

```
Clear["Global`*"]
```

$$Dz[a_, b_, c_] = \left( \frac{b^2 - c^2}{2bc} \operatorname{Log} \left[ \frac{\sqrt{a^2 + b^2 + c^2} - a}{\sqrt{a^2 + b^2 + c^2} + a} \right] + \frac{a^2 - c^2}{2ac} \operatorname{Log} \left[ \frac{\sqrt{a^2 + b^2 + c^2} - b}{\sqrt{a^2 + b^2 + c^2} + b} \right] + \frac{b}{2c} \operatorname{Log} \left[ \frac{\sqrt{a^2 + b^2} + a}{\sqrt{a^2 + b^2} - a} \right] + \frac{a}{2c} \operatorname{Log} \left[ \frac{\sqrt{a^2 + b^2} + b}{\sqrt{a^2 + b^2} - b} \right] + \frac{c}{2a} \operatorname{Log} \left[ \frac{\sqrt{c^2 + b^2} - b}{\sqrt{c^2 + b^2} + b} \right] + \frac{c}{2b} \operatorname{Log} \left[ \frac{\sqrt{a^2 + c^2} - a}{\sqrt{a^2 + c^2} + a} \right] + 2 \operatorname{Arctan} \left[ \frac{ab}{c \sqrt{a^2 + b^2 + c^2}} \right] + \frac{a^2 + b^2 - 2c^2}{3abc} + \frac{a^2 + b^2 - 2c^2}{3abc} \sqrt{a^2 + b^2 + c^2} + \frac{c}{ab} \left( \sqrt{a^2 + c^2} + \sqrt{b^2 + c^2} \right) - \frac{3abc}{(a^2 + b^2)^{1.5} + (c^2 + b^2)^{1.5} + (a^2 + c^2)^{1.5}} \Bigg) \Bigg/ \pi$$

$$\frac{1}{\pi} \left( \frac{(a^2 + b^2 - 2c^2) \sqrt{a^2 + b^2 + c^2}}{3abc} + \frac{a^3 + b^3 - 2c^3}{3abc} + \frac{3abc}{(a^2 + b^2)^{1.5} + (a^2 + c^2)^{1.5} + (b^2 + c^2)^{1.5}} + \frac{3abc}{ab} \right)$$

$$2 \operatorname{Arctan} \left[ \frac{ab}{c \sqrt{a^2 + b^2 + c^2}} \right] + \frac{b \operatorname{Log} \left[ \frac{\sqrt{a^2 + b^2}}{-a + \sqrt{a^2 + b^2}} \right]}{2c} + \frac{a \operatorname{Log} \left[ \frac{b \sqrt{a^2 + b^2}}{-b + \sqrt{a^2 + b^2}} \right]}{2c} + \frac{c \operatorname{Log} \left[ \frac{-a \sqrt{a^2 + c^2}}{a + \sqrt{a^2 + c^2}} \right]}{2a} + \frac{c \operatorname{Log} \left[ \frac{-b \sqrt{b^2 + c^2}}{b + \sqrt{b^2 + c^2}} \right]}{2a} + \frac{(b^2 - c^2) \operatorname{Log} \left[ \frac{-a \sqrt{a^2 + b^2 + c^2}}{a + \sqrt{a^2 + b^2 + c^2}} \right]}{2bc} + \frac{(a^2 - c^2) \operatorname{Log} \left[ \frac{-b \sqrt{a^2 + b^2 + c^2}}{b + \sqrt{a^2 + b^2 + c^2}} \right]}{2ac}$$

## Ni Data

### Parallel Configuration

#### First stripe

$l = 21\,000;$   
 $t = 44;$   
 $cyld = 360;$   
 $cyld = 303;$   
 $w = N \left[ \frac{\pi}{6} \left( \frac{cyld + cyld}{2} - t \right) + \frac{t}{\sqrt{3}} \right]$   
 $DMw = Dz[t, l, w]$   
 $DMt = Dz[l, w, t]$   
 $DMl = Dz[w, t, l]$   
175.938  
0.229533  
0.768696  
0.00177116

#### Six stripes

$DMx = \frac{2}{3} DMw + \frac{1}{\sqrt{3}} DMt$   
 $DMperp = \frac{2}{3} DMt + \frac{1}{\sqrt{3}} DMw$   
 $DMpar = DMl$   
0.596829  
0.644985  
0.00177116  
 $DMperp - DMpar$   
0.643214

## suPERpen Configuration

#### First stripe

$l = 19\,800;$   
 $t = 44;$   
 $cyld = 381;$   
 $cyld = 270;$   
 $w = N \left[ \frac{\pi}{6} \left( \frac{cyld + cyld}{2} - t \right) + \frac{t}{\sqrt{3}} \right]$   
 $DMt = Dz[l, w, t]$   
 $DMl = Dz[w, t, l]$   
 $DMw = Dz[t, l, w]$   
172.796  
0.765897  
0.00186664  
0.232236

#### Six stripes

$DMx = \frac{2}{3} DMt + \frac{1}{\sqrt{3}} DMw$   
 $DMperp = DMl$   
 $DMpar = \frac{2}{3} DMw + \frac{1}{\sqrt{3}} DMt$   
0.644468  
0.00186664  
0.597015  
 $DMperp - DMpar$   
-0.595148

# CoFeB Data

## perpen Configuration

### First stripe

$l = 18200;$   
 $t = 44;$   
 $cyld = 349;$   
 $cyld = 274;$   
 $w = N \left[ \frac{\pi}{2} \left( \frac{cyld + cyld}{2} - t \right) + \frac{t}{\sqrt{3}} \right]$   
 $DML = Dz[t, w, l]$   
 $DML = Dz[w, l, t]$   
 $DMw = Dz[l, t, w]$   
1.65.466  
0.00199994  
0.75913  
0.23887

### Six stripes

$DML = DML$   
 $DMperp = \frac{2}{3} DML + \frac{1}{\sqrt{3}} DMw$   
 $DMpar = \frac{2}{3} DMw + \frac{1}{\sqrt{3}} DML$   
0.00199994  
0.64398  
0.597531  
 $DMperp - DMpar$   
0.0464678

## Parallel Configuration

### First stripe

$l = 10300;$   
 $t = 30;$   
 $hexD = 258;$   
 $hexd = 261;$   
 $w = N \left[ \frac{hexD + hexd \sqrt{3}}{5} - \frac{t}{\sqrt{3}} \right]$   
 $DMw = Dz[t, l, w]$   
 $DML = Dz[l, w, t]$   
 $DML = Dz[w, t, l]$   
124.693  
0.223489  
0.774018  
0.00249352

### Six stripes

$DMx = \frac{2}{3} DMw + \frac{1}{\sqrt{3}} DML$   
 $DMperp = \frac{2}{3} DML + \frac{1}{\sqrt{3}} DMw$   
 $DMpar = DML$   
0.595872  
0.645043  
0.00249352  
 $DMperp - DMpar$   
0.64255

## suPERpen Configuration

### First stripe

```
l = 12620;  
t = 30;  
hexD = 274;  
hexd = 242;  
w = N * [ (hexD + hexd * sqrt(3)) / 5 - t / sqrt(3) ]  
DMt = Dz[l, w, t]  
DML = Dz[w, t, l]  
DMw = Dz[t, l, w]  
121.311  
0.770226  
0.00201685  
0.227758
```

### Six stripes

```
DMx =  $\frac{2}{3}$  DMt +  $\frac{1}{\sqrt{3}}$  DMw  
DMperp = DMl  
DMpar =  $\frac{2}{3}$  DMw +  $\frac{1}{\sqrt{3}}$  DMt  
0.64498  
0.00201685  
0.596528  
DMperp - DMpar  
-0.594511
```

## perpen Configuration

### First stripe

```
l = 12020;  
t = 30;  
hexD = 248;  
hexd = 241;  
w = N * [ (hexD + hexd * sqrt(3)) / 5 - t / sqrt(3) ]  
DMl = Dz[l, w, l]  
DMt = Dz[w, l, t]  
DMw = Dz[l, t, w]  
115.764  
0.00208328  
0.763066  
0.234851
```

### Six stripes

```
DMx = DMl  
DMperp =  $\frac{2}{3}$  DMt +  $\frac{1}{\sqrt{3}}$  DMw  
DMpar =  $\frac{2}{3}$  DMw +  $\frac{1}{\sqrt{3}}$  DMt  
0.00208328  
0.644302  
0.597124  
DMperp - DMpar  
0.0471783
```

## Fit Frequency Data

104

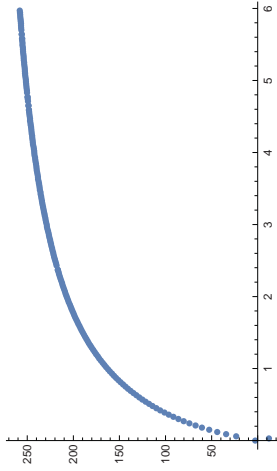
```
Clear["Global`*"]
```

### Path names

```
pathimport =
"p:\\Experiments\\CoFeB_NTs\\Analysis\\MainAnalysis_Paper\\
parallel\\HighField\\parallel_Up0to+6_FRQvsField_2013-05-28
00-09-19.dat";
pathexport =
"p:\\Experiments\\CoFeB_NTs\\Analysis\\MainAnalysis_Paper\\
parallel\\HighField\\parallel_Up0to+6_FIT_FRQvsField_2013-
05-28_00-09-19.dat";
```

### Import Data

```
file = Import[pathimport, "Table"];
ListPlot[file, AxesOrigin -> {0, 0}]
```



### Fit & find parameters

$$Df[H, M] := \frac{1}{2\pi} \frac{\omega_0}{2k_0} \frac{1}{l^2} \frac{\mu_0 M^2 V Ddelta H}{H + \mu_0 M Ddelta}$$

$$Df[H, M] = \frac{Ddelta H M^2 V \mu_0 \omega_0}{4 k_0 l^2 \pi (H + Ddelta M \mu_0)}$$

```
k0 = 48.7 * 10^-6;
omega0 = 2 * Pi * 2191.0;
l = 108.6 * 10^-6;
mu0 = 1.25663706 * 10^-6;
V = 2.26 * 10^-19;
ClearAll[Ddelta, H, M]

nlm = NonlinearModelFit[file, Df[H, M],
{{Ddelta, 0.6}, {M, 1.1/omega0}}, H, MaxIterations -> 10000]
FitPar = nlm["BestFitParameters"]
M = M /. FitPar;
Ddelta = Ddelta /. FitPar;
mu0 M /. FitPar
mu0 M Ddelta /. FitPar

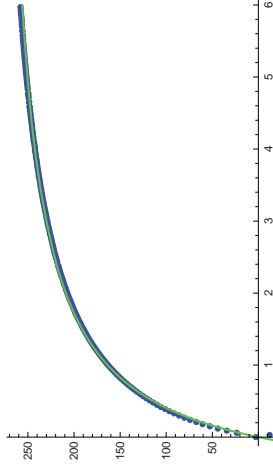
Show[ListPlot[file, PlotStyle -> Blue, AxesOrigin -> {0, 0}],
Plot[nlm[H], {H, -6, 6}, PlotStyle -> Green]]
```

```
FittedModel[


|              |
|--------------|
| 288.853 H    |
| 0.765739 + H |


]
```

```
{Ddelta -> 0.696318, M -> 875.112.}
1.0997
0.765739
```



### Export fit

```
Export[pathexport, Table[{H, Df[H, M]}, {H, 0, 6, 0.01}]];
```

## Calculate hysteresis curve



## Compute magnetizations

```

ClearAll[μ0, k0, ω0, l, H, Ddelta, V, M, deltaf]
MAG1[H_, deltaf_] :=
FullSimplify[M /. Solve[

$$\frac{1}{2\pi} \frac{\omega_0}{2k_0 l^2} \frac{1}{H + \mu_0 M Ddelta} = \text{deltaf}, M]]
MAG2[H_, deltaf_] := FullSimplify[
M /. Solve[

$$\frac{1}{2\pi} \frac{\omega_0}{2k_0 l^2} \frac{1}{H - \mu_0 M Ddelta} = \text{deltaf}, M]]
MAG3[H_, deltaf_] := FullSimplify[M /. Solve[

$$\frac{1}{2\pi} \frac{\omega_0}{2k_0 l^2} \frac{\mu_0 Ddelta}{-H^2 + \mu_0^2 M^2 Ddelta^2} = \text{deltaf}, M]]
MAG1[H, Δf]
MAG2[H, Δf]
MAG3[H, Δf]
{

$$\left( \left( 2 Ddelta k_0 l^2 \pi \Delta f \mu_0 - 2 \sqrt{\pi} \sqrt{Ddelta k_0 l^2 \Delta f \mu_0} \left( Ddelta k_0 l^2 \pi \Delta f \mu_0 + H^2 V \omega_0 \right) \right) / \left( Ddelta H V \mu_0 \omega_0 \right), \left( 2 \left( Ddelta k_0 l^2 \pi \Delta f \mu_0 + \sqrt{\pi} \sqrt{Ddelta k_0 l^2 \Delta f \mu_0} \left( Ddelta k_0 l^2 \pi \Delta f \mu_0 + H^2 V \omega_0 \right) \right) / \left( Ddelta H V \mu_0 \omega_0 \right) \right) \right) / \left( Ddelta k_0 l^2 \pi \Delta f \mu_0 + \sqrt{\pi} \sqrt{Ddelta k_0 l^2 \pi \Delta f \mu_0} \left( Ddelta k_0 l^2 \pi \Delta f \mu_0 + H^2 V \omega_0 \right) \right) \right) / \left( Ddelta H V \mu_0 \omega_0 \right), \left( -2 Ddelta k_0 l^2 \pi \Delta f \mu_0 + 2 \sqrt{\pi} \sqrt{Ddelta k_0 l^2 \Delta f \mu_0} \left( Ddelta k_0 l^2 \pi \Delta f \mu_0 + H^2 V \omega_0 \right) \right) / \left( Ddelta H V \mu_0 \omega_0 \right) \right) \}
{

$$\left( \left( \left( \sqrt{2} \sqrt{-H^2} \sqrt{2 Ddelta k_0 l^2 \pi \Delta f \mu_0 + H^2 V \omega_0} \right) / \left( \sqrt{(-Ddelta^2 \mu_0^2 (4 Ddelta k_0 l^2 \pi \Delta f \mu_0 + H^2 V \omega_0))} \right), \left( \sqrt{2} \sqrt{-H^2} \left( 2 Ddelta k_0 l^2 \pi \Delta f \mu_0 + H^2 V \omega_0 \right) \right) / \left( \sqrt{(-Ddelta^2 \mu_0^2 (4 Ddelta k_0 l^2 \pi \Delta f \mu_0 + H^2 V \omega_0))} \right) \right) \right) / \left( \sqrt{(-Ddelta^2 \mu_0^2 (4 Ddelta k_0 l^2 \pi \Delta f \mu_0 + H^2 V \omega_0))} \right) \right) \}$$$$$$$$$$

```

## Path names

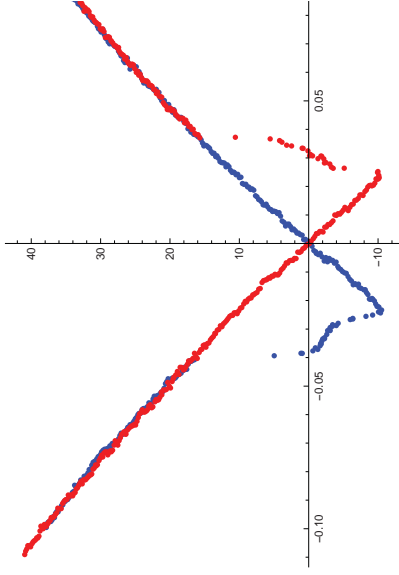
```

pathimportUP =
"P:\Experiments\CofEB_NTs\Analysis\MainAnalysis Paper\
Parallel\LowField\parallel_Up_FRQvsField_2013-05-28_19-45-
21.dat";
pathimportDOWN =
"P:\Experiments\CofEB_NTs\Analysis\MainAnalysis Paper\
Parallel\LowField\parallel_Down_FRQvsField_2013-05-28_22-
18-04.dat";
pathexportUP =
"P:\Experiments\CofEB_NTs\Analysis\MainAnalysis Paper\
Parallel\LowField\parallel_Up_Hystl_FRQvsField_2013-05-28_
19-45-21.dat";
pathexportDOWN =
"P:\Experiments\CofEB_NTs\Analysis\MainAnalysis Paper\
Parallel\LowField\parallel_Down_Hystl_FRQvsField_2013-05-
28_22-18-04.dat";

```

## Import data

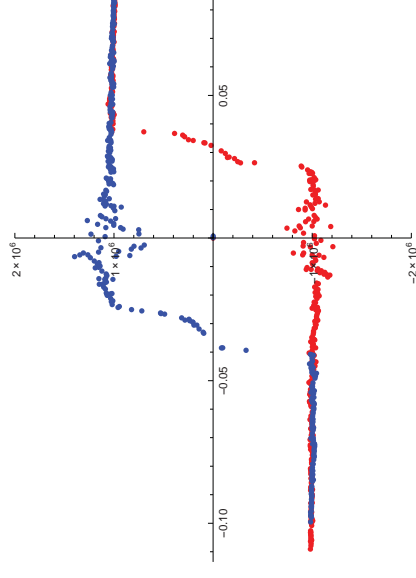
```
Upsweep = Import[pathImportUP, "Table"];
Downsweep = Import[pathImportDOWN, "Table"];
ListPlot[{Downsweep, Upsweep},
PlotStyle -> {Blue, Red}, ImageSize -> 500]
```



## Generate hysteresis plot

```
k0 = 48.7 * 10-6;
ω0 = 2 π * 2191.0;
l = 108.6 * 10-6;
μ0 = 1.25663706 * 10-6;
V = 2.26 * 10-13;
Delta = Delta /. FitPar;
```

```
ClearAll[H, M, deltaf, Hys1, Hys2, a, b, Df1, Df2, P, q, i, j]
a = 1; Df1 = 1;
Hys1 = Table[{P, 0, a, Df1}, {P, 1, Length[Upsweep]};
For[
i = 1,
i ≤ Length[Upsweep],
i++,
If[Sign[Df1] - Sign[Upsweep[[i, 2]]] == -2, a = 2];
Df1 = Upsweep[[i, 2]];
Hys1[[i]] = {Upsweep[[i, 1]],
MAG1[Upsweep[[i, 1]], Upsweep[[i, 2]]}][[a], a, Df1]
]
b = 2; Df2 = 1;
Hys2 = Table[{q, 0, b, Df2}, {q, 1, Length[Downsweep]};
For[
j = 1,
j ≤ Length[Downsweep],
j++,
If[Sign[Df2] - Sign[Downsweep[[j, 2]]] == -2, b = 1];
Df2 = Downsweep[[j, 2]];
Hys2[[j]] = {Downsweep[[j, 1]],
MAG1[Downsweep[[j, 1]], Downsweep[[j, 2]]}][[b], b, Df2]
]
ListPlot[{Hys1[All, 1; 2], Hys2[All, 1; 2]},
PlotStyle -> {Red, Blue},
PlotRange -> {-2 000 000, 2 000 000},
ImageSize -> 500]
```



## Export hysteresis data

```
Export[pathExportUP, Hys1];
Export[pathExportDOWN, Hys2];
```

## **B. Sample Specifications**

## B.1. Sample Specifications Ni

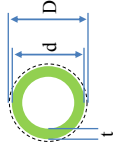
Si Cantilever		Ni Nanotube											
Configuration*	Length <sup>†</sup> ( $\mu\text{m}$ )	Effective Length <sup>‡</sup> $l_e$ ( $\mu\text{m}$ )	c-Factor <sup>§</sup>	Resonant Frequency** $f_0$ (Hz)	Spring Constant $k_0$ ( $\mu\text{N/m}$ )	Quality-Factor $Q_0$	Nanotube <sup>††</sup>	Length $l$ ( $\mu\text{m}$ )	Ni Shell Thickness $t$ (nm)	Outer Diameter (nm)	Volume <sup>‡‡</sup> $V$ ( $10^{-19}$ m <sup>3</sup> )	Demagnetization Factor ( $D_{\perp} - D_{\parallel}$ )	Saturation Magnetization $\mu_0 M_s$ (T)
													
								Max. $D$	Min. $d$	Avg. Facet $\langle a \rangle$ <sup>§§</sup>			
1	150.0 $\pm$ 0.5	105.0 $\pm$ 0.4	1.27	2808.5 (2801.9)	70 $\pm$ 10	25000	N1	21.0 $\pm$ 0.5	44 $\pm$ 9	360 $\pm$ 8	8.35 $\pm$ 1.79	0.66 $\pm$ 0.13	0.40 $\pm$ 0.07
2	150.0 $\pm$ 0.5	105.0 $\pm$ 0.4	1.27	2093.8 <sup>***</sup>	50 $\pm$ 10	42000	N2	19.8 $\pm$ 0.5	44 $\pm$ 9	381 $\pm$ 6	7.69 $\pm$ 1.65	-0.46 $\pm$ 0.13 <sup>†††</sup>	0.53 $\pm$ 0.12
3	150.0 $\pm$ 0.5	105.0 $\pm$ 0.4	1.27	2782.6 (2781.0)	50 $\pm$ 15	22000 (15000)	N3	18.2 $\pm$ 0.5	44 $\pm$ 9	349 $\pm$ 5	6.72 $\pm$ 1.44	0.01 $\pm$ 0.00	0.47 $\pm$ 0.12 <sup>†††</sup>

Table B1: Properties of the Si cantilever for each configuration at 4 K.

Table B2: Properties of the Ni nanotube sample for each configuration at 4 K.

\* Where “1” denotes “field parallel to NT” using cantilever W8Ec2-7L, “2” denotes “field perpendicular to NT (probing long axis, “suPERpendicular”)” using cantilever W15Ic3-4L, and “3” denotes “field perpendicular to NT (probing cross section, “perpendicular”)” using cantilever W8Ec2-7R.

<sup>†</sup> From optical micrographs. The precision is in the order of the cantilever half-tip-size.

<sup>‡</sup> Taken from simulation data for a length of 155  $\mu\text{m}$ , scaled to actual length.

<sup>§</sup> The c-factor is the ratio between the displacement of the tip and the paddle of the cantilever. From numerical simulation.

\*\* Frequency was calculated to be 2566.6 Hz from numerical simulations for a 155  $\mu\text{m}$ -long cantilever. Numbers in parentheses reflect the change in mass of the cantilever after one cool-down/warm-up cycle, likely due to adsorption of hydrocarbons or water present in the air.

<sup>††</sup> Taken from sample wafer “0602B”.

<sup>‡‡</sup> The volume of the nanotube is calculated as a hollow, truncated cone:  $V = \pi l t \left( \frac{D+d}{2} - t \right)$

<sup>§§</sup> Calculated from the measured dimensions,  $\langle a \rangle$  is the average facet size of a hexagonal hollow prism with the same volume as the calculated volume of our sample:  $\langle a \rangle = \frac{\pi}{6} \left( \frac{D+d}{2} - t \right) + \frac{t}{\sqrt{3}}$

<sup>\*\*\*</sup> Here the frequency is significantly lower compared to the other cantilevers of the same type. This frequency shift can be explained by an additional drop of glue unintentionally put on the cantilever.

<sup>†††</sup> Here the demagnetization factor is significantly lower (but still within the error) compared to the calculated -0.60. This is likely due to a magnetic material extrusion at one end of the sample.

<sup>‡‡‡</sup> The frequency data of configuration 3 cannot be fit, so this number is just the mean of the configurations 1 and 2.

## B.2. Sample Specifications CoFeB

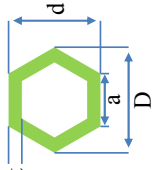
Si Cantilever		CoFeB Nanotube									
Configuration*		Nanotube**	Length** $l$ ( $\mu\text{m}$ )	CoFeB Shell Thickness $t$ (nm)					Volume*** $V$ ( $10^{-19}$ m <sup>3</sup> )	Demagnetization Factor ( $D_{\perp} - D_{\parallel}$ )	Saturation Magnetization $\mu_0 M_s$ (T)
1	154.5±0.5	C1	10.30±0.96***	30±2	Max. $D$	Facet $a$	Avg. Facet $\langle a \rangle^{***}$	2.26±0.46	0.67±0.02	1.12	
2	154.0±0.5	C2	12.62±0.03	30±2	Min. $d$			2.78±0.36	-0.62±0.02	1.07	
3	154.0±0.5	C3	12.02±0.03	30±2				2.42±0.40	0.10±0.00	1.09§§§	

Table B3: Properties of the Si cantilever for each configuration at 4 K.

Table B4: Properties of the CoFeB nanotube sample for each configuration at 4 K.

\* Where "1" denotes "field parallel to NT" using cantilever W14C1L, "2" denotes "field perpendicular to NT (probing long axis, "suPERpendicular")" using cantilever W15De4-3R, and "3" denotes "field perpendicular to NT (probing cross section, "perpendicular")" using cantilever W15Gc3-3L.

† From optical micrographs. The precision is in the order of the cantilever half-tip-size.

‡ Taken from numerical simulation data for a length of 155  $\mu\text{m}$ , scaled to actual length.

§ The c-factor is the ratio between the displacement of the tip and the paddle of the cantilever. From numerical simulation.

\*\* Frequency was calculated to be 2566.6 Hz from numerical simulations for a 155  $\mu\text{m}$ -long cantilever.

\*\*\* Taken from sample wafer "D1121109B".

§§ From SEM micrographs. The precision is in the order of the CoFeB shell thickness.

§§§ Facets are of different sizes on a non-perfect hexagon. Taken from SEM micrographs.

\*\*\*\* The volume of the nanotube is calculated as a hollow, hexagonal prism:  $V = (D + a + d\sqrt{3}) \cdot l \cdot t - 2\sqrt{3} \cdot l \cdot t^2$

\*\*\*\*\* Calculated from the measured dimensions,  $\langle a \rangle$  is the average facet size of an ideally hexagonal hollow prism with the same volume as the calculated volume of our sample:  $\langle a \rangle = \frac{D+d\sqrt{3}}{5} - \frac{t}{\sqrt{3}}$

\*\*\*\*\* Taken from comparison of optical images with SEM micrographs using pixel measurements.

§§§§ The frequency data of configuration 3 cannot be fit, so this number is just the mean of the configurations 1 and 2.



# C. Periodic Table of Chemical Elements

GROUP	1	2	3	4	5	6	7	8	9	10	11	12	13	14	15	16	17	18		
1	<b>H</b> hydrogen (1.00794)																			
2	<b>Li</b> lithium (6.941)	<b>Be</b> beryllium (9.012182)																		
3	<b>Na</b> sodium (22.98976928)	<b>Mg</b> magnesium (24.304)																		
4	<b>K</b> potassium (39.0983)	<b>Ca</b> calcium (40.078)	<b>Sc</b> scandium (44.955912)	<b>Ti</b> titanium (47.88)	<b>V</b> vanadium (50.9415)	<b>Cr</b> chromium (51.9961)	<b>Mn</b> manganese (54.938045)	<b>Fe</b> iron (55.845)	<b>Co</b> cobalt (58.933195)	<b>Ni</b> nickel (58.6934)	<b>Cu</b> copper (63.546)	<b>Zn</b> zinc (65.38)	<b>Ga</b> gallium (69.723)	<b>Ge</b> germanium (72.64)	<b>As</b> arsenic (74.9216)	<b>Se</b> selenium (78.96)	<b>Br</b> bromine (79.904)	<b>Kr</b> krypton (83.798)		
5	<b>Rb</b> rubidium (85.4678)	<b>Sr</b> strontium (87.62)	<b>Y</b> yttrium (88.90584)	<b>Zr</b> zirconium (91.224)	<b>Nb</b> niobium (92.90638)	<b>Mo</b> molybdenum (95.94)	<b>Tc</b> technetium (98.9062)	<b>Ru</b> ruthenium (101.07)	<b>Rh</b> rhodium (101.07)	<b>Pd</b> palladium (106.42)	<b>Ag</b> silver (107.8682)	<b>Cd</b> cadmium (112.411)	<b>In</b> indium (114.818)	<b>Sn</b> tin (118.710)	<b>Sb</b> antimony (121.757)	<b>Te</b> tellurium (127.603)	<b>I</b> iodine (126.905)	<b>Xe</b> xenon (131.29)		
6	<b>Cs</b> cesium (132.90545196)	<b>Ba</b> barium (137.327)	Lanthanoids	<b>Hf</b> hafnium (178.49)	<b>Ta</b> tantalum (180.94788)	<b>W</b> tungsten (183.84)	<b>Re</b> rhenium (186.207)	<b>Os</b> osmium (190.23)	<b>Ir</b> iridium (192.222)	<b>Pt</b> platinum (195.084)	<b>Au</b> gold (196.966569)	<b>Hg</b> mercury (200.59)	<b>Tl</b> thallium (204.3833)	<b>Pb</b> lead (207.2)	<b>Bi</b> bismuth (208.9804)	<b>Po</b> polonium (209)	<b>At</b> astatine (210)	<b>Rn</b> radon (222)		
7	<b>Fr</b> francium (223)	<b>Ra</b> radium (226)	Lanthanoids	<b>Rf</b> rutherfordium (261)	<b>Db</b> dubnium (262)	<b>Sg</b> seaborgium (263)	<b>Bh</b> bohrium (264)	<b>Hs</b> hassium (265)	<b>Mt</b> meitnerium (266)	<b>Ds</b> darmstadtium (268)	<b>Rg</b> roentgenium (269)	<b>Cn</b> copernicium (270)	<b>Uut</b> ununtrium (271)	<b>Fl</b> flerovium (272)	<b>Uup</b> ununpentium (273)	<b>Lv</b> livermorium (276)	<b>Uus</b> ununseptium (277)	<b>Uuo</b> ununoctium (278)		
			<b>La</b> lanthanum (138.90547)	<b>Ce</b> cerium (140.12)	<b>Pr</b> praseodymium (140.90766)	<b>Nd</b> neodymium (144.242)	<b>Pm</b> promethium (144.91288)	<b>Sm</b> samarium (150.36)	<b>Eu</b> europium (151.964)	<b>Gd</b> gadolinium (157.25)	<b>Tb</b> terbium (158.92535)	<b>Dy</b> dysprosium (162.50015)	<b>Ho</b> holmium (164.93033)	<b>Er</b> erbium (167.259)	<b>Tm</b> thulium (168.934)	<b>Yb</b> ytterbium (173.054)	<b>Lu</b> lutetium (174.967)			
			<b>Ac</b> actinium (227)	<b>Th</b> thorium (232.0377)	<b>Pa</b> protactinium (231.036889)	<b>U</b> uranium (238.02891)	<b>Np</b> neptunium (237.048173)	<b>Pu</b> plutonium (244.06422)	<b>Am</b> americium (243)	<b>Cm</b> curium (247)	<b>Bk</b> berkelium (247)	<b>Cf</b> californium (251)	<b>Es</b> einsteinium (252)	<b>Fm</b> fermium (257)	<b>Md</b> mendelevium (258)	<b>No</b> nobelium (259)	<b>Lr</b> lawrencium (260)			

Figure C.1. | Periodic Table of Chemical Elements adapted from [9].





# Acknowledgements

This thesis not only represents years of work, published and unpublished results, failures and lessons learned, thus the sweat and tears of being a PhD student, but is also a symbol for the time spent in the here and now. My sincerest gratitude goes to all of those I shared this time with.

First of all and most importantly I would like to thank Martino, who has supported me throughout these years with his everlasting patience, ceaseless availability, enduring help and guidance. Without him, I would never have completed my PhD. His keen perception, persistence and motivation are the driving forces behind the written and unwritten achievements of this thesis. One could not ask for a more favorite boss.

I thank Prof. Ernst Meyer very much for acting as a co-referee for the certification of my thesis and thesis defense. Many thanks to Prof. Christoph Bruder for chairing my defense.

Special thanks go to the entire Poggio Lab. In the early days, the band of Phani, Michele and I filled an empty lab with spirit, science, and many tools. Only with the knowledgeable contribution and vast experience of Fei did we make huge steps towards our groups' first paper. I got to know the second generation of PhD students and postdocs—Arne, Hari, Ben, and Andrea—being a great help and noble colleagues who soon took initiative and found and developed their own projects. Finally the newbies—Davide, Floris, Denis, Marcus, Nicola, and Kavian, in order of appearance—with whom I never really worked with, and therefore must think I am only good at drinking coffee and being on facebook. To all of you: Thank you very much for the friendship and company. I was lucky to share my daily work with a marvelous and cheerful group of fellow students. I am now passing the torch on to you to take the small steps and giant leaps in the service of science and the Poggio Lab.

I am grateful to my collaborators Anna Fontcuberta i Morral in Lausanne and Dirk Grundler in Munich who not only provided me with samples, and therefore with something to measure in the first place, but also with profound scientific insight. Special thanks here to Daniel, who seemed always just a click away facing the same problems, while already knowing the answers to my questions. Thanks to the Maletinskys and Warburtons for the occasional Journal Clubs about color centers.

The work on my thesis and the whole lab itself would not have been possible if the mechanical and electronic workshops, represented by Sascha Martin and Michael Steinacher, were not able to solve all our problems. I will also fondly remember their company during our annual joint barbecues and rooftop parties.

What would I have done without the true rulers of the department, the ones who know just about everything and who can do anything by picking up the phone or typing magic words into their computers. Thanks Audrey for always being able to help me with my administrative and other problems, for great fun, good advice and perfectly coordinated colorful dresses. You are always welcome to peek your head into our office—no need to knock, we heard you laughing in the hallway a while ago. Thank you Astrid, Barbara and Germaine, for always being there when I needed that coffee coin, that file, that note pad, that fax, that immediate last minute help (even after noon). And thank you for the smiles as well. Thank you Bernd: With a happy grin and “hello” every time we meet you are a source of quick relaxation and friendly conversation.

Es grosses Dankeschön au an dr Kanton Aargau, bsunders an dr Herr Regierigsrot Alex Hürzeler (SVP), für d'Finanzierig vom Doktorat vomne Schwoob. (Und danke an Schorsch für die Übersetzung in die Muttersprache.)

I thank Arne for being a most reliable supporter and accurate critic, not only during days and nights of measurement, but also in unscientific endeavors. Thanks for chats on common topics and sometimes feeling “small and insignificant”. Thanks for the occasional beer, both at lunch and supper. Thanks for walking me home after work, for your patience, and the shared love for indecent thinking. And last but not least, thanks for saving me by discussing and proofreading my entire thesis.

Thank you Michele for welcoming me to the group and being my first friend in Basel. We had a lot of good times, most notably, I remember Fasnacht and our vacation in Lecce. Now that we went through the hell of thesis writing together, nothing can stop us. Thanks for being a reliable roommate for more than three years and thanks for a lot of good pasta, for which half of the gratitude goes to Mamma.

Andi and Johnny, I think you also lived in my apartment, I'm not sure. You were always running when I was awake, and went to bed when I came home. No, seriously, we were having an amazing time—thank you for being awesome housemates. We will have a barbecue soon!

I am deeply and utterly thankful to Björn, Clemens, and Damian, who set me on the right track in academia and life and without whom I would never have made it through university. Thanks for all your help and friendship.

There is no way I could possibly express my gratitude to my parents who have supported me at every point in my life.

# Curriculum Vitae

## Dennis P. Weber

Born on September 17th 1981 in Rastatt, Germany.

Department of Physics  
University of Basel  
Klingelbergstrasse 82  
4056 Basel  
Switzerland

dennis.weber@unibas.ch

## Education And Relevant Work

- 2014      PhD (Dr. phil.) in Experimental Physics  
University of Basel, Switzerland  
Thesis on “Dynamic Cantilever Magnetometry of Individual Ferromagnetic Nanotubes” in the group of Prof. Martino Poggio.
- 2008–2009    Institute for Reliability of Components and Systems (izbs), Karlsruhe Institute of Technology (KIT), Germany, in the Group of Prof. Peter Gumbsch, together with Robert Bosch GmbH, Germany.  
Scientific assistant in the field of microstructure related material modeling for ceramic matrix composites (CMC).
- 2007      Diplom (Dipl.-Phys.) in Physics  
Karlsruhe Institute of Technology (KIT), Karlsruhe, Germany  
Thesis on the “Analysis of Transient Conductance Levels in Atomic Switches” in the group of Prof. Thomas Schimmel.
- 2005      Master of Science (M.Sc.) in Physics  
University of Oregon, Eugene, OR, USA
- 2001      Abitur  
Tulla-Gymnasium, Rastatt, Germany

## List of Publications

- [77] Fei Xue, P. Peddibhotla, M. Montinaro, D. P. Weber, and M. Poggio. “A geometry for optimizing nanoscale magnetic resonance force microscopy”. *Applied Physics Letters*, **98**(16):163103, April 2011. doi: 10.1063/1.3579521
- [85] Fei Xue, D. P. Weber, P. Peddibhotla, and M. Poggio. “Measurement of statistical nuclear spin polarization in a nanoscale GaAs sample”. *Phys. Rev. B*, **84**(20):205328, November 2011. doi: 10.1103/PhysRevB.84.205328
- [22] D. P. Weber, D. Ruffer, A. Buchter, F. Xue, E. Russo-Averchi, R. Huber, P. Berberich, J. Arbiol, A. Fontcuberta i Morral, D. Grundler, and M. Poggio. “Cantilever magnetometry of individual ni nanotubes”. *Nano Lett.*, **12**(12):6139–6144, December 2012. doi: 10.1021/nl302950u
- [50] A. Buchter, J. Nagel, D. Ruffer, F. Xue, D. P. Weber, O. F. Kieler, T. Weimann, J. Kohlmann, A. B. Zorin, E. Russo-Averchi, R. Huber, P. Berberich, A. Fontcuberta i Morral, M. Kemmler, R. Kleiner, D. Koelle, D. Grundler, and M. Poggio. “Reversal mechanism of an individual ni nanotube simultaneously studied by torque and SQUID magnetometry”. *Phys. Rev. Lett.*, **111**(6):067202, August 2013. doi: 10.1103/PhysRevLett.111.067202

